

# **TROPOSPHERIC EMISSION SPECTROMETER (TES)**

## **LEVEL 2 ALGORITHM THEORETICAL BASIS DOCUMENT**

Version 1.1  
October 1, 1999

Jet Propulsion Laboratory  
California Institute of Technology  
Pasadena, California

# **TROPOSPHERIC EMISSION SPECTROMETER (TES)**

## **LEVEL 2 ALGORITHM THEORETICAL BASIS DOCUMENT**

Reinhard Beer	Jet Propulsion Laboratory
Kevin W. Bowman	Jet Propulsion Laboratory
Patrick D. Brown	Atmospheric and Environmental Research Inc.
Shepard A. Clough	Atmospheric and Environmental Research Inc.
Aaron Goldman	University of Denver
Daniel J. Jacob	Harvard University
Jennifer A. Logan	Harvard University
Mingzhao Luo	Jet Propulsion Laboratory
Frank J. Murcray	University of Denver
David M. Rider	Jet Propulsion Laboratory
Curtis P. Rinsland	NASA Langley Research Center
Clive D. Rodgers	University of Oxford
Stanley P. Sander	Jet Propulsion Laboratory
Eugene A. Ustinov	Jet Propulsion Laboratory
Helen M. Worden	Jet Propulsion Laboratory
Marguerite Syvertson, editor	Jet Propulsion Laboratory

---

Approved by:  
Reinhard Beer  
TES Principal Investigator

Version 1.1  
October 1, 1999

Jet Propulsion Laboratory  
California Institute of Technology  
Pasadena, California

## **TES Level 2 Algorithm Theoretical Basis Document**

---

This document was prepared at the Jet Propulsion Laboratory, California Institute of Technology, under a contract from the National Aeronautics and Space Administration.

## TABLE OF CONTENTS

<b>I. LIST OF ACRONYMS</b>	<b>VII</b>
<b>II. TES NOTATION AND STANDARD UNITS</b>	<b>IX</b>
<b>III. LIST OF FIGURES</b>	<b>XIII</b>
<b>IV. LIST OF TABLES</b>	<b>XIII</b>
<b>1.0 INTRODUCTION</b>	<b>1</b>
1.1 PURPOSE	1
1.2 SCOPE	1
1.3 APPLICABLE DOCUMENTS	1
1.3.1 Controlling Documents	1
1.3.2 Project Reference Documents	1
1.4 REVISION HISTORY	1
<b>2.0 BACKGROUND</b>	<b>2</b>
2.1 EXPERIMENT OBJECTIVES	2
2.2 RELEVANCE TO EARTH SYSTEM SCIENCE	2
2.3 INSTRUMENT CHARACTERISTICS	3
2.4 STANDARD PRODUCTS	4
2.5 SPECIES INCLUDED IN RETRIEVALS	7
<b>3.0 ALGORITHM DESCRIPTION</b>	<b>12</b>
3.1 ALGORITHM OVERVIEW	12
3.1.1 TES Working Prototype Retrieval Algorithm (TWPR)	13
3.2 STATE VECTORS	15
3.2.1 Terminology	15
3.2.2 Full State Vector Elements	15
3.2.3 Pressure Level Grids	16
3.2.4 Spectral Grids	17
3.2.4.1 Spectral grid for radiative transfer	17
3.2.4.2 Spectral grid for heavy molecules and continua	17
3.2.4.3 Spectral grid for clouds and aerosols	17

<b>3.3 FORWARD MODEL: ATMOSPHERE</b>	<b>17</b>
3.3.1 Radiative Transfer	17
3.3.1.1 Ray Tracing and Path Integrals	19
3.3.1.2 Ray Tracing (Surface Layer)	19
3.3.1.3 Optical Depth	20
3.3.1.4 Atmospheric Radiance	20
3.3.1.5 Non-LTE	21
3.3.1.6 Radiative Transfer for the Solar Contribution	22
3.3.1.7 Surface Contribution	23
3.3.1.8 Simultaneous Multiple Rays	24
3.3.1.9 Horizontal Inhomogeneity	24
3.3.2 Surface Model	25
3.3.2.1 Surface Radiative Properties	25
3.3.2.2 Map of Earth Surface Composition	25
3.3.2.3 Digital Elevation Model	25
3.3.3 Radiative Transfer for Aerosols	26
3.3.5 Instrumental Line Shape Spectral Convolution and Apodization	28
3.3.6 Field-of-View Spatial Convolution	28
3.3.7 Absorption Coefficient (ABSCO) Tables	30
3.3.7.1 ABSCO Table Generation (Using LBLRTM)	30
3.3.7.2 TES Line-by-Line Code	31
3.3.7.3 Cross-Section Code	33
3.3.7.4 Pressure Interpolation	33
3.3.8 ABSCO Databases	34
3.3.8.1 Line Parameters	34
3.3.8.2 Cross-Sections	34
3.3.8.3 Aerosols	36
3.3.8.4 CKD 3.0 Continuum	36
 <b>3.4 JACOBIANS</b>	 <b>37</b>
3.4.1 Finite Difference	37
3.4.2 Analytical	38
3.4.2.1 Temperature and Gas Concentrations	38
3.4.2.2 Surface Properties	39
3.4.2.3 Limb Background Parameters	39
3.4.2.4 Pointing	40
 <b>3.5 RETRIEVAL</b>	 <b>40</b>
3.5.1 General Strategy	40
3.5.2 Retrieval Vectors	41
3.5.2.1 Limb Background Parameters	41
3.5.3 A Priori Constraints	43
3.5.3.1 Surface Radiative Properties	43
3.5.3.2 Reference Pressure	44
3.5.4 Inverse Algorithm	44
3.5.4.1 Initial Guess	44
3.5.4.2 Initial Guess Refinement	44
3.5.4.2.1 Nadir	45
3.5.4.3 Numerical Solution	47
3.5.4.4 Convergence Criterion	48
3.5.4.5 Jacobian Update	49
3.5.5 Clear Pixel Identification (nadir)	49
3.5.6 Clear Pixel Identification (limb)	50
3.5.7 Retrieval Microwindow Selection	50

3.5.8 <i>A Priori</i> Database Generation	50
3.5.9 Error Analysis	51
<b>3.6 FINAL FULL SPECTRUM CALCULATION</b>	<b>52</b>
<b>3.7 DATA QUALITY &amp; RESIDUALS</b>	<b>52</b>
<b>4.0 ALGORITHM VERIFICATION</b>	<b>53</b>
4.1 END-TO-END CLOSURE EXPERIMENTS	53
4.2 VALIDATION	53
<b>5.0 REFERENCES</b>	<b>55</b>

THIS PAGE INTENTIONALLY LEFT BLANK.

## I. LIST OF ACRONYMS

ABSCO	Absorption coefficient
ADEOS	Advanced Earth Observing Satellite
AER	Atmospheric and Environmental Research Inc.
AERI	Atmospheric Emitted Radiation Interferometer
AES	Airborne Emission Spectrometer
AIRS	Atmospheric Infrared Sounder
ARM	Atmospheric Radiation Measurements
ASTER	Advanced Spaceborne Thermal Emission and Reflection Radiometer
ATBD	Algorithm Theoretical Basis Document
ATMOS	Atmospheric Trace Molecule Spectrometer
CAMEX	Convection and Moisture Experiment
CART	Cloud and Radiation Test (site)
CDC	Climate Diagnostics Center
CFC	chlorofluorocarbon
CHEM	Chemistry Mission (EOS third spacecraft)
CKD	Clough, Kneizys, and Davies
DAAC	Distributed Active Archive Center
DAO	Data Assimilation Office
DEM	Digital Elevation Model
ECMWF	European Center for Medium Range Weather Forecasting
ENVISAT	ESA Environmental Satellite
EOS	Earth Observing System
ETOPO5	Global digital elevation model on a 5-minute grid
FEV	fraction of explained variance
FFT	Fast Fourier Transform
FOV	field of view
GTOPO30	Global digital elevation model on a 30-arc second grid produced by the U. S. Geological Survey's EROS Data Center in Sioux Falls, South Dakota
HCFC	Hydrogenated Chlorofluorocarbon
HDF	Hierarchical Data Format
HFC	Hydrogenated Fluorocarbon
HIS	High resolution Interferometric Sounder
HITRAN	The molecular spectroscopic database
ILS	instrument line shape
IMG	Interferometric Monitor of Greenhouse Gases
ISAMS	Improved Stratospheric and Mesospheric Sounder
JPL	Jet Propulsion Laboratory
LaRC	Langley Research Center
LBLRTM	Line By Line Radiative Transfer Model
LIMS	Limb Infrared Monitor of the Stratosphere
LOS	line of sight
LRIR	Limb Radiance Inversion Radiometer
MIPAS	Michelson Interferometer for Passive Atmospheric Sounding
NASA	National Aeronautics and Space Administration
NAST-I	NPOESS Aircraft Sounder Testbed – Interferometer



NMC/NCEP	National Meteorological Center/National Center for Environmental Prediction
NOAA	National Oceanic and Atmospheric Administration
OD	optical depth
SCF	Science Computing Facility
TES	Tropospheric Emission Spectrometer
TOA	top of atmosphere
TOVS	TIROS N Operational Vertical Sounder
UARS	Upper Atmosphere Research Satellite
VMR	volume mixing ratio

## II. TES NOTATION AND STANDARD UNITS

### General

Both symbols and units are given in the lists below. The first column is the unit to be used in code, and in files unless there is good reason to use other (well documented) units. If other units are used in files, the data should be converted to the recommended unit on input. SI under the heading *docs* means any conventional SI unit, with standard prefixes for powers of  $10^3$ . Where no unit is given, the quantity is dimensionless.

		<i>code &amp; files</i>	<i>docs</i>
<b><u>Thermodynamics &amp; mass distribution</u></b>			
$T$	(level) temperature	K	SI
$\bar{T}$	layer mean temperature	K	SI
$P$	pressure	Pa	SI, hPa
$\bar{P}$	layer mean pressure	Pa	SI, hPa
$P_m$	partial pressure of gas g	Pa	SI, hPa
$\zeta$	log pressure parameter		
$\rho$	(mass) density	kg m <sup>-3</sup>	SI
$H$	pressure scale height	m	SI
$g$	acceleration due to gravity	m s <sup>-2</sup>	SI
$M_m$	molar mass of gas g	kg mole <sup>-1</sup>	SI
$q_m$	volume mixing ratio of gas g	fractional	*ppxv
$\bar{q}_m$	volume mixing ratio layer mean	fractional	*ppxv *x is m, b, t, etc.
<b><u>Geometry</u></b>			
$z$	height	m	SI
$r$	radius from a center	m	SI
$R_e$	Earth radius to geoid	m	SI
$R_c$	Earth radius of curvature at geoid	m	SI
$R_s$	Earth center to satellite	m	SI
$R_{cs}$	Radius of curvature to satellite	m	SI
$\psi$	Angle at center of curvature between path element and tangent point	rad	deg
$\psi_s$	Angular position of satellite	rad	deg
$\phi$	latitude	rad	deg
$\lambda$	longitude	rad	deg
$\theta$	zenith angle of a ray	rad	deg
$s$	distance along ray	m	SI

### **Indexing**

$i$	frequency index
$j, k$	level index
$l$	layer index

Levels indices are numbered 0 to N, bottom to top.  
Corresponding layers are numbered from 1 to N

### **Spectroscopy**

$S$	line intensity	$\text{cm}^{-1} \text{ molec}^{-1} \text{ cm}^2$	$\text{cm}^{-1} \text{ molec}^{-1} \text{ cm}^2$
$f(\nu)$	line shape	$1/\text{cm}^{-1}$	$1/\text{cm}^{-1}$
$\chi_\nu$	spontaneous emission line shape	$1/\text{cm}^{-1}$	$1/\text{cm}^{-1}$
$\phi_\nu$	absorption and stimulated emission line shape	$1/\text{cm}^{-1}$	$1/\text{cm}^{-1}$
$\rho_n$	number density	$\text{molec cm}^{-3}$	SI
$\tilde{C}_s, \tilde{C}_f$	self and foreign continuum functions	$\text{cm}^{-1} \text{ molec}^{-1} \text{ cm}^2 \text{ atm}^{-1}$	

[Warning: the units recommended here are not SI because the HITRAN data base is not in SI. Care must be taken when combining them with other quantities.]

### **Radiative Transfer**

$\nu$	wavenumber	$\text{cm}^{-1}$	$\text{cm}^{-1}$
$n$	refractive index		
$L$	spectral radiance	$\text{W m}^{-2} \text{ sr}^{-1}/\text{cm}^{-1}$	$*\text{W m}^{-2} \text{ sr}^{-1}/\text{cm}^{-1}$
$L^\uparrow$	up radiance, etc	$\text{W m}^{-2} \text{ sr}^{-1}/\text{cm}^{-1}$	$*\text{W m}^{-2} \text{ sr}^{-1}/\text{cm}^{-1}$
$F$	flux	$\text{W m}^{-2}/\text{cm}^{-1}$	$*\text{W m}^{-2}/\text{cm}^{-1}$
$B$	Planck function	$\text{W m}^{-2} \text{ sr}^{-1}/\text{cm}^{-1}$	$*\text{W m}^{-2} \text{ sr}^{-1}/\text{cm}^{-1}$
$J$	source function	$\text{W m}^{-2} \text{ sr}^{-1}/\text{cm}^{-1}$	$*\text{W m}^{-2} \text{ sr}^{-1}/\text{cm}^{-1}$
$\tau_l$	optical depth of layer $l$		
$T_l$	transmittance of layer $l$		
$\tau_{ik}$	optical depth of path from level $i$ to level $k$		
$T_{ik}$	transmittance of path from level $i$ to level $k$		
$u_l$	layer amount (number)	$\text{molec m}^{-2}$	SI
$u_{il}$	column amount (number)	$\text{molec m}^{-2}$	SI
$\kappa_g$	absorption coefficient of gas $g$	$\text{m}^2 \text{ molec}^{-1}$	SI
$\epsilon$	emissivity		
$\alpha$	albedo		
$R_{\text{BRDF}}$	Bidirectional Reflectance Distribution Function		
$\Phi$	Instrument line shape	$1/\text{cm}^{-1}$	$1/\text{cm}^{-1}$
$\Psi$	Field of view function	$\text{rad}^{-1}$	$\text{deg}^{-1}$
$r_1, r_u$	ratios of NLTE to LTE state populations		
$g_1, g_u$	state degeneracies for upper and lower states		
$n_1, n_u$	occupation numbers for upper and lower states		
$\Delta$	LTE vibrational Boltzmann factor		
$C_\nu$	Non-LTE correction function		
$R_\nu$	Volumetric radiation function	$\text{W m}^{-2} \text{ sr}^{-1}/\text{cm}^{-1}$	$*\text{W m}^{-2} \text{ sr}^{-1}/\text{cm}^{-1}$

\* with SI-style prefix ( $\mu$ , m, etc)

## **Retrieval**

Matrices are upper case bold. Column vectors are lower case bold. Superscript T (e.g.  $A^T$ ) indicates transpose

$\mathbf{x}_f$	full state vector
$\mathbf{x}$	retrieval vector
	– $\hat{\mathbf{x}}$ for retrieved $\mathbf{x}$
	– $\mathbf{x}_a$ for a priori
	– $\mathbf{x}_0$ for first guess
	– $\mathbf{x}_i$ for i'th iteration
$\mathbf{y}$	measurement vector
$\mathbf{e}$	measurement error
$\mathbf{b}$	forward model parameters
$\mathbf{F}$	generic forward model
$\mathbf{S}$	covariance matrices. Subscript determines which.
	– $\mathbf{S}_e$ for $\mathbf{e}$
	– $\mathbf{S}_a$ for $\mathbf{x}-\mathbf{x}_a$
	– $\hat{\mathbf{S}}$ for $\mathbf{x}-\hat{\mathbf{x}}$
$\mathbf{K}$	Jacobian
$\mathbf{A}$	averaging kernel
$\mathbf{G}$	Kalman gain (contribution function)
$\mathbf{I}_n$	unit matrix (order $n$ optional)
$\mathbf{O}_n$	zero matrix (order $n$ optional)
$\sigma$	standard deviation
$z_r$	correlation length
$C$	cost function

## **Physical constants**

$k_B$	Boltzmann constant
$c$	speed of light
$h$	Planck constant
$N$	Avagadro constant
$\sigma$	Stefan-Boltzmann constant
$c_1$	First radiation constant
$c_2$	Second radiation constant
$R$	Molar gas constant

THIS PAGE INTENTIONALLY LEFT BLANK.

### III. LIST OF FIGURES

Figure 3 - 1: TES Level 2 Retrieval Flow	14
Figure 3 - 2: Illustration of the recursive radiative transfer calculations	21
Figure 3 - 3: Monochromatic solar spectrum over the spectral region relevant to TES (Kurucz, 1995).	28
Figure 3 - 4: Diagram for TES pointing geometry and FOV convolution in limb mode	30
Figure 3 - 5: Observed HIS spectrum and LBLRTM calculated results in equivalent brightness temperature for CAMEX case (a) and observed-calculated differences (b). The nadir measurement was taken from 20 km on the NASA ER2.	32
Figure 3 - 6: AFGL Mid Latitude Summer Profiles	43

### IV. LIST OF TABLES

Table 2 - 1: TES Filter Bandpasses	3
Table 2 - 2: TES Global Survey Filters	4
Table 2 - 3: TES Standard Products	5
Table 2 - 4: TES Product Reporting Levels [= UARS Standard Levels]	6
Table 2 - 5: Format for Reporting TES Retrievals	7
Table 2 - 6: HITRAN Line List Species Used by TES	8
Table 2 - 7: HITRAN Cross-Section Species Used by TES	10
Table 2 - 8: Additional Cross-Section Species Needed by TES	11
Table 3 - 1: IR cross-section data prepared for TES	35
Table 3 - 2: Retrieval results for temperature and tangent point for central ray of pixel 11 with TES FOV (tangent height = 11.5 km).	46
Table 3 - 3: Quantities related to the ray trace from the tangent point to the satellite as a function of tangent height. Refraction is included in the ray trace.	47

THIS PAGE INTENTIONALLY LEFT BLANK.

## 1.0 INTRODUCTION

### 1.1 PURPOSE

This Algorithm Theoretical Basis Document (ATBD) describes the algorithms used to retrieve all Tropospheric Emission Spectrometer (TES) Standard Data Products. These products are scheduled to be archived at the NASA Langley Research Center (LaRC) Distributed Active Archive Center (DAAC) <http://eosdis.larc.nasa.gov>. The standard products consist of vertical volume mixing ratio profiles of ozone, water vapor, carbon monoxide, methane, nitric oxide, nitrogen dioxide and nitric acid and their associated error estimates. Note that all products are retrieved near-simultaneously through a common process and are therefore discussed jointly rather than individually.

This document identifies the following: sources of input data that are required for the retrievals; provides the physical theory and mathematical background underlying the use of this information in the retrievals; describes practical considerations affecting algorithm development; and outlines a test and validation approach.

### 1.2 SCOPE

This document covers the algorithm theoretical basis for the parameters to be included in the TES Data Products at or near launch time. Only parameters that are to be routinely retrieved at the DAAC are discussed. On-going development and prototyping efforts may result in modifications to parts of certain algorithms. Only the algorithms that are implemented at the DAAC for routine processing of TES data will be preserved in the final release of this document. However, certain materials deemed too detailed for the main body of the document may be found in the Appendices, which are numerically keyed to their relevant sub-sections.

### 1.3 APPLICABLE DOCUMENTS

#### 1.3.1 Controlling Documents

1) *Mission to Planet Earth Strategic Enterprise Plan 1998-2002*. NASA HQ MTPE, Oct 1998.  
<http://www.earth.nasa.gov/visions/stratplan/index.html>

2) *Execution Phase Project Plan for the Earth Observing System (EOS)*. GSFC 170-01-01, Rev. A, May 1995.

#### 1.3.2 Project Reference Documents

*Tropospheric Emission Spectrometer: Scientific Objectives & Approach, Goals & Requirements*. JPL D-11294, Rev. 5.0, May 1996.

### 1.4 REVISION HISTORY

The original version (1.0) of this document was dated January 29, 1999.



## 2.0 BACKGROUND

### 2.1 EXPERIMENT OBJECTIVES

The Tropospheric Emission Spectrometer (TES), selected for flight on the EOS CHEM I mission, will provide the first global view of the chemical state of the troposphere (the lowest region of the atmosphere, extending from the surface to about 10-15 km altitude). The investigation will focus on mapping the global distribution of tropospheric ozone and on understanding the factors that control ozone concentrations.

Ozone is produced in the troposphere by photochemical oxidation of carbon monoxide (CO) and hydrocarbons in the presence of nitrogen oxides (NO<sub>x</sub>) and water vapor. These ozone precursors have both natural and anthropogenic sources. The chemistry of ozone is complex and tightly coupled to the atmospheric transport of both ozone and the precursors.

Tropospheric ozone has three major environmental impacts:

- 1) AS AN AIR POLLUTANT. Ozone in surface air is toxic to humans, animals and vegetation. It is the principal harmful component of smog.
- 2) AS A CLEANSING AGENT. Photolysis of ozone in the presence of water vapor is the primary source of the hydroxyl radical (OH), which is the main oxidant in the atmosphere. Reactions with OH in the lower and middle troposphere are the principal sink for a large number of environmentally-important species including air pollutants (carbon monoxide), greenhouse gases (methane), and gases depleting the stratospheric ozone layer (HCFC's, methyl halides).
- 3) AS A GREENHOUSE GAS. Ozone in the middle and upper troposphere is an efficient greenhouse gas. Perturbation of ozone in this region of the atmosphere results in heterogeneous radiative forcing with complicated implications for climate.

The troposphere contains only about 10% of the total ozone in the atmosphere -the bulk is in the stratosphere. The environmental implications of tropospheric ozone are very different from those of stratospheric ozone. The ozone layer in the stratosphere shields the Earth's surface from solar UV-B radiation, and thinning of this layer as a result of human activities is a matter of grave concern. Tropospheric ozone, by contrast, has increased as a consequence of human activity (primarily because of combustion processes). Whether this increase in tropospheric ozone is beneficial (cleansing agent) or harmful (air pollutant, greenhouse gas) depends to a large extent on its altitude. It is very important, therefore, to map the global 3-dimensional distribution of tropospheric ozone and its precursors in order to improve our understanding of the factors controlling ozone in different regions of the troposphere.

The specific Standard Products that TES will produce are global-scale vertical concentration profiles (0 - ~33 km) of ozone, water vapor, carbon monoxide, methane, nitric oxide, nitrogen dioxide and nitric acid (the latter 3 in the mid- and upper troposphere only). Essential by-products of the analysis are atmospheric temperature profiles and surface temperature and emissivity.

### 2.2 RELEVANCE TO EARTH SYSTEM SCIENCE

One of the primary EOS themes is 'Atmospheric Ozone Research.' TES directly addresses this theme.

## **2.3 INSTRUMENT CHARACTERISTICS**

TES is an infrared, high resolution, Fourier Transform spectrometer covering the spectral range 650 - 3050  $\text{cm}^{-1}$  (3.3 - 15.4  $\mu\text{m}$ ) at a spectral resolution of 0.1  $\text{cm}^{-1}$  (nadir viewing) or 0.025  $\text{cm}^{-1}$  (limb viewing). The two observation modes are essential because many of the spectral features that TES observes are very weak (especially the nitrogen oxides) and limb-viewing markedly enhances their measurability (with the deficiency that cloud interference is much more likely than in nadir viewing, where TES has relatively good spatial resolution).

In order to improve signal-to-noise ratio and improve collection efficiency, TES is (as far as possible) radiatively cooled to ~180K, and it divides the spectral range into 4 sub-regions, each observed with a separate 1x16 array of detectors (identified as 1A, 1B, 2A, and 2B) actively cooled to 65K. The bandwidth is further restricted to ~250  $\text{cm}^{-1}$  by interchangeable filters. With these arrays, 16 altitudes in the troposphere and lower stratosphere are observed simultaneously with a height separation of 2.3 km or, alternatively, 16 contiguous areas (each 0.5 x 5 km) are observed on the ground. Table 2 - 1 shows the available filter ranges and their identifiers. A complete description of TES can be found as an appendix to the L1B ATBD [JPL D-16479, Oct.1 1999].

**Table 2 - 1: TES Filter Bandpasses**

Filter ID	Lower 50% Point, $\text{cm}^{-1}$	Upper 50% Point, $\text{cm}^{-1}$
1A1	1900	2250
1A2	2200	2450
1A3	2425	2650
1A4	2600	2850
1A5	2800	3050
1B1	820	1050
1B2	950	1150
2A1	1100	1325
2A2	1300	1550
2A3	1500	1750
2A4	1700	1950
2B1	650	900

Note: Any combination of 1Ax, 1By, 2Az and 2B1 is allowable (1 per detector array) with the proviso that, normally, only limited switching among 1Ax and 2Az filters can occur between successive scans. The actual arrangement of the filters in the filter wheels has been optimized for expected observation scenarios.

The filters actually employed for the Global Surveys are shown in Table 2 - 2. Sequences “A” and “B” alternate every 81.2 seconds for 58 orbits (4 days) for a total of 4234 sequences (= no. of profile sets). Note also that the pairs of nadir observations in each sequence are co-located.

**Table 2 - 2: TES Global Survey Filters**

Sequence	Scan No.	Type	Array 1A	Array 1B	Array 2A	Array 2B
A	1	Space	1A1	1B1	2A2	2B1
A	2	Black Body	1A1	1B1	2A2	2B1
A	3	Nadir	1A1	1B2	2A2	2B1
A	4	Nadir	1A1	1B2	2A2	2B1
A	5	Limb	1A1	1B1	2A2	2B1
A	6	Limb	1A1	1B2	2A4	2B1
A	7	Limb	1A1	1B2	2A4	2B1
B	1	Space	1A1	1B2	2A2	2B1
B	2	Black Body	1A1	1B2	2A4	2B1
B	3	Nadir	1A1	1B2	2A4	2B1
B	4	Nadir	1A1	1B2	2A2	2B1
B	5	Limb	1A1	1B1	2A2	2B1
B	6	Limb	1A1	1B2	2A4	2B1
B	7	Limb	1A1	1B2	2A4	2B1

In the limb mode, TES measures the infrared thermal emission from the atmosphere. In the nadir mode, the measurement is of the surface emission, downward directed atmospheric emission scattered from the surface, and further emission and absorption by the atmosphere. In a limited spectral range, under sunlit conditions, there may also be solar radiation scattered from the atmosphere and the surface.

TES obtains its data in 4 seconds (nadir) or 16 seconds (limb) plus calibrations in a sequence: 2 calibrations followed by 2 nadir observations followed by 3 limb observations. The entire cycle requires 81.2 seconds and is repeated continuously for four days out of eight, interspersed with major calibration-only sequences (essential for this type of instrument) and occasional targets-of-opportunity such as volcanic eruptions, biomass burning regions or regional ozone episodes for which TES has unique capabilities (but note that these are Special, not Standard, Products and are not further considered in this document).

It is a property of a Fourier Transform Spectrometer that it must be used in a so-called ‘staring’ mode (that is, the target location or altitude must be tracked). Accordingly, TES is equipped with a precision pointing system.

## **2.4 STANDARD PRODUCTS**

TES Standard Products (and their data sources) are shown in Table 2 - 3.

**Table 2 - 3: TES Standard Products**

Product	Nadir	Limb
Atmospheric Temperature, T	√	√
Surface Temperature, T <sub>s</sub>	√	
Land Surface Emissivity	√	
Ozone (O <sub>3</sub> ) VMR	√	√
Water Vapor (H <sub>2</sub> O) VMR	√	√
Carbon Monoxide (CO) VMR	√	√
Methane (CH <sub>4</sub> ) VMR	√	√
Nitric Oxide (NO) VMR		√
Nitrogen Dioxide (NO <sub>2</sub> ) VMR		√
Nitric Acid (HNO <sub>3</sub> ) VMR		√

Standard Products will be reported at the pressure levels shown in Table 2 - 4 (note that the corresponding altitudes are approximate). Nadir and limb data are nearly co-located.

For each species, at each level, the reported parameters will be as shown in Table 2 - 5. The meaning of the last 5 columns is the following:

*Volume Mixing Ratio* (VMR,  $q$ ) is reported with respect to dry air to avoid the problem that the H<sub>2</sub>O VMR can be large enough to effect the overall result.

*Random Errors* are the square roots of the diagonal elements of the output error covariance matrix (i.e., the  $1\sigma$  values). The full matrix is also available.

*Systematic Errors* are estimated from reported errors in, for example, the HITRAN database.

*Fraction of Explained Variance* (FEV) is a measure of how much the measurements improve upon the *a priori* data (see 3.5.9 for a detailed explanation). If the FEV = 1 then all the information comes from the data. If the FEV = 0 then no information comes from the data.

*Correlation Length* ( $z_r$ ) is a measure of the dependence of adjacent (or nearby) retrieval levels (see 3.5.9). If  $z_r \ll$  the distance between adjacent levels then the values are independent. If  $z_r \geq$  the distance between adjacent levels then the values are not independent.

Each such file will be accompanied by a header containing information such as the time, date, latitude, longitude, and solar zenith angle at acquisition, plus a set of data quality indicators.

**Table 2 - 4: TES Product Reporting Levels [= UARS Standard Levels]**

<b>Index</b>	<b>Pressure hPa</b>	<b>US S.A. Altitude km</b>	<b>Delta Altitude km</b>
0	1000.0	0.100	
1	681.3	3.175	3.075
2	464.2	6.100	2.925
3	316.2	8.825	2.725
4	215.4	11.350	2.525
5	146.8	13.800	2.450
6	100.0	16.200	2.450
7	68.1	18.650	2.450
8	46.4	21.100	2.500
9	31.6	23.600	2.500
10	21.5	26.100	2.500
11	14.7	28.600	2.600
12	10.0	31.200	2.600
13	6.8	33.800	2.600
14	4.6	36.600	2.800

“Delta Altitude” at level  $i$  is the difference between Level  $i$  and Level  $i-1$

**Table 2 - 5: Format for Reporting TES Retrievals**

<b>Species</b>	<b>Volume Mixing Ratio w.r.t Dry Air (<math>q</math>)</b>	<b>Estimated Random Error (<math>1\sigma</math>)</b>	<b>Estimated Systematic Error</b>	<b>Fraction of Explained Variance (FEV)</b>	<b>Correlation Length <math>z_r</math>, km</b>
----------------	---	--	---	---	--

## 2.5 SPECIES INCLUDED IN RETRIEVALS

In order to retrieve the Standard Products listed in Table 2 - 3, it is necessary to account for many more species in the process. These are often called “interferents” but, in fact, some will be retrieved as controls (e.g.,  $N_2O$ ), some flagged for Special Processing (e.g., heavy hydrocarbons) and some fixed. For example, in order to retrieve  $HNO_3$ , it is essential to include both  $CCl_3F$  (CFC11) and  $CCl_2F_2$  (CFC12) whose bands overlap the nitric acid signature.

The primary source of spectral information is the HITRAN database [Rothman *et al.*, 1998]. Not all of the species in the list are pertinent to TES but those that are, are shown in Tables 2 - 6 (line data) and 2 - 7 (cross-section data). In addition, some modifications and additions to the list are discussed elsewhere in this document and it should be noted that certain isotopomers *must* be treated as separate molecules because their concentrations relative to the parent are known to be height-variable (HITRAN assumes a fixed ratio). Finally, Table 2 - 8 lists some species that are likely to be important to TES but for which little or no useful spectral data are available (i.e., they are candidates for laboratory study in the very near future).

**Table 2 - 6: HITRAN Line List Species Used by TES**

<b>HITRAN [TES] Index No.</b>	<b>Molecule</b>	<b>Comments</b>
1	H <sub>2</sub> O	HDO & H <sub>2</sub> <sup>17</sup> O Separated
[1a]	HDO	
[1b]	H <sub>2</sub> <sup>17</sup> O	
2	CO <sub>2</sub>	
3	O <sub>3</sub>	<sup>16</sup> O <sup>17</sup> O <sup>16</sup> O & <sup>17</sup> O <sup>16</sup> O <sup>16</sup> O Separated
[3a]	<sup>16</sup> O <sup>17</sup> O <sup>16</sup> O	
[3b]	<sup>17</sup> O <sup>16</sup> O <sup>16</sup> O	
4	N <sub>2</sub> O	
5	CO	
6	CH <sub>4</sub>	CH <sub>3</sub> D Separated
[6a]	CH <sub>3</sub> D	
7	O <sub>2</sub>	
8	NO	
9	SO <sub>2</sub>	
10	NO <sub>2</sub>	
11	NH <sub>3</sub>	
12	HNO <sub>3</sub>	
13	OH	
14 **	(HF)	** Not Used **

## TES Level 2 Algorithm Theoretical Basis Document

---

15	HCl	
16 **	(HBr)	** Not Used **
17 **	(HI)	** Not Used **
18	ClO	
19	OCS	
20	HCOH	
21	HOCl	
22	N <sub>2</sub>	
23	HCN	
24	CH <sub>3</sub> Cl	
25	H <sub>2</sub> O <sub>2</sub>	
26	C <sub>2</sub> H <sub>2</sub>	
27	C <sub>2</sub> H <sub>6</sub>	
28 **	(PH <sub>3</sub> )	** Not Used **
29	COF <sub>2</sub>	
30	SF <sub>6</sub>	Also need X-sections
31	H <sub>2</sub> S	
32	HCOOH	
33 **	(HO <sub>2</sub> )	** Not Used **
34 **	(O)	** Not Used **
35	ClONO <sub>2</sub>	Also need X-sections
36 **	(NO <sup>+</sup> )	** Not Used **
37 **	(HOBr)	** Not Used **



**Table 2 - 7: HITRAN Cross-Section Species Used by TES**

<b>Molecule</b>	<b>Common Name</b>
$\text{CCl}_4$	Carbon Tetrachloride
$\text{CCl}_3\text{F}$	CFC-11
$\text{CCl}_2\text{F}_2$	CFC-12
$\text{CClF}_3$	CFC-13
$\text{CF}_4$	CFC-14
$\text{CHCl}_2\text{F}$	HCFC-21
$\text{CHClF}_2$	HCFC-22
$\text{C}_2\text{Cl}_3\text{F}_3$	CFC-113
$\text{C}_2\text{Cl}_2\text{F}_4$	CFC-114
$\text{C}_2\text{ClF}_5$	CFC-115
$\text{N}_2\text{O}_5$	Dinitrogen Pentoxide
$\text{HO}_2\text{NO}_2$	Peroxynitric Acid*
$\text{SF}_6$	Sulfur Hexafluoride
$\text{ClONO}_2$	Chlorine Nitrate

\* Seriously incomplete

**Table 2 - 8: Additional Cross-Section Species Needed by TES**

<b>Molecule</b>	<b>Common Name</b>
$C_6H_6$	Benzene
$C_2H_4$	Ethylene
$C_3H_8$	Propane
$CH_3C(O)CH_3$	Acetone
$CH_3OH$	Methyl Alcohol
$CH_3C(O)NO_2$	Peroxyacetyl Nitrate (PAN)
$HO_2NO_2$	Peroxynitric Acid*
$CH_3COOH$	Acetic Acid
$CH_3OOH$	Methyl Hydroperoxide

\* For bands not in HITRAN

## 3.0 ALGORITHM DESCRIPTION

### 3.1 ALGORITHM OVERVIEW

TES data processing falls naturally into 3 groups:

- 1) At Level 1A the raw data from the spacecraft are decommutated and the instrument outputs (called *interferograms*) reconstructed. File headers also contain important ancillary data such as time, date, spacecraft and target location, and instrument pointing.
- 2) At Level 1B, the interferograms are converted to spectra, radiometrically-calibrated and resampled onto a common frequency grid. Certain data quality flags are added to the header at this juncture and the results passed to Level 2 [JPL D-16479, 1999].
- 3) At Level 2, vertical concentration profiles of the selected species are extracted from the data through the process of *retrieval* that is the topic of this document.

Although this document is primarily concerned with standard products, we also expect to use the same algorithm for special products so we have retained generality in some sections to support these additional functions. This additional functionality will be maintained in the Reference Forward Model. We therefore describe the deliverable version as the Operational Forward Model.

Figure 3 - 1 shows an overall flow chart for the forward model and retrieval process.

In Global Survey mode, observations are made in sequences made up of calibration scans, two nadir observations and three limb observations, the limb observations corresponding geographically to nadir observations made 437 seconds earlier. These data will be combined into 'observation sets' containing collocated limb and nadir observations. Each observation set will then be analyzed as a unit.

Observation sets will be processed in batches containing all observations made each day at the same time after an equator crossing, i.e. at the same latitude. This will enable savings to be made in disk accesses for quantities that depend on latitude only. This includes climatological information used for the first guess and *a priori* information, which are likely to be zonally averaged. Making use of the fact that the distribution of  $N_2O$  is known in the troposphere, the retrieval of the column  $N_2O$  for nadir retrievals and  $N_2O$  profile for the limb retrievals will be used as a critical test that the retrieval of temperature has been successful and that the field of view is cloud free. Retrievals from partial observation sets will be attempted, but will be flagged and further evaluated before release.

Each observation set will be retrieved in several stages, with each stage using a selection of the results of a previous stage as *a priori*, or as a first guess, or as forward model parameters, as appropriate. For example, separate retrievals will be carried out for corresponding nadir and limb measurements, and for different constituents. Within the nadir and the limb retrievals, temperature will be retrieved first, and the results used as forward model parameters for constituent retrievals. The constituent retrievals will be carried out in an appropriate order so that an already retrieved quantity can be included as a forward model parameter ('interferent') for subsequent retrievals. Some quantities may be retrieved jointly. In particular, the final profile for the temperature and water vapor fields will be obtained from a joint retrieval.

Each retrieval will use the same inverse algorithm comprising the following stages:

- (1) initial guess construction;

- (2) initial guess refinement by means of a simplified retrieval;
- (3) *a priori* construction;
- (4) optimal estimate by numerically minimizing a cost function.

The optimal estimate will be obtained by a nonlinear least squares process with constraints. It will minimize a cost function, which includes contributions from both the departure of the measured spectrum from the calculated spectrum and the departure of the retrieved state from constraints imposed through the *a priori* state. (The *a priori* is not in general the same as the first guess, which is a state selected as a starting point for a non-linear iteration). An appropriate subset of the measured spectrum will be used for each parameter retrieved. This may comprise a microwindow or a large segment of spectrum.

Finally, the complete spectrum will be calculated for quality control. At this point, the atmosphere will be determined as well as possible, but the individual retrievals will not have covered the complete spectrum, so there will be gaps in the surface emissivity (nadir case) or aerosol optical depth (limb case). This necessitates a final retrieval using the entire spectrum, with fixed atmospheric parameters. The results will be the desired spectra, along with spectra of the surface emissivity or aerosol optical depth as by-products.

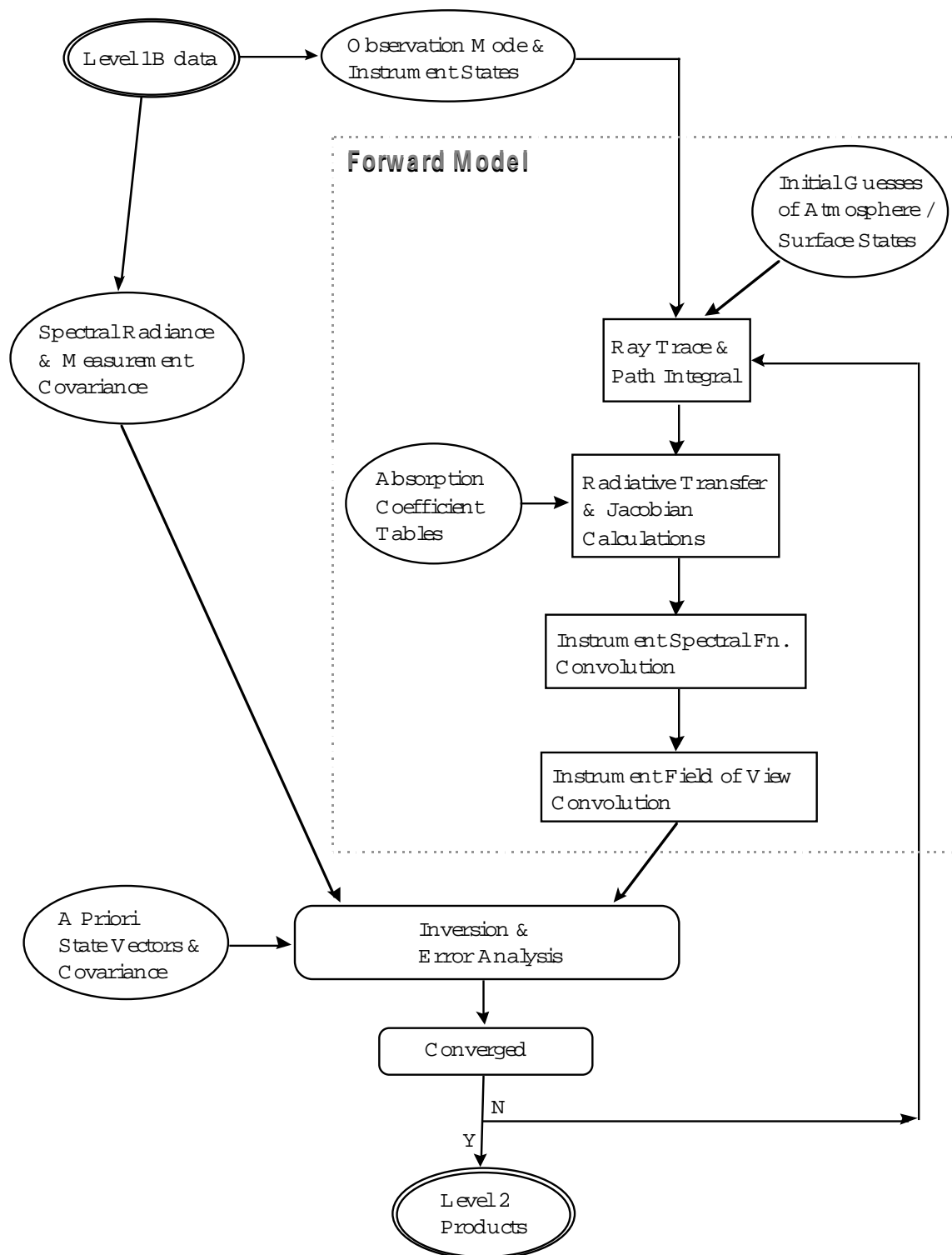
The optimal estimation process requires a numerical model to generate the spectrum expected for a particular atmospheric condition. Below, we describe the parameters necessary to carry out the calculation (3.2), the forward model (3.3), and the derivatives of the spectrum with respect to the desired parameters (3.4). The actual retrieval process is detailed in 3.5.

### 3.1.1 TES Working Prototype Retrieval Algorithm (TWPR)

Most of the algorithm elements discussed in this document have been coded and tested at the TES SCF in the TWPR (TES Working Prototype Retrieval Algorithm). The TWPR is used to test the speed and accuracy of ideas as they are put forward by the members of the Science Team and, whenever possible, validated against real data from AES (Airborne Emission Spectrometer), HIS (High Resolution Interferometer Sounder) and IMG (Interferometric Monitor of Greenhouse Gases). These instruments all have spectral resolution and coverage similar to TES, albeit nadir viewing only. When MIPAS (Michelson Interferometer for Passive Atmospheric Sounding) limb data become available, they will be used for the same purpose. It is our intention to continue using (and improving) the TWPR until it becomes clear that the deliverable, operational, algorithm is sufficiently advanced to make further development of the TWPR unnecessary.

Figure 3 - 1: TES Level 2 Retrieval Flow

# TES LEVEL 2 RETRIEVAL FLOW



## 3.2 STATE VECTORS

### 3.2.1 Terminology

A *state vector* specifies those aspects of the state of the atmosphere being measured, and of the instrument measuring it, which together determine the value of the resulting measurement. We will use the term *full state vector* to indicate the complete set of parameters required by the forward model (section 3.3) to simulate a measurement to the necessary accuracy, and the term *retrieval state vector* or simply *retrieval vector* to indicate the subset of the full state vector that is a target for retrieval. The remaining elements will either be predetermined (*forward model parameters*) or be determined by interpolation where the forward model requires a finer grid for numerical purposes.

### 3.2.2 Full State Vector Elements

The following elements comprise the full state vector for calculating nadir radiance:

- surface pressure
- temperature on a specified pressure grid
- constituent mixing ratios on a specified pressure grid
- aerosol extinction coefficients on specified pressure and wavenumber grids
- surface radiating temperature
- surface optical properties corresponding to each detector element on a specified wavenumber grid:
  - emissivity
  - albedo/reflectivity
  - bi-directional reflectivity distribution function
- nadir view angle
- nadir view location
- sun angle at the nadir location
- instrument line shape
- field of view function

The following elements comprise the full state vector for calculating limb radiance:

- temperature on a specified pressure grid
- constituent mixing ratios on a specified pressure grid
- aerosol extinction coefficients on specified pressure and wavenumber grids
- spacecraft position
- look angle of the boresight from the spacecraft
- sun angle at the tangent point location
- altitude of one pressure level
- instrument line shape
- field of view function

In this we assume that the atmosphere is hydrostatically balanced and radially symmetric. For the limb view, it may be necessary to include some representation of horizontal gradients of some of the elements.

There are several other quantities that should formally be part of the full state vector, but are best considered as constants, and treated separately by the forward model. These include

- Constituent absorption coefficients on a wavenumber, pressure and temperature grid.

- Digital elevation model
- Surface characterization map (Global land cover database)

### 3.2.3 Pressure Level Grids

The natural vertical grid for nadir forward model is based on pressure levels, as this is one in which the Jacobians have a particularly simple form. In order to combine results from the nadir and limb views, both must be on compatible grids, so this choice requires us to use a pressure grid for the limb view as well. We have chosen to use  $\log(P)$  as the basic vertical coordinate, and to make the grid spacing compatible with that established for UARS.

The full state vector will be defined on the *full grid*, which is a superset of the retrieval grid:

$$\log_{10}(P_i) = 5 - i/6m \quad (3.1)$$

where  $P_i$  is the pressure in pascals of level index  $i$  and the 'superset factor'  $m$  is an integer. The UARS grid corresponds to  $m=1$ , with a spacing of 6 levels per decade of pressure. The value of  $m$  will be determined by the accuracy requirements of the numerical method, and may vary with height.

The pressure grids for the retrieved state vectors will be subsets of those for the full state. The elements of the retrieval state vector that comprise profiles will be defined on a *retrieval grid*,

$$\log_{10}(P_j) = 5 - j/6n \quad (3.2)$$

The value of  $n$  will be a submultiple of  $m$ , chosen so that the full information content of the measurements can be represented. The range of levels used will vary with the quantity retrieved. The choice of the retrieval pressure levels for each TES product molecule and temperature are key investigation activities which involve the physical constraints used for profile retrieval and the trade-offs between the retrieval vertical resolution and the product accuracy.

Values of the profiled quantities between retrieval grid levels will be determined by the following interpolations:

- (1) Temperature is linearly interpolated in  $\log(P)$ .
- (2) Logarithms of constituent mixing ratios and aerosol extinction coefficients are interpolated and extrapolated linearly in  $\log(P)$ , and linearly extrapolated above the top level at the same gradient as in the top layer.

As an example, for the full state vector of the prototype forward we have constructed an 86-layer atmosphere model for simulations and for the absorption coefficient table pressure and temperature grids. This 86-layer atmosphere has 87 pressure levels between about 1211.53 hPa and 0.1 hPa. The pressure levels (in hPa) are defined up to 1 hPa as

$$P_k = 1000 \times 10^{-(k-2)/24} \quad k = 0 \dots 74; \quad (3.3)$$

and above 1 hPa as

$$P_k = 1000 \times 10^{-(k-38)/12} \quad k = 75 \dots 86; \quad (3.4)$$

In the troposphere, the layer thickness calculated using hydrostatic equation and for US standard atmosphere is about 0.83 km (surface) to 0.6 km (tropopause). Between 100 hPa and 1 hPa, the layer thickness is about 0.6-0.8 km; while above 1 mb, it is about 1.5 km.

### **3.2.4 Spectral Grids**

State vector elements specified on spectral grids will be interpolated by a 4-point Lagrangian. Nominal values of the spacings of the grids will be

• Radiative transfer calculation	0.0002 cm <sup>-1</sup>
• Aerosol extinction coefficients	0.0025 cm <sup>-1</sup>
• Surface emissivity	10 cm <sup>-1</sup>
• Surface albedo/reflectivity	10 cm <sup>-1</sup>
• Surface bi-directional reflectivity distribution function	10 cm <sup>-1</sup>

#### **3.2.4.1 Spectral grid for radiative transfer**

The spectral grid for the monochromatic radiative transfer calculations over the spectral domain associated with a specific filter is determined by the mean Doppler width at the top of the atmosphere. Studies of the dependence of errors in radiative transfer on spectral sampling indicate that for pressure broadened lines, a sampling grid of four points per Lorentz halfwidth is required, [Clough and Kneizys, 1979]. Extension of this analysis to the Doppler and Voigt line shapes leads to essentially the same conclusion. The spectral sampling based on this criterion, in addition to being appropriate for the stratosphere, provides proper spectral sampling of the narrow water lines in the atmospheric window regions and of the line coupling effects of the carbon dioxide Q branches in the pressure broadening regime. Since the spectral grid is based on the Doppler width, the grid, though fixed for a given filter, is frequency dependent by filter (coarser at higher wavenumber values). The spectral spacing for the 1B2 filter for the ozone region is 0.0001 cm<sup>-1</sup>.

Based on studies of computational efficiency and accuracy, a preliminary decision has been made to utilize a fixed spectral grid over the domain of a given filter. Although utilization of an adaptive spectral grid is attractive for reasons of storage and apparent efficiency, our initial studies indicate that implementation of an adaptive approach increases computational cost and, in the general case, a loss in accuracy.

#### **3.2.4.2 Spectral grid for heavy molecules and continua**

While the radiative transfer will be performed on the spectral grid as described, a coarser spectral grid will be used for storing the absorption coefficients associated with the heavier molecular species for which the individual line contributions are overlapped or the line parameters are not available, and for the continuum absorption associated with the more strongly absorbing species, principally water vapor and carbon dioxide. The spacing of this coarse spectral grid is 0.0025 cm<sup>-1</sup> and is controlled by the spectral sampling required for HNO<sub>3</sub>.

#### **3.2.4.3 Spectral grid for clouds and aerosols**

The spectral grid for surface properties, cloud and aerosol optical properties will be 10 cm<sup>-1</sup>.

## **3.3 FORWARD MODEL: ATMOSPHERE**

### **3.3.1 Radiative Transfer**

The spectral radiance received by TES can be expressed by the radiative transfer equation. Under clear conditions, the radiance received in a downlooking mode includes four contributions: upwelling atmospheric emission, attenuated reflected downwelling atmospheric emission, attenuated surface emission, and attenuated reflected solar radiation. In order to show the influence



of the sensor on the signal, the radiance must be convolved with the absolute instrument line shape (ILS) (Equation 3.5).

$$\begin{aligned}
 L(\Omega, \nu) = & \int_0^\infty \Phi(\nu, \nu') \left\{ \int_{z_0}^\infty B(\nu', T(z)) \frac{\partial T(\Omega, z, z_0, \nu')}{\partial z} dz \right. \\
 & \text{(Instrument)} \quad \text{(Upwelling atmospheric emission term)} \\
 & + \left[ \alpha(\nu') \int_{2\pi} R_{BRDF}(\Omega, -\Omega', \nu') \int_{\infty}^{z_0} B(\nu', T(z)) \frac{\partial T(-\Omega', z, z_0, \nu')}{\partial z} dz d\Omega' \right. \\
 & \quad \text{(Downwelling, back - reflected, atmospheric emission term)} \\
 & + \varepsilon(\Omega, \nu') \cdot B(\nu', T_{surf}) \\
 & \quad \text{(Surface emission term)} \\
 & \left. + \alpha(\nu') \cdot R_{BRDF}(\Omega, -\Omega_0, \nu') \cdot E_s(\nu') \cdot \Omega_s \cdot T(-\Omega_0, \infty, z_0, \nu') \right] T(\Omega, z_0, \infty, \nu') \} d\nu' \\
 & \quad \text{(Reflected sunlight term)}
 \end{aligned} \tag{3.5}$$

where

- $L(\Omega, \nu)$  = radiance at frequency  $\nu$  into upward, directed, solid angle  $\Omega$
- $\Phi(\nu, \nu')$  = ILS, i.e. spectral response of  $\nu$  due to incident radiance at  $\nu'$
- $B(\nu, T)$  = Planck function for temperature  $T$
- $T_{surf}$  = surface temperature
- $T(\Omega, z, z', \nu')$  = atmospheric transmittance at frequency  $\nu'$  in a direction  $\Omega$  between altitudes  $z$  and  $z'$
- $\alpha(\nu')$  = surface albedo
- $R_{BRDF}(\Omega, -\Omega', \nu')$  = surface biconical reflectance function for incident (downward) solid angle  $-\Omega'$  and emergent (upward) solid angle  $\Omega$
- $\varepsilon(\Omega, \nu')$  = surface emittance at frequency  $\nu'$  in the upward direction  $\Omega$
- $E_s(\nu')$  = disk-average solar radiance
- $\Omega_s$  = solar solid angle at Earth

The same equation holds for limb emission sounding if the last three (surface-related) terms are omitted. While the equation, therefore, seems much simpler, the geometry of the light path (especially in the lower atmosphere) becomes much more complicated because of strong refraction effects.

Next, a numerical radiative transfer model that was developed for TES will be described. This forward model uses atmospheric temperature and constituent profiles and the surface properties as

inputs. The integrations in equation 3.5 will be carried out numerically by dividing the atmosphere into thin layers. The layer effective quantities, such as the layer effective temperature and pressure, and the layer molecular column amount, are calculated in the ray tracing and path integrals step.

### 3.3.1.1 Ray Tracing and Path Integrals

The lines of sight through the atmosphere must be traced, allowing for the detailed geometry and possible refraction effects. Full details will be found in appendix 3.3.1.1. The basic principles are described here.

The non-sphericity of the Earth is accommodated by using a coordinate system with origin at the center of curvature, at a nominal tangent point, of a reference geoid. In the plane of the ray (refraction horizontally is ignored) the atmosphere is described in terms of functions of radius  $r$  and angle  $\psi$  of the line from the center to the ray element. Quantities in a radially symmetric atmosphere are assumed to be independent of  $\psi$ .

For integrating the hydrostatic equation, a full latitude/altitude model is used for the variation of the acceleration of gravity. The air density is calculated from an equation of state that includes the effect of water, and is not simplified to the perfect gas law. (Appendix 3.3.1.1.7)

For the quasi-nadir case, the ray tracing is evaluated from simple trigonometry, ignoring refraction. Integrals of absorber amounts and temperature are carried out analytically over full grid layers, assuming that  $\ln(q)$  and  $T$  are linear in  $\ln(P)$ .

For the limb case, the approach used is based on that of Kneizys *et al.* (1983). The coordinate  $x = r \cos\theta$  is used along the ray to avoid the singularity at the tangent point. The zenith angle of the ray,  $\theta$ , is obtained from Snell's law for spherical symmetry,  $n(r)\sin\theta(r) = \text{constant}$ , and the distance element  $ds$  along the ray is related by  $dr = \sin\theta ds$ . This can be shown to give

$$ds = dx/[1+(r/n)(\partial n/\partial r)\sin^2\theta(r)] \quad (3.6)$$

which can be used to integrate path integrals with respect to  $x$ , an explicit function of  $r$ , rather than  $s$ . The integrals are evaluated by dividing each full grid layer into sub-layers in  $x$ , such that all quadrature intervals are smaller than a given length, and using a trapezium or higher order quadrature.

When the atmosphere is not radially symmetric, the above ray tracing technique does not apply because we can no longer assume that  $nr\sin\theta = \text{constant}$ . In this case we can use a more general approach and construct a set of three coupled ordinary differential equations in  $r(s)$ ,  $\theta(s)$  and  $\psi(s)$  to describe the ray trajectory. These are integrated forwards from an assumed tangent point to the satellite altitude. The horizontal location of the tangent point as expressed by  $\psi(0)$  is then iterated so that the ray reaches the location of the satellite. Path integrals are evaluated in the same way as for the radially symmetric case, but using the same quadrature points in  $s$  as are used by differential equation integration.

### 3.3.1.2 Ray Tracing (Surface Layer)

The pressure boundaries of the forward model atmospheric layer above the Earth's surface must be redefined for every TES observation. This layer will be thinner than or equal to the TES standard forward model layers near the surface. The sea surface pressure will be obtained from fields obtained from available Numerical Weather Prediction results (e.g. ECMWF, NCEP, DAO, etc.). The earth surface pressure (the lower pressure boundary for the surface layer) will be calculated

from the sea surface pressure using the hydrostatic equation at the TES identified elevation (section 3.3.2.4). The top pressure boundary for the surface layer will be a TES fixed pressure level.

### 3.3.1.3 Optical Depth

The optical depth (OD) along the line of sight for a given layer  $l$  is calculated as

$$\tau(\nu)_l = \sum_m u_{m,l} k_m(\bar{T}, \bar{P}, \nu) \quad (3.7)$$

where the sum is over species,  $u_{m,l}$  is the layer molecular amount for absorber  $m$ , and  $k_m(\bar{T}, \bar{P}, \nu)$  is the absorption coefficient for molecule  $m$ .  $u_{m,l}$ ,  $\bar{T}$ , and  $\bar{P}$  are calculated in the ray-trace and path integral step. Although we will still keep the option of using a line-by-line model to calculate absorption coefficients, for most molecules  $k_m(\bar{T}, \bar{P}, \nu)$  will be pre-calculated at fixed P/T grids and stored in files (ABSCO Tables). Section 3.5 describes the ABSCO Table generation and discusses the  $k_m(\bar{T}, \bar{P}, \nu)$  interpolations in temperature / pressure / H<sub>2</sub>O VMR. The frequency grid spacing of  $\tau(\nu)$  for the line species in the HITRAN list will be 0.0001 cm<sup>-1</sup> (TES tier 1 frequency spacing), small enough to describe a Doppler line in the upper atmosphere.

The cross-section, continuum, and cloud absorption coefficients (section 3.5 and 3.6) will be stored and calculated on a coarser frequency grid spacing, 0.0025 cm<sup>-1</sup>. This is mostly determined by the representative spectral structures shown in some cross-section species, and this coarser frequency spacing is the TES tier 2 spacing.

The total layer optical depth is then calculated by the sum of the tier 1 OD and the interpolated tier 2 OD. The tier 2 to tier 1 interpolation is performed using a 4-point Lagrange interpolation scheme.

### 3.3.1.4 Atmospheric Radiance

The spectral radiance at the satellite is given in equation (3.5). By neglecting the reflected sunlight term the monochromatic radiance may be summarized as

$$L_{sat} = L_L^\uparrow + \epsilon B(T_{sf}) T_{0,L} + \alpha L_0^\downarrow T_{0,L} \quad (3.8)$$

in which  $L_L^\uparrow$  is the upwelling radiance contribution of the atmosphere from the surface to the level at the top of the atmosphere (TOA),  $T_{0,L}$  is the transmittance of the atmosphere and  $L_0^\downarrow$  is the downwelling radiance of the surface. For a specularly reflecting surface,  $L_0^\downarrow$  is calculated for the same zenith angle as  $L_L^\uparrow$  and  $\alpha$  is the appropriate bidirectional reflectance. For a Lambertian surface,  $L_0^\downarrow$  is calculated at the diffusivity angle, the downwelling radiation scattered by the surface is taken to be isotropic and  $\alpha$  is the albedo.

In the limb case, there is no surface term.  $L_L^\uparrow$  is then the radiance contribution from the portion of the atmosphere from the tangent to the satellite and  $L_0^\downarrow T_{0,L}$  would be the radiance contribution from the atmosphere from the far-side space to the tangent along the line of sight.

The upwelling term,  $L_L^\uparrow$ , the downwelling radiance,  $L_0^\downarrow$ , and the total transmittance  $T_{0,L}$  are calculated recursively in a layer loop. For example, in the case that the calculation starts from Earth's surface to satellite,  $L_L^\uparrow$ ,  $L_0^\downarrow$ , and  $T_{0,L}$  are initialized as 0.0, 0.0, and 1.0. At each layer step ( $l$ ), they are updated as (illustrated in Figure 3 - 2)

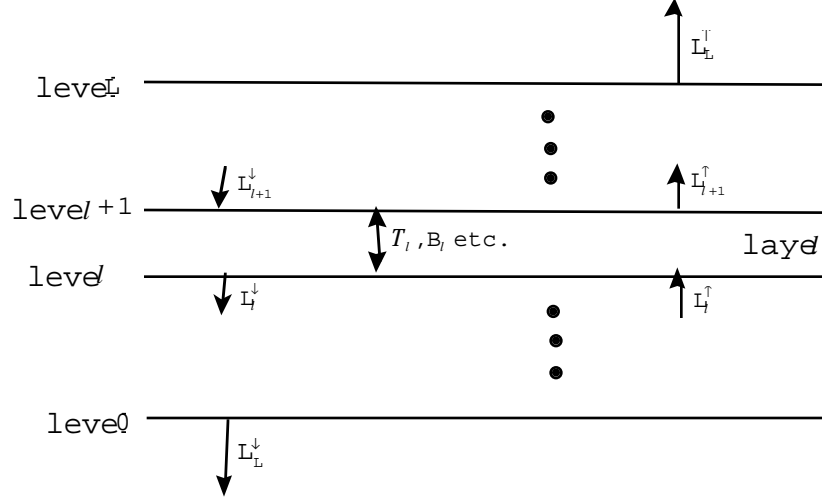
$$L_{l+1}^\uparrow = L_l^\uparrow T_l + (1 - T_l) B_{eff} \quad (3.9)$$

$$L_{l+1}^\downarrow = L_l^\downarrow + (1 - T_l) B_l T_{0,l} \quad (3.10)$$

$$T_{0,l+1} = T_0 T_l \quad (3.11)$$

where  $T_l$  is the layer transmittance which is not necessarily the same for upwelling and downwelling cases ;  $B_l$  and  $B_{eff}$  are the Planck function at layer mean temperature  $\bar{T}_l$  and the layer effective Planck function defined below.

**Figure 3 - 2: Illustration of the recursive radiative transfer calculations**



The layer transmittance  $T_l$  is calculated as

$$T_l = \exp(-\tau_l) \quad (3.12)$$

where  $\tau_l$  is the layer optical depth, as described in 3.3.1.3. Since the exponential calculation is relatively expensive, the linear approximation is used for  $\tau_l$  is less than 0.01 and  $\tau_l$  is taken as zero when  $\tau_l$  is greater than 10.0.

In order to simulate the contribution of the layer emission to the total radiance more accurately, the source term in equation 3.9 uses an effective Planck function defined as

$$B_{eff} = B_l(\bar{T}_l) + [B(T_{l+1}) - B_l(\bar{T}_l)] \left\{ 1 - 2 \left[ \frac{1}{\tau_l} - \frac{T_l}{1 - T_l} \right] \right\} \quad (3.13)$$

where  $B(T_{l+1})$  is the Planck function calculated using the layer upper level temperature,  $T_{l+1}$ . An effective Planck function can be further approximated as

$$B_{eff} = B_l(\bar{T}_l) + [B(T_{l+1}) - B_l(\bar{T}_l)] \left\{ \frac{a\tau_l}{1 + a\tau_l} \right\} \quad (3.14)$$

where  $a$  is an empirical factor with a value of 0.278 [Clough *et al.*, 1981; Clough *et al.*, 1986]. At the two extremes, e.g., optically thin layers,  $B_{eff} \approx B(T_l)$  and optically thick layers,  $B_{eff} \approx B(T_{l+1})$ .

The calculation of Plank function as a function of frequency at the forward model frequency grids ( $0.0001 \text{ cm}^{-1}$ ) is very time consuming. We therefore implemented a piecewise continuous approximation in this calculation. The accurate Plank function is calculated at coarser frequency grids and a linear interpolation is done for the grids in between.

### 3.3.1.5 Non-LTE

In certain circumstances it is necessary to make allowances for departures of the source function  $J$  from the Planck function. This will be most important for the case of nitric oxide, which has significant non-thermal emission from the thermosphere, particularly in the presence of solar activity. This emission can be a significant fraction of the total measured NO signal. To account for Non-LTE the forward model must be able to accept the populations of the individual vibrational levels affected relative to the Boltzmann population, which depends only on temperature. The algorithm to be implemented in the forward model for the calculation of NLTE radiances is provided in Appendix A3.3.1.5.

Two approaches are being explored to obtain NLTE state populations for the TES spectral measurements:

- (1) Estimate the populations of the excited states, using existing models and climatological temperature and solar irradiance values. This will provide a non-LTE climatology to be included as forward model parameters. For NO, retrieve only the mixing ratio in the troposphere and lower stratosphere.
- (2) Retrieve the populations of the affected vibrational levels at all relevant altitudes, as well as the mixing ratio distribution. This would proceed in the same way as retrieval of any other parameter, by including the relative populations in the state vector, and computing the Jacobians for them.

### 3.3.1.6 Radiative Transfer for the Solar Contribution

The contribution to the radiance at the satellite due to scattered solar radiation must be taken into account in the spectral region  $2000\text{-}3050 \text{ cm}^{-1}$ . Experience with HIS spectra suggests that, under solar conditions, there is almost always some solar scattering due to atmospheric hydrometeors and aerosols in addition to the scattering from the surface. Empirical techniques will be developed and utilized to address scattered solar effects in the affected microwindows in addition to the treatment of the scattered radiation from the surface. For the nadir case, the radiative transfer including the surface scattering is given as

$$L_{\text{sat}} = L_L^{\uparrow} + \epsilon B(T_{\text{sfc}})T_{0,L} + \alpha L_0^{\downarrow} T_{0,L} + R_{\text{BRDF}}(90, \theta_{\text{sun}}) J_{\text{sun}} T_{\text{sun}_{0,L}} T_{0,L} \quad (3.15)$$

where  $J_{\text{sun}}$  is the solar source function at the top of the atmosphere,  $T_{\text{sun}_{0,L}}$  is the transmittance of the atmosphere along the solar refracted path and  $R_{\text{BRDF}}(90, \theta_{\text{sun}})$  is the surface bidirectional reflectance.

The solar contributions will be calculated at the monochromatic wavenumber grid. The appropriate Doppler shift and radiance adjustment due to the distance of the Earth to the sun will be taken into account. Treatment of these effects involves minimal computation time.

The method of calculation will be to use an effective secant for the solar path in each layer, thus making use of the optical depth calculation being done for the upwelling atmospheric radiation. The reference radiative transfer model will have the capability to treat solar scattering in the single

scattering approximation at each layer given a profile of scatterers and their optical properties. The initial approach for the limb will be to remove spectra that are strongly contaminated by solar scattering in the 2000-3050  $\text{cm}^{-1}$  spectral domain, recognizing that if strong aerosol conditions exist, appropriate methods will be applied to extract as much information as possible for species optically active in this region [Rinsland *et al.*, 1994].

### 3.3.1.7 Surface Contribution

The radiance at the satellite including the effects of scattering and reflection at the surface may be written as,

$$L_{\text{sat}} = L_L^{\uparrow} + \epsilon B(T_{\text{sfc}}) T_{0,L} + \alpha L_0^{\downarrow} T_{0,L} + R_{\text{BRDF}}(90, \theta_{\text{sun}}) J_{\text{sun}} T_{\text{sun}0,L} T_{0,L} \quad (3.16)$$

where  $J_{\text{sun}}$  is the solar source function at the top of the atmosphere,  $T_{\text{sun}0,L}$  is the transmittance of the atmosphere along the solar refracted path and  $R_{\text{BRDF}}(90, \theta_{\text{sun}})$  is the surface bidirectional reflectance. The terms associated with the upwelling radiance of the atmosphere, the surface emitted radiance and the surface reflected solar radiance can be treated rigorously assuming that the surface emittance is isotropic with emissivity  $\epsilon$  and that  $R_{\text{BRDF}}(90, \theta_{\text{sun}})$  properly describes the solar scattering by the surface. The radiance due to the surface scattering of the downwelling irradiance is a rather more complex problem. First, this term is assured not to be large: if the atmosphere is in the optically thin regime then the downwelling flux is small, and is further reduced by the surface albedo so that the radiance at the satellite is dominated by the surface emitted radiance attenuated by the satellite. In the optically thick regime, there is no contribution from other than upwelling radiance of the atmosphere. As a consequence of this perspective, the accuracy of the forward model radiance at the satellite is not highly dependent on the accuracy of the value for the albedo or on the accuracy of the calculation of the downwelling irradiance.

The scattering due to the surface is characterized as either Lambertian or specular. For the Lambertian case, the downwelling irradiance,  $L_0^{\downarrow}$  is required. This is obtained by performing the radiance calculation along the diffusivity ray (secant = 1.66) [Goody and Yung, 1989]. The product of this radiance and the albedo provides an excellent approximation to the scattered upwelling isotropic radiance at the surface. The motivation for this approach is the low computational cost with acceptable accuracy. The layer optical depth for the diffusivity angle is obtained by multiplying the nadir layer optical depth by the secant angle. Although an additional exponential is required, this approach is faster than alternative methods. In general, the albedo will be taken as  $1-\epsilon$  with  $\epsilon$  a retrieved parameter.

In the case of specular reflection,  $\alpha$  assumes the role of a bidirectional reflectance, e.g.  $R_{\text{BRDF}}(90, 90)$  for the nadir case. The downwelling radiance is calculated for the same secant as the upwelling (secant = 1 in the nadir case) and the same layer transmittances are used for both the upwelling and downwelling radiances. This calculation is fast and has full accuracy.

The spectral variation of the emissivity and effective albedo function is slow in relation to the molecular spectral absorption and the resolution of the TES instrument, enabling the implementation of Eq. 3.16 to be performed after the spectral convolution associated with the instrument function. The extra time required for the FFTs for the three contributions is partially compensated by the reduced computational effort. In any case this approach greatly facilitates the retrieval of the surface properties without the recomputation of the atmospheric contribution.

### 3.3.1.8 Simultaneous Multiple Rays

Two computationally expensive stages in the calculation of the radiance at the satellite for a given ray in the limb mode are the calculation of the spectral absorption coefficients and the calculation of the spectral radiative transfer. With the exception of the tangent layer the absorption coefficients required to calculate optical depths are the same in a given layer for all rays passing through that layer under the assumption that the layers are spherically symmetric. Consequently, given the optical depths for a given ray through a layer, the optical depths for all other rays through the layer may be obtained by multiplying this optical depth by the appropriate ratio of the integrated path amounts of dry air for the other rays. For the tangent layer (and perhaps the adjacent layer) the pressure and temperature are different from that of the prestored pressure grid and the absorption coefficients must be obtained specifically for the ray through tangent layer. Using an approach that retains the information required for the calculation of the required optical depths for all rays in this fashion, essentially eliminates the cost of multiple lookups of absorption coefficients and with the subsequent calculations of the optical depth. The additional quantities to be stored in the general case is small, namely the number of tangent rays. We refer to this approach for the limb as a simultaneous multiple ray approach, since the information for all rays to the satellite is obtained with a single detailed calculation of optical depth in each layer plus one extra for each tangent layer.

Certain savings of this type can also be achieved in the radiative transfer, principally the calculation of the Planck functions. However, the computational cost of the Planck functions in our current implementation is sufficiently small that the gain in treating the multiple tangent rays simultaneously may not be warranted.

### 3.3.1.9 Horizontal Inhomogeneity

At the limb, the path length through the tangent layer can be many tens of kilometers. Consequently, the assumption that the atmosphere is homogeneous in composition and physical state may not be valid. It further follows that the ensuing discussion is tentative and subject to “lessons learned” once we are on orbit.

The approaches that we shall investigate (in order) are

- 1) Ignore Line-of-Sight (LOS) gradients in the forward model, retrieve a single profile from a single set of spectra, and include the effect in the error analysis (*i.e.* if a gradient exists, the residuals will increase).
- 2) Assume some known LOS gradients in the forward model. For temperature/pressure this can come from NCEP/ECMWF/DAO data. For constituents it can come from a first pass using method (1). This approach has been used by LRIR, LIMS, and ISAMS.
- 3) First perform a “nadir-type” retrieval (but with cold space rather than the Earth’s surface as background) *along the LOS*. The weighting and contribution functions will be strongly peaked in the tangent layer, but this is where inhomogeneity will have most of its impact. Use the results (one for each pixel) as a first guess for the standard limb retrieval.
- 4) Retrieve the 2-D distribution (or at least a mean profile and a profile of the LOS gradient) from a single set of spectra. If horizontal inhomogeneity has a measurable effect on the radiances, then there is, in principle, information about it from which it might be retrieved. However this information might also alias into something else. Only numerical experiments can tell the difference.
- 5) Simplified tomography by sequential estimation. For example, consider successive profiles at the locations corresponding to three successive measurements. Call them A, B, and C in time

order. Set up an *a priori* (see later). Use the B spectra to retrieve all three profiles jointly. The result gives the final retrieval for the A profile. The retrievals so far for B and C become *a priori* for the next cycle, and *a priori* for D, the next location, are obtained by a combination of, for example, climatology and extrapolation. Now use the C spectra to retrieve B, C, and D jointly. This gives the final retrieval for B and the C and D *a priori* for the next cycle. Repeat.

### 3.3.2 Surface Model

#### 3.3.2.1 Surface Radiative Properties

TES nadir data will have many spectral regions that contain information about the surface radiative properties, (“window” regions). As discussed in 3.3.1, unless we have additional information about the bi-directional reflectance, the surface model must choose either a Lambertian or specular reflectance approximation for the forward model calculation. For either case, we will assume that the albedo is  $1-\epsilon$ , where  $\epsilon$  is the emissivity. For any forward model frequency,  $\nu$ , the emissivity is calculated from a linear interpolation. We can then model the surface contribution with a single “skin” temperature and the emissivity spectrum, which gives us the flexibility to adjust the emissivity structure for specific target types.

The *a priori* emissivity values will be obtained from a database structured by month and lat/lon coordinates. To populate the database, we will use a combination of ASTER emissivity products, where available, and emissivities derived from knowledge of the seasonal land cover characteristics. Although ASTER will have a very coarse spectral resolution, (5 channels between 8 and 12  $\mu\text{m}$ ), it measures the reflective properties of actual nadir targets from space. For land nadir target scenes where we do not have measured emissivities, we will generate the emissivity first guess using the seasonal land characteristics for the target spot and weighted emissivity spectra for the specific materials (e.g., deciduous trees or dry grass) that are likely to be present. Note that the preponderance of our nadir targets are either water or ice, which have reasonably well known emissivities [Smith *et al.*, 1996 and Masuda *et al.*, 1988].

#### 3.3.2.2 Map of Earth Surface Composition

In order to arrive at a reasonable first guess of emissivity, or where appropriate, the bi-directional reflectance for a target surface scene, we will need an up-to-date estimate of the seasonal land cover for the latitude and longitude of each pixel in a given nadir view. Since the footprint of an individual pixel is approximately 0.5 by 5 km, a database with spatial resolution of order 1 km (or 32 arc-seconds) should suffice. An existing database of land cover characteristics with 1 km resolution is described in Appendix 3.3.2.3. This database can be used for our initial algorithm development and testing, however, it is also important to note that improved databases, tailored more to the needs of infrared spectral remote sensing, should be available by TES launch.

For the TES Level 2 algorithm to access this type of data efficiently, the global maps will likely need to be reformatted from separate seasonal images to a look-up table of land cover type vs. season or month, latitude and longitude. The land cover type from the table would then specify the emissivity function to be used in the first guess of the surface model parameters. If a particular land cover type required further differentiation, such as snow/ice or dry/wet grasslands, additional information, if available, could be employed. If no additional information were available, default values for the emissivity of the ambiguous land cover type would be used.

#### 3.3.2.3 Digital Elevation Model

The digital elevation map (DEM), together with NCEP sea level pressures and the hydrostatic equation, are used to estimate the surface pressure at the location of an observation for nadir



retrievals. The DEM simply provides the difference in altitude between the location of an observation and sea-level pressure reference geoid. Integration of the hydrostatic equation, using this elevation difference and the *a priori* temperature profile, gives an estimate of the surface pressure.

There are a number of global DEMs available. The only issue is horizontal resolution and vertical accuracy. The highest spatial resolution DEMs with global coverage are limited to latitude-longitude bins of 5 arc-minutes. At the equator this corresponds to an area of 9.28 x 9.28 km<sup>2</sup>, somewhat larger than the 8.5 km along track by 5.5 km cross-track nadir footprint of (i.e. the coverage of a 16-pixel TES detector array). The altitude at the pixel is estimated from a 2 dimensional linear fit and interpolation of the DEM elevations along the spacecraft track.

The requirements for DEM altitude accuracy is driven by the requirement that errors in total column density be less than 0.5%. This translates into a maximum allowable elevation error of about 42 m near sea level.

A candidate map is the ETOPO5 5-arcminute gridded elevation data:

<http://www.ngdc.noaa.gov/mgg/global/etopo5.html>

This DEM is maintained by and available *via* ftp from NOAA's National Geophysical Data Center:

<http://www.ngdc.noaa.gov/seg/fliers/se-1104.html>

The map was assembled from a variety of data sources with varying horizontal resolutions and vertical accuracies. The USA, Europe, Japan and Australia are true 5-minute data with vertical resolutions of 1 m. Data for Africa, Asia, and South America vary in resolution from  $\pm$  a few meters to as much as 150 meters in the vertical and in few data deficient areas were assembled from 1 degree horizontal resolution data.

Another candidate data set is the GTOPO30:

<http://www.ngdc.noaa.gov/seg/globsys/globe.html>

under development at NOAA's National Geophysical Data Center. It improves upon the ETOPO5 map with increased horizontal resolution (30-arc-second or 1 km grid). Currently, this map covers about 60% of the Earth's land surface. It is anticipated that this data set will cover the Earth's complete land surface before launch of the CHEM platform.

The EOS Product Generation Software Tool-Kit provides routines to extract the elevation data from both of these DEMs.

### 3.3.3 Radiative Transfer for Aerosols

The capability to treat aerosol radiative effects is an important aspect of the radiative transfer to be included in the forward model. The principal contributions to the radiative transfer associated with aerosols are somewhat different for the nadir and limb viewing modes. In the nadir mode the principal contribution is from boundary layer aerosols in the most common case with the flux driven by the radiance associated with the surface. In the limb mode, the dominant contribution to the spectral radiance along the line of sight will originate in the tangent layer with scattering into and out of the beam in that layer. To obtain an acceptable estimate of the scattering effects, the up and down welling fluxes or reasonable proxies are required. The approach to the problem of developing a satisfactory algorithm for an operational code for scattering atmospheres will be to obtain simulated radiances including aerosol multiple scattering using radiative transfer codes of

high accuracy ( e.g. DISORT and CHARTS; Moncet and Clough, 1997), for typical TES viewing geometries. Using these simulated radiances, a number of modifications to the radiative transfer algorithm will be explored. It is anticipated that different algorithms will be developed for the nadir and limb viewing cases.

The initial approach will be to use a two stream approximation to see how well the simulated radiances can be modeled. Assuming that a single scattering approach is sufficient, we will develop an accelerated algorithm that adapts elements of the two stream approximation, re-using as much of the clear sky forward model algorithm as possible. It is anticipated that the aerosol properties to be required by the forward model are the effective path length, the aerosol extinction coefficient, and an effective single scatter albedo. It is important to note that a full residual spectrum will be available at the conclusion of the TES retrieval process. These residual spectra (or averages of residual spectra) will enable us to search for aerosol spectral features and possibly retrieve some of the aerosol properties.

### 3.3.4 Solar Source Function

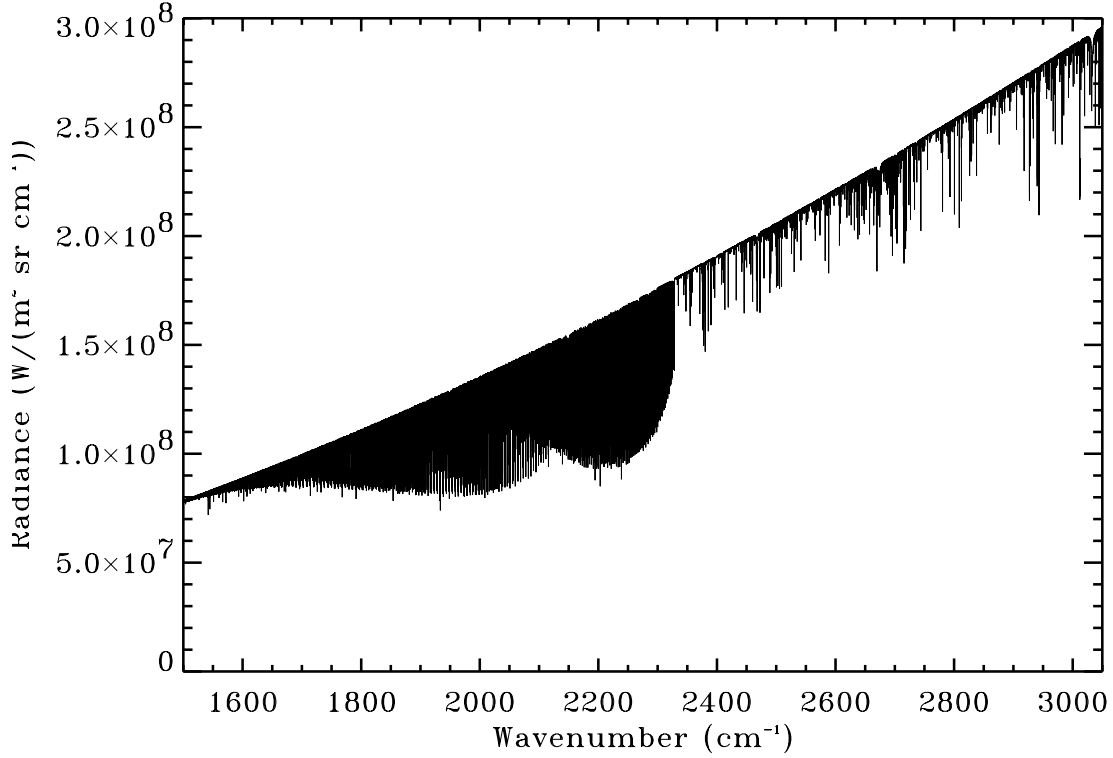
Extraterrestrial solar radiance will contribute to the TES observed radiance in the 2000-3050  $\text{cm}^{-1}$  spectral regime. In order to accurately model the impact of the solar source radiance in the spectrum, the solar source function of Kurucz [1995, 1992, 1984], shown in Figure 3 - 1, is used in the forward model. It is the result of a radiative transfer calculation based upon solar measurements, including those of ATMOS [Gunson *et al.*, 1996], with a resolution of 0.0040  $\text{cm}^{-1}$  at 2000  $\text{cm}^{-1}$  and 0.0061 at 3050  $\text{cm}^{-1}$ . The spectra are interpolated and stored on a 0.0001  $\text{cm}^{-1}$  grid.

Given the solar function  $J_{\text{SUN}}$ , total transmittance through the atmospheric path  $T_{0,L}$ , and surface albedo  $\alpha$ , the solar contribution to the radiance observed at the satellite  $L_{\text{SUN}}$  is given as

$$L_{\text{sun}} = J_{\text{sun}} T_{0,L} \alpha, \quad (3.17)$$

where  $\alpha=1$  in limb viewing mode. This source function results from a spatial integration over the solar disk and is provided at monochromatic resolution. For radiative transfer calculations using the solar source function, the proper Doppler shifts between the scattering medium (nadir view) and the sun must be applied to the spectrum.

**Figure 3 - 3: Monochromatic solar spectrum over the spectral region relevant to TES (Kurucz, 1995).**



### 3.3.5 Instrumental Line Shape Spectral Convolution and Apodization

The measurement of radiance by off-axis detectors introduces self-apodization, frequency scaling, line broadening, and asymmetry to the instrumental line shape (ILS). These effects can be modeled analytically. For a known spatial illumination, this model leads to a technique that corrects for most of the off-axis effects in Level 1B processing, but does not remove the residual asymmetry in the ILS. As a result, this asymmetry must be modeled in Level 2. A detailed description of this algorithm and a sensitivity analysis to model errors in illumination are presented in the TES Level 1B ATBD.

Additional apodization may also be applied to the measurement and forward model spectra in order to facilitate retrievals on microwindows. The choice of apodization functions for a given retrieval is discussed in Section 3.8.7.

### 3.3.6 Field-of-View Spatial Convolution

The TES forward model derives the effective radiative response of a pixel at the satellite by performing a trapezoidal integration of the Field Of View (FOV) function with the representation of the radiance field provided by multiple rays originating at specified tangent points. The set of refracted path radiances,  $L(\theta_k)$ , is obtained by running the forward model over TES prescribed tangent pressure levels,  $k=0, \dots, N$ , with corresponding zenith angles at the satellite,  $\theta_k$ . The TES instrument spatial FOV function  $\Psi_{FOV}$  is stored on an angular grid  $\theta_j, j=0, \dots, \hat{N}$  appropriate for the trapezoidal integration. The forward model radiances,  $L(\theta_k)$ , are interpolated to match the  $\Psi_{FOV}$  grid

using a four point Lagrange method for unequally spaced points with continuous first derivatives and are then convolved with  $\Psi_{FOV}$  to obtain the effective radiance at the detector. The calculated radiance at the satellite  $L_{sat}$  is given as

$$L_{sat} = \sum_j L(\theta_j) \Psi_{FOV}(\theta_j), \quad (3.18)$$

where

$$L(\theta_j) = a_{-1} L(\theta_{k-1}) + a_0 L(\theta_k) + a_1 L(\theta_{k+1}) + a_2 L(\theta_{k+2}) \quad (3.19)$$

The Lagrange coefficients  $a_{-1}$ ,  $a_0$ ,  $a_1$ , and  $a_2$  are defined as follows:

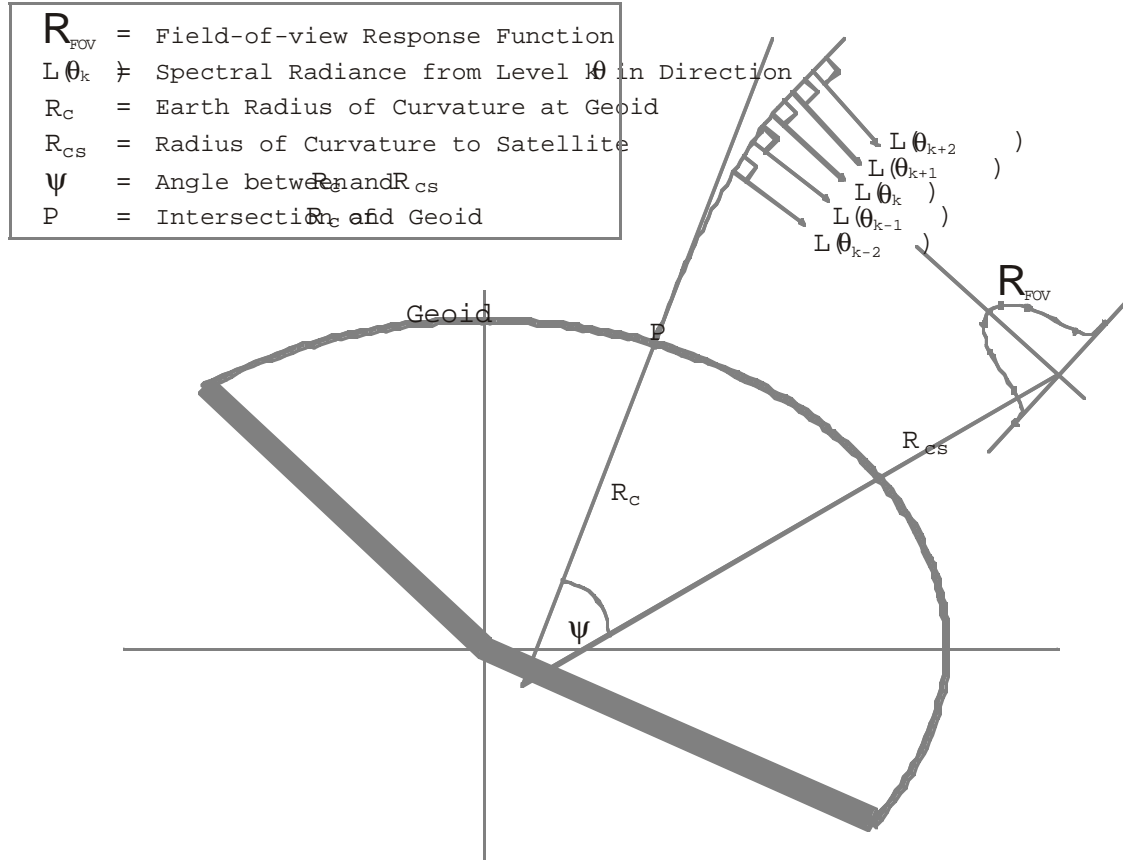
$$\begin{aligned} a_{-1} &= p(-1+2p-p^2)(1+c_1) \\ a_0 &= p^2(2p-3+(1-p))(1/(1+c_2))+1 \\ a_1 &= p^2((3-2p)+p((1-2p+p^2)(1/(1+c_1)))) \\ a_2 &= p^2((-1+p)(1/(1+c_2))) \end{aligned}$$

with

$$\begin{aligned} c_1 &= (\theta_k - \theta_{k-1})/(\theta_{k+1} - \theta_k) \\ c_2 &= (\theta_{k+2} - \theta_{k+1})/(\theta_{k+1} - \theta_k) \end{aligned}$$

The usual fractional interpolation parameter  $p$  corresponds to the fractional angular distance between rays designated  $\theta_k$  and  $\theta_{k+1}$ . Analytic partial derivatives of  $L_{SAT}$  with respect to  $\theta$  can be calculated at little computational cost from the expression obtained by differentiating  $L(\theta)$  with respect to  $\theta$ . These derivatives are required for the Jacobian used for the retrieval of pointing angle (see Section 3.8.4.2.3).

**Figure 3 - 4: Diagram for TES pointing geometry and FOV convolution in limb mode**



### 3.3.7 Absorption Coefficient (ABSCO) Tables

#### 3.3.7.1 ABSCO Table Generation (Using LBLRTM)

The absorption coefficients for a given molecular species as functions of pressure, temperature, and frequency will be pre-calculated and stored using TES LBL (a line-by-line code described in next section) without any line rejection approximation. The corresponding pressures will be the TES forward model layer effective pressures pre-calculated using US standard global average temperature profile. At each pressure, about ten temperatures are calculated at every 10 K. A  $\pm 60$  K temperature band centered at the US standard atmospheric temperature profile [1976 US Standard] is used to limit the temperature grids at a given layer.

Temperature interpolation for total layer optical depth, which is the sum of the layer optical depths for all the molecules considered, will be performed to interpolate OD at pre-defined temperature grids to the TES retrieved atmospheric layer effective temperature. The interpolation scheme will be a three-point Lagrangian method. The pressure interpolation for the layer optical depth will not be required except for the surface layer in the nadir case and for the tangent layer in the limb case. Detailed discussions and validations of this pressure interpolation issue are in section 3.3.7.4.

In the case of tropospheric water vapor, the self-broadening effect cannot be neglected. The  $H_2O$  volume mixing ratio ( $q$ ) is therefore another variable in the ABSCO tables for tropospheric  $H_2O$ . Since the dependence of the  $H_2O$  absorption coefficient on its  $q$  is nearly linear for a given

temperature and pressure, we use linear interpolation/extrapolation in  $q$  to calculate the  $H_2O$  absorption coefficient at layer  $H_2O$  effective  $q$  for the three temperature grids before doing the temperature interpolation described above. The two tabulated  $q$  grids are for extremely dry air,  $q_{dry} = 10^{-8}$ , and for 90% of the saturation  $q$  at the given temperature and pressure grid,  $q_{wet} = 0.9 * q_{sat}$ .

In general, by comparison to real time line-by-line calculations of ABSCO, the advantage of table lookup is to speed up greatly the calculation of the required spectral optical depths. However, there are spectral regions in which lines are sparse for a given molecular species. In these cases, the computational cost of the line-by-line calculation may be comparable or faster. The evaluation of this situation is underway which include exploring the data computations and accelerated interpolations. TES team has started to study the data storage issue. In the light of using spectral microwindows for TES retrievals and the advancing of the computing technology, it seems that it is not very difficult to handle the required storage for TES ABSCO table files.

The effect of interpolations (temperature, pressure, and tropospheric  $q$ ) on TES retrievals will be examined thoroughly. Preliminary studies for a nadir case show that comparing to the spectral radiance calculated by line-by-line code, the radiance differences are less than 0.5%. A significant advantage of the ABSCO approach is that the accuracy of the absorption coefficient calculation is not limited in any way by computational cost considerations. In addition, the spectral absorption coefficients are readily amenable to empirical adjustment as atmospheric measurements may suggest for improved retrievals.

### 3.3.7.2 TES Line-by-Line Code

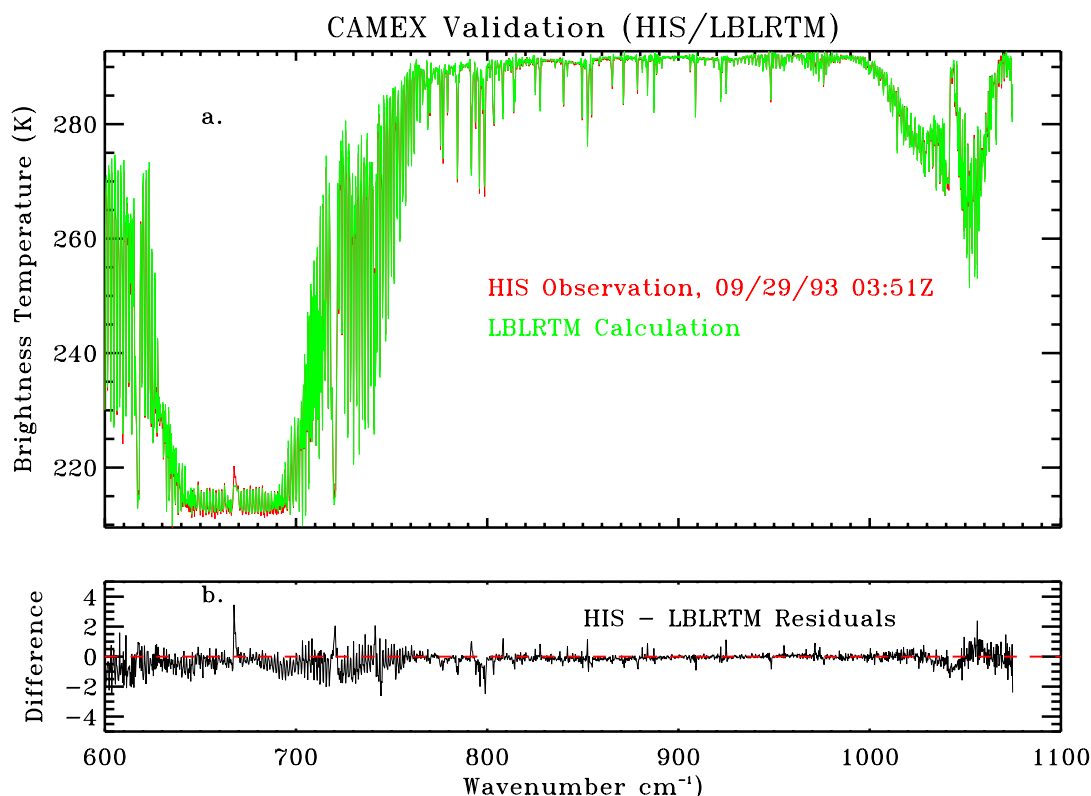
The line-by-line model being developed for TES (TES\_LBL) to calculate spectral absorption coefficients is an advanced version of the module performing the comparable operation in LBLRTM (e.g. Clough *et al.*, 1995) which itself is based on the FASCOD line by line model [Clough *et al.*, 1981]. These models have a long history of validation in the spectral radiative transfer community. TES\_LBL is being developed to calculate only spectral absorption coefficients, to provide greater algorithmic accuracy, to be reasonably efficient and it is to be written such that the connection between the physics and the coding is more apparent. TES\_LBL is being developed (1) to be run off line for the generation of absorption coefficients for a lookup table to be used subsequently in the radiative transfer calculation; or (2) to be incorporated directly into the forward model to be used as part of the online radiative transfer calculation. In the latter case options will be invoked to accelerate the calculation with some small loss of accuracy, e.g. line rejection.

TES\_LBL includes the following important attributes: (1) the Voigt line shape is used at all atmospheric levels with an algorithm based on a linear interpolation between precalculated Voigt functions; (2) all relevant parameters from line databases including HITRAN are utilized including the pressure shift coefficient, the halfwidth temperature dependence and the coefficient for the self-broadening of water vapor; (3) an improved version of the TIPS (Total Internal Partition Sum) program is used for the temperature dependence of the line intensities [Gamache *et al.*, 1990]; (4) the effects of line coupling are treated to second order with the coefficients for carbon dioxide in the 600 - 800  $cm^{-1}$  region included explicitly [Hoke *et al.*, 1988]; (5) an explicit formulation is included to address the non-Lorentzian behavior of the wings of carbon dioxide lines. For molecules having an associated continuum, the spectral absorption coefficient calculation utilizes a line shape such that the result of combining the line and continuum contributions provides the correct result.

There have been extensive validations of the LBLRTM model against both upward and downward radiance observations taken by a number of different instruments for a range of atmospheric conditions [Tobin *et al.*, 1999; Mlawer *et al.*, 1997; Clough and Iacono, 1995; Clough *et al.*,

1992]. The assessment of this model has principally been accomplished under the DoE ARM program. In general, the spectral residuals from these validations have been acceptably low for the purposes of TES. There are spectral regimes where continuing evaluation and improvement is required, including the 650-800  $\text{cm}^{-1}$  carbon dioxide region, the methane region at 1300  $\text{cm}^{-1}$ , and the carbon dioxide bandhead at 2385  $\text{cm}^{-1}$ . The magnitude of the residuals is such that errors including the specification of atmospheric state, line parameters and instrument function are of similar order as those of the model errors presenting a significant challenge to model improvement.

**Figure 3 - 5: Observed HIS spectrum and LBLRTM calculated results in equivalent brightness temperature for CAMEX case (a) and observed-calculated differences (b). The nadir measurement was taken from 20 km on the NASA ER2.**



As an indication of the current level of model performance for a portion of the longwave spectral region, we provide in Figure 3 - 5a a radiance spectrum in equivalent brightness temperature obtained with the U. of Wisconsin High-resolution Interferometer Sounder (HIS). The data were taken from the NASA ER2 aircraft during the 1993 Convection and Moisture Experiment (CAMEX) aircraft at an altitude of 20 km in a nadir view over the ocean. The resolution of the unapodized spectrum is 0.22  $\text{cm}^{-1}$  (hwhm). The absolute radiometric calibration is better than 1K with the relative calibration better than 0.5K. In Figure 3 - 5b we indicate the difference between the brightness temperature spectrum of Figure 3 - 5a and a calculated spectrum utilizing LBLRTM with the HITRAN96 line parameter database [Rothman *et al.*, 1998]. Despite the limitation that the atmosphere utilized for the validation was obtained from radiosonde data that was neither co-spatial nor co-temporal, the comparison is extremely good. The surface temperature and emissivity have been adjusted to minimize the brightness temperature differences in the atmospheric window region. The ozone residuals in the 1000-1100  $\text{cm}^{-1}$  region have been improved by utilizing a retrieved ozone profile obtained from the spectral data. The effects of heavy molecules including  $\text{CCl}_4$ , CFC11 and CFC12 have been into account. Carbon dioxide line coupling effects have been

accounted for using the temperature dependent first and second order coupling coefficients of Hoke *et al.* [1988]. The sharp spectral residual at  $668\text{ cm}^{-1}$  is actually due to warmer carbon dioxide in the instrument area rather than to line coupling effects. The regularly spaced spectral residuals in the  $600\text{--}650\text{ cm}^{-1}$  and  $700\text{--}760\text{ cm}^{-1}$  regions are associated with carbon dioxide and are either due to remaining issues with carbon dioxide line shape or with problems with the characterization of the instrument function.. The remaining relatively random residuals in this spectral region are associated with water vapor and are related to errors in the halfwidths and strengths of the weak water vapor transitions, predominantly transitions in the pure rotational band. A contribution to the spectral residuals undoubtedly results from errors in the atmospheric temperature and humidity profiles. Of particular note is the high quality of the spectral radiance data in terms of the photometric calibration, the noise and the spectral calibration.

### 3.3.7.3 Cross-Section Code

Similar to the table look up / temperature interpolation strategy used for the absorption coefficients of line molecules, the cross-section data table for heavy molecules will also be pre-generated at pre-defined pressure and temperature grids. These layer pressure and temperature grids will be the same as the grids used for the line species (section 3.3.7.1). The 3-point Lagrangian interpolation scheme will also be used for temperature interpolation. Section 3.3.8.2 and the associated appendix discussed the method used for temperature/pressure interpolations from the laboratory measurement grids to the TES table  $T/P$  grids.

### 3.3.7.4 Pressure Interpolation

An advantage of using fixed pressure levels bounding the TES forward model atmospheric layers is the ability to ignore the interpolation of species absorption coefficients in pressure at all layers except two: the layer nearest the Earth's surface in the nadir case, and the tangent layer in the limb case. We have conducted a study to examine the changes in layer effective pressures for all the possible layer atmospheric temperature gradients and the effect of pressure interpolation on the simulated spectral radiance.

With a fixed layer boundary pressure, the change in the layer effective pressure ( $\bar{P}$ ) depends mainly on the changes of the boundary temperatures and on the instrument viewing direction. Fifteen averaged temperature profiles of 1997 are calculated using data obtained from the NOAA CDC site (<http://www.cdc.noaa.gov/cdc/reanalysis>): global averaged, global maximum, global minimum, four seasons for tropics, four seasons for mid-latitude, and four seasons for the polar region. We also constructed an extreme temperature profile:  $\pm 20\text{ K}$  on odd and even levels of the global averaged temperature points, respectively. These temperature profiles are used to calculate the layer effective pressures for 24 atmospheric layers between 1000 and 10 hPa for three TES viewing modes: nadir angle = 0, nadir angle =  $45^\circ$ , and a limb viewing case. A standard  $\bar{P}$  profile is calculated using the global average temperature profile and for the nadir angle = 0 case. This standard layer effective pressure profile is the pressure profile used to generate the species absorption coefficient tables.

In the two nadir cases, the layer  $\bar{P}$  for the considered temperature profiles are seen to be extremely close to the standard  $\bar{P}$  profile. The unrealistic temperature profile results in less than 0.3% differences in  $\bar{P}$ , and all the other realistic temperature profiles result even small differences in  $\bar{P}$  (less than 0.11%).

In the limb case, the largest disagreement in  $\bar{P}$  occurs at the tangent layer ( $\sim 3.2\%$ ) for all the temperature profiles, comparing to the nadir standard  $\bar{P}$ . The differences in the layer next to the tangent layer are reduced to about 0.5%. We also found that the effect of different temperature profiles on the limb tangent layer  $\bar{P}$  is very small, which means that we may need a standard limb tangent layer  $\bar{P}$  profile for the limb case if the  $\sim 3.2\%$  difference is a problem in the level 2 process.



In conclusion, the standard  $\bar{P}$  profile calculated using global averaged temperature profile for TES nadir ( $\theta = 0^\circ$ ) mode can be used as the pressure grids for the absorption coefficient tables, and the interpolation in pressure is not needed for most cases. The two exceptions are the limb tangent layer and the surface layer. In the case of the limb tangent layer, the absorption coefficient table at the standard limb tangent layer  $\bar{P}$  profile calculated using global averaged temperature profile for TES limb mode may be needed. In the case of the surface layer, which will be thinner than our fixed layers near the surface, the option would be to perform pressure interpolation if it is necessary. The preliminary comparisons of spectral radiances using the standard  $\bar{P}$  profile and the “real”  $\bar{P}$  profiles strongly support this conclusion (the radiance differences for the nadir case are less than 0.05% and for the limb case are less than 0.1%).

### 3.3.8 ABSCO Databases

#### 3.3.8.1 Line Parameters

The line-by-line portion of the TES spectroscopic database contains transitions for individual infrared active molecular species and their isotopomers within the spectral range defined by the TES nadir and limb observations. The numbering of the species, the format and definition of the parameters, and the contents of the TES spectral parameters database are currently identical to those in the 1996 HITRAN compilation [Rothman *et al.*, 1998]. The status and quality of the HITRAN parameters have been reviewed by Rothman *et al.* [1998]. Here we highlight the known, key limitations of the 1996 HITRAN parameters for the molecules and spectral regions of importance to TES, laboratory work in progress, and published results not incorporated in HITRAN. As was done for the ATMOS project [Brown *et al.*, 1996], the TES spectroscopic database will be updated to satisfy the specific needs of the TES project. The discussion, shown in Appendix 3.3.8.1, proceeds on a molecule-by-molecule basis, with the anticipated changes described for each molecule in ascending wavenumber order.

#### 3.3.8.2 Cross-Sections

For heavy molecular species such as chlorofluorocarbons (CFC's), hydrochlorofluorocarbons (HCFCs),  $\text{SF}_6$ ,  $\text{N}_2\text{O}_5$ , and, in part,  $\text{ClONO}_2$ , spectral absorption cross-sections measured at atmospheric conditions are required [Massie *et al.*, 1985; Camy-Peyret *et al.*, 1987 and Massie and Goldman, 1992]. This is essential, since the small rotational constants, low vibrations and strong hot bands of such molecules preclude complete modeling of the individual line transitions. The 1986 and 1992 editions of the HITRAN compilation introduced temperature-dependent cross-sections but neglected the effect of pressure broadening [Ballard *et al.*, 1988, McDaniel *et al.*, 1991; Massie *et al.*, 1991; Cantrell *et al.*, 1988]. More recently, pressure-temperature cross-sections sets have become available [Varanasi *et al.*, 1992a; Varanasi, 1992b; Varanasi, 1992c].

The absorption cross-section,  $\kappa_\nu$ , is defined as

$$\kappa_\nu = (-\ln T_\nu)/nL \quad (3.20)$$

in terms of the spectral transmittance  $T$  at wavenumber  $\nu$ , temperature  $T$  and pressure  $P$ , of column density  $n$  along an optical path of length  $L$  (cm). It is presented at several  $(T,P)$  combinations representing atmospheric layers given in commonly tabulated atmospheric models as well as conditions encountered in the polar regions.

Table 3 - 1 shows the datasets that have been adapted for TES, from an updated set of measurements provided by Varanasi [private communication, 1997]. These form an extension of

the cross-sections of CFC-11, CFC12, HCFC-22, and SF<sub>6</sub> provided by Varanasi for 1996 HITRAN [Varanasi and Nemtchinov, 1994; Li and Varanasi, 1994; Varanasi *et al.*, 1994; Rothman *et al.*, 1998], and also include CF<sub>4</sub>. The cross-sections of CCl<sub>4</sub> listed in 1996 HITRAN, which originate from the work of Orlando *et al.* [1992] have been replaced by those of Varanasi, for TES. These cross-sections were measured using a high-resolution Fourier-transform spectrometer. For these species, a spectral resolution of 0.03 cm<sup>-1</sup> was used for most of the broadening pressures used in the experiments, while at 40 torr and lower 0.01 cm<sup>-1</sup> was used. The data were obtained at temperatures between 180 and 296 K and are free from instrumental distortion, since the spectra were recorded at a spectral resolution that was sufficiently high at each broadening pressure used.

**Table 3 - 1: IR cross-section data prepared for TES**

<i>Molecule</i>	<i>Wavenumber Range (1/cm)</i>	<i>Temperature Range (K)</i>	<i>Pressure Range (torr)</i>	<i>Number of P,T sets</i>
CCl <sub>4</sub>	770-812	208-297	8-760	32
CFC-11	810-880	190-296	8-760	55
(CCl <sub>3</sub> F)	1050-1120	190-296	8-760	55
CFC-12	810-965	190-296	8-760	51
(CCl <sub>2</sub> F <sub>2</sub> )	1040-1200	190-296	8-760	51
HCFC-22	760-860	216-294	40-760	7
(CHClF <sub>2</sub> )				
SF <sub>6</sub>	925-955	216-295	25-760	7
CF <sub>4</sub>	1250-1290	180-296	8-760	54
HFC134a	1000-1350	253-287	0	3
(CFH <sub>2</sub> CF <sub>3</sub> )				

For the purpose of TES codes, the cross-sections, which are originally given at different spacings (chosen according to resolution and pressure) were interpolated to a constant step of 0.0025 cm<sup>-1</sup>. A special P-T interpolation was devised for conditions different from the laboratory data. Table 3 - 1 shows the data sets prepared on the TES system and Appendix 3.3.8.2 describes the P-T interpolation program XSFINT.

The data are stored in HITRAN format, i.e. as separate files for each individual molecule. Each portion of the file corresponding to a particular temperature-pressure pair begins with a header that contains information on the wavenumber (cm<sup>-1</sup>) range, number of cross-section data in this set, temperature (K), and pressure (torr). The maximum value of the absorption cross-section (cm<sup>2</sup>/molecule) and additional information containing the reference to that observation are also presented in each header. The wavenumber spacing of the cross-section listings is uniform for each of the pressure-temperature sets, and is determined by taking the difference between the maximum and minimum wavenumber and dividing by the number of points (cross-section data in this set).

The rest of the molecular cross-sections sets are taken from the 1996 HITRAN database, which, compared to 1992 HITRAN, provides an update for ClONO<sub>2</sub>. In addition to the ClONO<sub>2</sub> v<sub>4</sub> line parameters, new cross-sections for the ClONO<sub>2</sub> in the 1265-1325 cm<sup>-1</sup> region at 201, 211, and 222 K are available from 1996 HITRAN, as provided by Orphal *et al.* [1994].

The increased use of hydrofluorocarbons (HFCs), which are expected to replace CFCs and HCFCs in many applications in order to reduce the deleterious effects of released chlorine on the atmospheric ozone layer, will add another absorber in the IR 'window' region, 8-12 μm. Cross-sections data for a number of HCFCs have become available [Clerbaux *et al.*, 1993; Smith *et al.*, 1996]. More recently, Smith *et al.* [1998] determined the cross-sections of HFC-134

(CHF<sub>2</sub>CHF<sub>2</sub>) and HFC-143a (CF<sub>3</sub>CH<sub>3</sub>). All of these data are already available on the GEISA database [Jacquinet-Husson *et al.*, 1998] and will also be available on a future edition of HITRAN. At this time we prepared in TES format the cross-sections of HFC-134a (from Clerbaux *et al.*, 1993) which is considered as one of the most popular HCFC's.

### 3.3.8.3 Aerosols

The HITRAN 1996 compilation [Rothman *et al.*, 1998] contains auxiliary tables in ASCII for various atmospheric particles. The index of refraction tables include water and ice (the composition of cloud particles), aqueous sulfuric acid (the composition of volcanic aerosols), and nitrate acid trihydrate and aqueous HNO<sub>3</sub>/H<sub>2</sub>O (possible compositions of polar stratospheric clouds). The tables have individual wavenumber ranges, increments, and data formats. A description of the individual files is reported in Table 10 of Rothman *et al.* [1998]. Massie [1994] reviewed the indices of refraction which form the basis of the files on HITRAN 1996 [Rothman *et al.*, 1998]. Note that most of the available measurements were obtained only at room temperature.

The emission measurements obtained by TES will display enhanced radiances due to the scattering and absorption by aerosol particles. As is well known, sulfate aerosol injection into the stratosphere after a major volcanic eruption will greatly increase radiance levels. At such times, strong aerosol bands appear throughout infrared limb spectra [Rinsland *et al.*, 1994].

### 3.3.8.4 CKD 3.0 Continuum

A new continuum model is being developed for TES. This model includes continua due to water vapor, carbon dioxide, oxygen and nitrogen. The water vapor continuum [Clough *et al.*, 1980 and Clough *et al.*, 1989] and carbon dioxide continua are developed and utilized such that when the continuum contribution is added to the line by line component, agreement with observation is achieved. These continua have slow spectral dependence and known thermodynamic scaling. The continua for oxygen [Thibault *et al.*, 1996] and nitrogen [Lafferty *et al.*, 1996] are due to collision induced effects resulting from collisions with the respective molecule and the molecules comprising the air.

The water vapor continuum plays an important role in atmospheric radiative transfer providing increased opacity between spectral lines over the full spectral region from the microwave to the visible. The continuum is important to the physical solution of the inverse problem, the remote sensing of atmospheric state to retrieve temperature, water vapor, and trace species profiles as well as surface properties. There are two components to the continuum: the self-broadened continuum ( $C_s$ ), dependent on the square of the partial pressure of water vapor, and the foreign-broadened continuum ( $C_f$ ), dependent on the product of the water vapor partial pressure and the dry air pressure. As a consequence the self-broadened continuum tends to be more important in the lower atmosphere while the foreign-broadened continuum tends to be more important in the middle to upper troposphere. A comprehensive continuum model based on a single line shape for all transitions from the microwave to the visible has provided generally acceptable results [Clough *et al.*, 1989; hereafter CKD]. The general formulation for the absorption coefficient associated with the continuum is given by

$$\kappa_c = \nu \tanh(hc\nu / 2k_B T) \left[ (\rho_{H_2O} / \rho_0) \tilde{C}_s(T) + (\rho_{air} / \rho_0) \tilde{C}_f(T) \right] \quad (3.21)$$

with the usual definitions.

The CKD model has evolved with empirical adjustments over time to provide improved agreement with measurements (e.g. Clough, 1995). The current version of the model, CKD\_2.2, has been modified on the basis of two recent observations: (1) the measurement of the downwelling

radiance at Kavieng, New Guinea by Han *et al.* [1997] which indicated that the self-broadened continuum gave rise to an 8K error in brightness temperature at  $950\text{ cm}^{-1}$  for an atmosphere with  $\sim 6$  precipitable cm of water vapor; and (2) a clear indication that the foreign continuum was in error in the wings of the  $1600\text{ cm}^{-1}$  water vapor band as observed by Revercomb and colleagues at the U. of Wisconsin. These modifications are significant in the context of remote sensing from space. Of interest is the fact that the spectral character of the continuum in the  $950\text{ cm}^{-1}$  window has the effect of decoupling the atmospheric radiance of the moist atmosphere in the boundary layer from the surface emission, thereby significantly improving the accuracy with which boundary layer water vapor and surface brightness temperature can be retrieved (given the spectral emissivity of the surface). Examples of the role of the continuum for atmospheric observations may be found in Clough *et al.* [1992] and Mlawer *et al.* [1997].

As a result of more stringent accuracy requirements for remote sensing applications and with the availability of improved laboratory measurements and atmospheric observations, an entirely new water vapor continuum formulation is being developed [Mlawer *et al.*, 1999]. The basis for the new formulation is an important new set of laboratory measurements by Tobin *et al.*, 1996. The laboratory measurements are for 296K. The foreign continuum coefficient is taken as temperature independent consistent with the CKD model. The temperature dependence of the CKD model has been adopted for the self continuum. The new formulation involves not only line wing effects but also two types of collision-induced effects, one with high spectral content and the other with very slow spectral characteristics. The principal consequences for remote sensing are with respect to the foreign continuum, important in the upper troposphere for the retrieval of water vapor and for the background spectral radiance for retrieval of trace species including NO. An interim version of the new continuum is currently available and has been applied to atmospheric observations in the arctic by Tobin *et al.* [1999] with encouraging results. The agreement between observation and LBLRTM calculation with the new continuum in the  $400\text{-}500\text{ cm}^{-1}$  region in an extremely cold environment provides confidence that the model will perform well in the middle –upper troposphere in the  $1200\text{-}2000\text{ cm}^{-1}$  region of importance for TES retrievals. The new formulation has significantly higher spectral content than the CKD continuum model. It is anticipated that the self continuum coefficients will be stored on a  $0.5\text{ cm}^{-1}$  grid and the foreign continuum on a  $0.1\text{ cm}^{-1}$  grid.

## 3.4 JACOBIANS

The sensitivity of spectral radiance at the satellite to the perturbations of retrieved parameters included in the retrieval vector is the Jacobian matrix,  $\mathbf{K}$ . In general,  $\mathbf{K} = \partial \mathbf{F} / \partial \mathbf{x}$ , where  $\mathbf{F}$  is the forward model radiance and  $\mathbf{x}$  represent a retrieved parameter, such as temperature at level  $l$ .

### 3.4.1 Finite Difference

Evaluating Jacobian using finite difference method is straightforward. For example,  $\mathbf{K}$  can be calculated as  $[\mathbf{F}(\mathbf{x} + \Delta \mathbf{x}) - \mathbf{F}(\mathbf{x})] / \Delta \mathbf{x}$ , where  $\Delta \mathbf{x}$  is a small perturbation of parameter  $\mathbf{x}$ . If terms  $\mathbf{F}(\mathbf{x} + \Delta \mathbf{x})$  are calculated for all retrieved parameters by carrying out forward model many times, the algorithm is not very efficient considering that many layer quantities (see 3.3.1.3 and 3.3.1.4) will be unnecessarily calculated over and over again. The computation if not optimized can be expensive and the accuracy of the derivatives is more prone to numerical error and nonlinear contributions.

Based on the algorithms for TES forward model (3.3.1.4), the accelerated finite difference method to calculate Jacobian would be to calculate  $\mathbf{F}(\mathbf{x} + \Delta \mathbf{x})$  in the same computational loop through atmospheric layers while  $\mathbf{F}(\mathbf{x})$  is recursively calculated. At each layer, the necessary layer quantities required will be used to calculate both  $\mathbf{F}(\mathbf{x})$  and  $\mathbf{F}(\mathbf{x} + \Delta \mathbf{x})$ , such as absorption

coefficients, Planck functions, *etc.* The implementation of this accelerated method is relatively straightforward and it should provide a good standard to validate the analytical algorithms described below in both accuracy and computation speed.

### 3.4.2 Analytical

#### 3.4.2.1 Temperature and Gas Concentrations

Due to the form of the radiative transfer equation (equation 3.8), the analytic derivative of the radiance at the satellite with a change in parameter  $x_l$  at level  $l$ , is most expeditiously obtained in terms of associated layer quantities, so that we have

$$\frac{\partial L_{sat}}{\partial x_l} = \sum_j \frac{\partial L_{sat}}{\partial \bar{x}_j} \frac{\partial \bar{x}_j}{\partial x_l} \quad (3.22)$$

in which  $x_l$  is an element of the retrieval vector associated with level  $l$  and  $\bar{x}_j$  is the associated layer quantity for layer  $j$ . Note that in general,  $x$  may be mixing ratio (log mixing ratio) or temperature in this context.

In this section we focus on the computation of  $\frac{\partial L_{sat}}{\partial \bar{x}_j}$ , noting that  $\frac{\partial \bar{x}_j}{\partial x_l}$  is independent of wavenumber. Differentiating Eq. 3.8 with respect to  $\bar{x}_j$  we obtain

$$\begin{aligned} \frac{\partial L_{sat}}{\partial \bar{x}_j} &= \frac{\partial L^\uparrow}{\partial \bar{x}_j} + \varepsilon B(T_{sfc}) \frac{\partial T_{0,L}}{\partial \bar{x}_j} + \alpha \frac{\partial L_0^\downarrow}{\partial \bar{x}_j} T_{0,L} + \alpha L_0^\downarrow \frac{\partial T_{0,L}}{\partial \bar{x}_j} \\ &= \frac{\partial L^\uparrow}{\partial \bar{x}_j} + \alpha T_{0,L} \frac{\partial L_0^\downarrow}{\partial \bar{x}_j} + \left[ \varepsilon B(T_{sfc}) + \alpha L_0^\downarrow \right] \frac{\partial T_{0,L}}{\partial \bar{x}_j} \end{aligned} \quad (3.23)$$

The formula for the limb case is straightforward: the emissivity  $\varepsilon$  and the albedo  $\alpha$  are set to zero and unity respectively.

Appendix A3.4 gives the detailed derivations and discussions on each of the above terms. In summary, equations (A4.12), (A4.13) and (A4.15) in the appendix are used to evaluate the derivative of total transmittance with respect to layer species VMR, layer H<sub>2</sub>O VMR, and layer temperature,  $\frac{\partial T_{0,L}}{\partial \bar{x}_j}$ , respectively. Equations (A4.22) and (A4.25) together with part of (A4.12), (A4.13), and (A4.15) are used to calculate the derivative of upwelling radiance with respect to the layer quantities,  $\frac{\partial L^\uparrow}{\partial \bar{x}_j}$ . Similar algorithms apply to the term  $\frac{\partial L^\downarrow}{\partial \bar{x}_j}$ .

The important strategy is that in calculating the total transmittance,  $T_{l,L}$  from TOA to a given layer the calculation starts from TOA. If at some level  $L_{min}$  that  $T_{L_{min},L}$  becomes less than a small

threshold value, the contributions of downwelling and surface terms as well as the upwelling portion below this level may be ignored.

### 3.4.2.2 Surface Properties

The possible retrieved parameters for the surface are the surface temperature  $T_{sfc}$ , emissivity  $\epsilon(v)$  and albedo  $\alpha(v)$ . The Jacobians for these parameters are calculated analytically. Derivations are straightforward given that the surface contribution to the total radiance is a separate term in the radiative transfer equation 3.8. Emissivity and albedo functions can be expressed as either polynomial functions of frequency or tabulated on a coarse spectral grid (no finer than  $10 \text{ cm}^{-1}$  spacing). For tabulated  $\epsilon(v)$  on a frequency grid with any two adjacent table points at  $v_a$  and  $v_b$ , the emissivity at  $v$ , where  $v_a \leq v \leq v_b$ , is given by:

$$\epsilon(v) = \left[ \frac{v_b - v}{v_b - v_a} \right] \epsilon_a + \left[ \frac{v - v_a}{v_b - v_a} \right] \epsilon_b \quad (3.24)$$

Assuming the albedo is defined on the same grid, we have the following surface Jacobians:

$$\frac{\partial L_{sat}}{\partial T_{sfc}} = \epsilon(v) \frac{\partial B}{\partial T_{sfc}} T_{0,L} \quad (3.25)$$

$$\frac{\partial L_{sat}}{\partial \epsilon_a} = \left[ \frac{v_b - v}{v_b - v_a} \right] B(T_{sfc}) T_{0,L} \quad (3.26)$$

$$\frac{\partial L_{sat}}{\partial \alpha_a} = \left[ \frac{v_b - v}{v_b - v_a} \right] L_0^\downarrow T_{0,L} \quad (3.27)$$

$$\frac{\partial L_{sat}}{\partial \epsilon_b} = \left[ \frac{v - v_a}{v_b - v_a} \right] B(T_{sfc}) T_{0,L} \quad (3.28)$$

$$\frac{\partial L_{sat}}{\partial \alpha_b} = \left[ \frac{v - v_a}{v_b - v_a} \right] L_0^\downarrow T_{0,L} \quad (3.29)$$

### 3.4.2.3 Limb Background Parameters

Using Equation 3.8 for the limb case, we have  $L_{sat} = L_L^\uparrow$ . In order to adjust for any background radiance as described in 3.5.2.1, we can assume  $L_{sat} = [a(v - v_{min}) / (v_{max} - v_{min}) + b] + L_L^\uparrow$  where  $a$  and  $b$  are arbitrary slope and offset radiances and  $v_{min}$  and  $v_{max}$  are the endpoints of the microwindow under consideration. The Jacobians for  $a$  and  $b$  are calculated analytically from the above expression.

### 3.4.2.4 Pointing

In the limb case, retrieving instrument pointing angle needs to be carried out as part of the profile retrievals. Recall that the TES forward model radiances for the rays along the field of view directions starting from pre-defined tangent pressure levels are interpolated in zenith angle and convolved with the instrument field of view function (section 3.3.6). Only one angle, the instrument pointing angle (e. g. the zenith angle for the optical axis) determines the relative “alignment” between the pixel dependent FOV functions and the radiance rays. The derivative of pixel radiance with respect to this angle can be calculated by perturbing this angle, equivalently shifting the FOV function relative to the forward model rays by a delta angle, and performing the convolution again. The difference of the perturbed and the reference convolved radiances divided by the delta angle gives the pointing angle Jacobian.

## 3.5 RETRIEVAL

### 3.5.1 General Strategy

Our goal is to have a single, flexible, efficient retrieval code that can be used in a variety of ways under control of a driver table. The approach is to use non-linear least squares spectral fitting, based on the so-called optimal estimation technique [Rodgers, 1970].

For a particular observation set, the retrieval will be run a number of times for different parameters. The runs will mostly be sequential, with retrieved quantities from one stage feeding the next as fixed inputs. Computational gains from parallelization can be achieved by processing multiple observation sets at the same time.

Each retrieval will be supplied with an initial full state vector, along with other information needed, including an initial guess and possible *a priori* information. The initial guess may be derived from a preliminary, simplified retrieval (see section 3.5.4.2). The availability of temperature and moisture fields from NWP models is also expected to be very useful in this context.

As an example of an initial retrieval strategy the following approach will be evaluated. The limb and nadir spectra will be treated independently. This is the simplest approach, and allows partial results from incomplete observation sets. The first step in the limb case will be the simultaneous retrieval of the pointing angle and the temperature field in the spatial regime associated with the pixel just below the tropopause. This retrieval will be followed by the retrieval of the full temperature profile, which will likely be used as the initial guess for the nadir temperature retrieval. In the nadir case, the temperature and water profiles will be retrieved first. Next, the N<sub>2</sub>O profile (limb) or column (nadir) will be retrieved to verify cloud free conditions. Individual (or combined) species retrievals will follow. Because the nadir ozone retrieval will use a relatively broad spectral region, it will probably be done last. Also, because of the stratospheric overburden, the limb ozone profile could be used for the initial guess for the nadir retrieval.

A detailed retrieval strategy requires further study, and will be modified in the light of experience with real data. The retrieval strategy will be implemented by defining the sequence of stages, with their inputs and outputs. These definitions will form a driver table that will be used to control the retrieval process. A stage will be defined by the following parameters:

- quantities to be placed in the retrieval vector
- source of first guess for each of these quantities
- source of *a priori* for each of these quantities
- quantities to be used as forward model parameters

- source of the forward model parameters
- numerical method to be used to minimize the cost function
- subset of the measured spectrum to be used
- other items TBD.

Finally, the complete spectrum will be calculated for quality control. In the limb case, the final calculation will be done for each pixel. In the nadir case, this will actually be a retrieval of surface emissivity using the already determined atmospheric state.

### 3.5.2 Retrieval Vectors

The retrieval vector is the subset of the full state vector that is a target for retrieval. Each retrieval stage will have its own retrieval vector. To simulate a measurement given a retrieval vector, it is first expanded to form the full state vector by interpolating the profiled quantities from the retrieval grid to the full grid and adding the relevant forward model parameters.

The retrieval code will be written so that joint retrievals are possible, with the quantities being retrieved at each stage being specified by the driver table. The retrieval vector may be selected from the following, although not all combinations will be valid.

- surface emitting temperature, for each detector
- surface spectral emissivity for a specified spectral range, for each detector
- atmospheric temperature on a contiguous range of levels of the retrieval grid
- constituent mixing ratio ( $q$ ) on a contiguous range of levels of the retrieval grid
- constituent  $\ln(q)$  on a contiguous range of levels of the retrieval grid
- aerosol extinction coefficient (or its  $\ln$ ) on a contiguous range of levels of the retrieval grid and for a specified spectral range
- limb background parameters for each detector
- the angle of the boresight of the spectrometer

Each retrieved profile quantity will have its own altitude range of retrieval grid elements. The quantities not being retrieved at each stage will be treated as forward model parameters.

The interpolation of profiled quantities from the retrieval grid to the full grid will be carried out as follows:

- (1) Temperature is linearly interpolated in  $\log(P)$
- (2) Logarithms of constituent mixing ratios and aerosol extinction coefficients are interpolated linearly in  $\log(P)$

Temperature is interpolated linearly in  $\log(P)$  because that is how temperature usually behaves in the atmosphere, and because it simplifies the integration of the hydrostatic equation. The same may be said of  $\log$  mixing ratio as most constituent distributions show a smoother behavior when plotted as  $\log(q)$  rather than  $q$ , e.g. Figure 3 - 6.

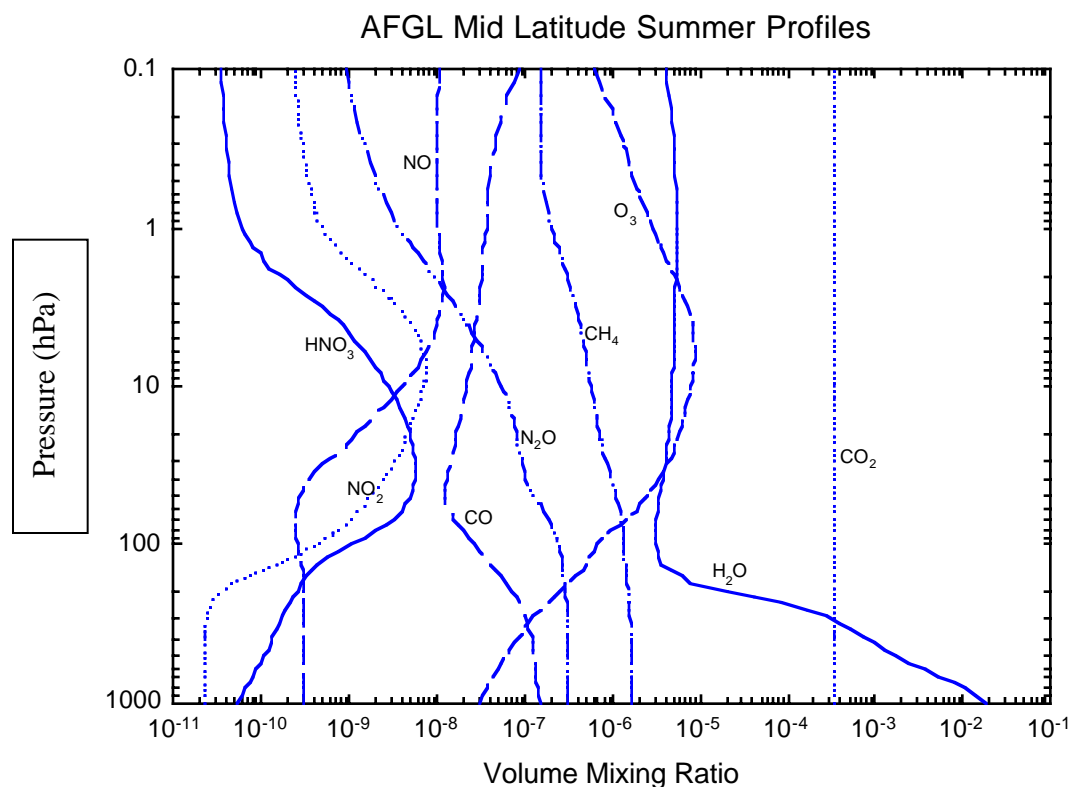
#### 3.5.2.1 Limb Background Parameters

In the limb mode, we will retrieve offset and slope parameters, for each detector, to account for any smooth radiance residuals in our limb microwindows. These parameters are applied in the forward model at the conclusion of the radiative transfer calculation, in a manner similar to the nadir surface parameters. Smooth residuals in the limb microwindows could be due to unmodeled aerosols and/or errors in the continuum model, cross-sections of heavy molecules and radiometric calibration. The retrieved parameters will be examined as a diagnostic of the possible aerosol or error contributions to the radiance. For example, if a calibration error is present, these retrieved



parameters should be approximately the same for all detectors, while if residual radiances are due to aerosol emission, we should observe variations with detector tangent height.

Figure 3 - 6: AFGL Mid Latitude Summer Profiles



### 3.5.3 A Priori Constraints

*A priori* is a description of what is known or believed about the state before the measurement is considered. Typically it may comprise a climatological estimate of the state plus some measure of its uncertainty, most conveniently expressed as a covariance matrix. Other possible sources include independent measurements by other observing systems, such as the NCEP analyses or forecasts.

Other constraints that may be used include *ad hoc* smoothness, positivity, and linear inequality constraints. Smoothness can be imposed by adding a quadratic form to the cost function that penalizes the second difference of the profile [Twomey 1963]. Positivity for constituents may be imposed by using  $\log(\text{mixing ratio})$  rather than mixing ratio in the state vector. Linear inequality constraints allow physical bounds to be imposed on the range of the state vector elements, such as emissivity [Gill, Murray, and Wright, 1981].

The combination of constraints to be used will be determined by the driver table (see 3.5.1).

#### 3.5.3.1 Surface Radiative Properties

For the retrieval of surface temperature, emissivity and reflectance, TES has the advantage that it will be viewing identical locations every 16 days in the Global Survey mode. This will allow us to develop a surface property database that is tailored to the observations used to produce our standard products. In order to build up this database and to retrieve the surface properties for our special products, we will have the capability of retrieving surface emissivity and reflectance

parameters for all the TES spectral ranges where surface information can be obtained. Since we plan to use microwindows to retrieve atmospheric parameters, we will need to perform a final retrieval of the surface properties for scenes over land using the forward model generated for the entire measured spectrum after all atmospheric parameters are computed. This must be done in order to produce meaningful residuals that can be used for diagnostics or research, but will also produce useful surface emissivity and reflectance spectra.

As described in section 3.3.2.1, the surface model allows us to retrieve a single surface “skin” temperature parameter and emissivities/reflectances that are specified on a coarse grid as either fixed or retrieved parameters. For TES nadir data taken over water, we would fix the emissivity parameters to the known water emissivity spectrum and retrieve only the “skin” temperature. This may also be possible for some well-characterized scenes over ice. For land targets, the emissivity spectrum will be retrieved using reasonable first guess emissivity values (described in section 3.3.2.1). We have successfully performed land emissivity retrievals with silicate features using AES data and we found that emissivity parameters need additional constraints so that they are limited to physical values (*i.e.*, they must be less than 1).

### 3.5.3.2 Reference Pressure

The reference pressure either at sea level or at surface and the surface elevation are two important parameters in TES forward model simulations. The accuracy of this pair of parameters will affect the accuracy of the retrieval products. The sources of reference pressure would be the re-analysis product from metrology centers, such as ECMWF, NCEP, and DAO, where the historical meteorological observations are consistently analyzed using atmospheric models to produce the best knowledge of the atmospheric states. We need to identify and evaluate the available reference pressure data sources.

### 3.5.4 Inverse Algorithm

The inverse algorithm for a particular retrieval vector  $\mathbf{x}$  will follow the general approach outlined in Rodgers (1976). The cost function  $C(\mathbf{x})$  will be the quadratic form:

$$C(\mathbf{x}) = (\mathbf{x} - \mathbf{x}_a)^T \mathbf{S}_a^{-1} (\mathbf{x} - \mathbf{x}_a) + (\mathbf{y} - \mathbf{F}(\mathbf{x}))^T \mathbf{S}_e^{-1} (\mathbf{y} - \mathbf{F}(\mathbf{x})) \quad (3.30)$$

Minimization proceeds iteratively from an initial guess by means of an appropriate numerical method, until convergence is obtained. It is clearly important that each of these stages is carried out efficiently and accurately.

#### 3.5.4.1 Initial Guess

The main sources for the initial guess are the *a priori* and a nearby retrieval. The nearest previous retrievals include the previous one along the orbit (about 530 km), one at the same latitude on an adjacent orbit (orbital spacing is about 24°), or one at the same latitude on the previous day. It is of course possible that any of these was not retrieved due to cloudy pixels. The available information may be combined by weighting each according to its estimated precision. The initial guess based on one or more of these pieces of information will then be refined using a simpler, faster and less accurate retrieval than the full resolution non-linear iteration.

#### 3.5.4.2 Initial Guess Refinement

The purpose of initial guess refinement is to start the relatively expensive optimal estimator close to the final solution, so that as few iterations as possible are required. Thus a computationally

inexpensive *ad hoc* non-optimal retrieval method is used to find the region of the solution. Attention is concentrated on the more non-linear aspects of the problem.

#### 3.5.4.2.1 Nadir

In the nadir case, a preliminary retrieval step could be to treat the troposphere and stratosphere as two columns. This step is to fit the measurement spectrum to solve for the two scale factors that would shift the initial guess constituent profile, and this refined profile would then be the initial guess profile used for the full optimal retrieval at more levels.

#### 3.5.4.2.2 Limb

In the limb case, the onion peeling method can be used to obtain an initial guess profile for the full optimal retrieval. The onion peeling procedure starts from the top pixel. By fitting the spectra of measurement and the forward model for a given pixel, the constituent mixing ratio at the tangent layer is solved. Since only one parameter is calculated at one step, this procedure is relatively inexpensive and stable.

#### 3.5.4.2.3 Strategy for Limb Pointing Retrieval

The central problem to be addressed from the spacecraft is the pointing direction of the 2B1 reference focal plane. Once this is known, then the pointing of all pixel elements is established given predetermined focal plane properties. The general strategy will be to utilize the radiance spectrum associated with a pixel having a projection in the upper troposphere to minimize the effects of clouds and to perform a simultaneous retrieval of pointing angle and temperature.

The procedure for establishing the radiance field at the satellite and the relevant Jacobians with respect to pointing angle and to temperature is described elsewhere. The initial guess for the pointing angle will be obtained from the encoder associated with the platform spacecraft attitude system. For this stage of the pointing angle retrieval, there will be three elements for the retrieval state vector: (1) the pointing angle, (2) a shift in level temperature for all tangent rays included in the FOV, and (3) a shift in temperature lapse rate for all tangent rays included in the FOV. It will probably be necessary to retrieve temperature profiles somewhat above the tangent layers, but this can be handled in a fashion analogous to the line of sight retrievals appropriate to the nadir case. The spectral region will be that associated with carbon dioxide for which the mixing ratio is assumed known, Figure 3 - 6, and one in which water vapor plays a minimal role.

The radiance at the satellite is calculated for each tangent ray required for the FOV convolution. The tangent levels associated with all tangent rays are those of the forward model pressure grid. The zenith angle of the tangent ray at the satellite,  $\theta$ , is obtained directly from Snell's law,

$$n R \sin(\theta) = \text{Constant} \quad (3.31)$$

$$n_t (R_c + z_t) = R_{cs} \sin(\theta_s) \quad (3.32)$$

$$\theta_s = \text{asin} \{ n_t (R_c + z_t) / R_{cs} \} \quad (3.33)$$

where  $z_t$  is the tangent altitude,  $R_c$  is the radius of curvature of the geoid,  $R_{cs}$  is the distance from the satellite to the center of curvature and  $n_t$  is the index of refraction. The altitude  $z_t$ , required for this calculation is obtained from the hydrostatic equation. As in the nadir case, *a priori* information is required to obtain the altitudes at the required tangent pressure levels to required accuracy, e.g. the surface pressure and the temperature field from the surface to the tangent pressure. The angle

between  $R_c$  and  $R_{cs}$  is given by  $\psi$ . The radius of curvature for a TES limb observation is defined for the tangent ray associated with  $z=0$ . The change in curvature over the tangent ray altitudes may be neglected for these purposes. The nominal radius of the Earth is taken as 6378 km with the satellite at 700 km. The atmosphere is the tropical atmosphere [Anderson *et al.*, 1986].

The dependence of the radiance field on the zenith angle at the satellite,  $\theta_s$ , is nonlinear and is retrieved as an element of the retrieval vector in the nonlinear retrieval procedure. The Jacobian required is obtained analytically in the course of the FOV convolution. Results from a simultaneous pointing angle / temperature retrieval are provided in Table 3 - 2. The method, as evaluated through simulations, has been established to be robust and provides excellent accuracy.

Relevant geometrical quantities and horizontal offsets in the direction of the satellite are provided in Table 3 - 3 as a function of tangent height. These offset values enable the evaluation of the effects of using a single column for the hydrostatic equation. It may be noted that the FOV is 25 km wide in the horizontal direction perpendicular to the chief ray. The effect on the pointing / temperature retrieval due to an error in the tangent altitude obtained from the hydrostatic equation is small.

This simultaneous retrieval approach should be more critically evaluated with respect to measurement errors greater than those given by the source radiance and with respect to the expected sources of systematic error. The use of pixels in other atmospheric regimes such as the lower stratosphere needs to be explored since there would presumably be less cloud. Also to be explored is the inclusion of the pointing angle in the retrieval state vector for the global fit associated with the retrieval of the temperature field. The relative registration of the four focal plane arrays is determined by the on-board spatial calibration. It may also be tested in space by viewing sharp radiative discontinuities in the scene with both nadir and limb views. These discontinuities can be associated with discontinuities in cloud fields for both the limb and nadir mode and in surface properties (land/ocean) for the nadir view. The relative registration of the pixels is independent of the viewing mode so that there should be consistency between pixel registrations obtained from the two modes. Also to be explored is the retrieval of pointing angle using other spectral regions associated with the other focal planes to further evaluate the consistency of pointing angle among the focal plane arrays.

**Table 3 - 2: Retrieval results for temperature and tangent point for central ray of pixel 11 with TES FOV (tangent height = 11.5 km).**

Case	Parameter		Perturbation	Retrieved	Difference	Error (1 $\sigma$ )
1c	Temperature	(K)	1.0	1.00	0.00	0.02
(700-800 cm-1)	Tangent Point	(m)	500.0	501.00	1.00	1.96
1d (NESR*10)	Temperature	(K)	1.0	0.97	0.03	0.20
(700-800 cm-1)	Tangent Point	(m)	500.0	506.40	6.40	19.60

**Table 3 - 3: Quantities related to the ray trace from the tangent point to the satellite as a function of tangent height. Refraction is included in the ray trace.**

Tangent Height	$\theta_s$	$\sin(\theta_s)$	$\Psi$	bending	Horizontal Offset
(km)	(deg)		(deg)	(deg)	(km)
37.95	115.078	0.90574	17.137	0.003	-163.9
36.80	115.099	0.90557	17.086	0.003	-150.3
35.65	115.121	0.90541	17.035	0.004	-142.3
34.50	115.143	0.90525	16.985	0.005	-134.3
33.35	115.165	0.90509	16.936	0.006	-126.4
32.20	115.187	0.90492	16.887	0.007	-118.6
31.05	115.209	0.90476	16.839	0.008	-110.8
29.90	115.231	0.90460	16.791	0.010	-103.0
28.75	115.252	0.90444	16.744	0.012	-95.3
27.60	115.274	0.90428	16.698	0.014	-87.5
26.45	115.296	0.90412	16.652	0.017	-79.9
25.30	115.317	0.90395	16.606	0.021	-72.2
24.15	115.339	0.90379	16.562	0.025	-64.5
23.00	115.360	0.90363	16.518	0.030	-56.8
21.85	115.382	0.90347	16.474	0.036	-49.0
20.70	115.403	0.90331	16.431	0.043	-41.2
19.55	115.424	0.90315	16.388	0.052	-33.2
18.40	115.445	0.90300	16.347	0.063	-25.2
17.25	115.466	0.90284	16.305	0.077	-17.0
16.10	115.487	0.90268	16.265	0.091	-8.7
14.95	115.508	0.90253	16.225	0.110	0.0
13.80	115.528	0.90237	16.186	0.133	9.0
12.65	115.549	0.90222	16.147	0.150	17.3
11.50	115.569	0.90207	16.109	0.167	25.3
10.35	115.589	0.90191	16.071	0.187	33.8
9.20	115.609	0.90176	16.034	0.211	42.7
8.05	115.629	0.90161	15.998	0.237	51.6
6.90	115.649	0.90146	15.962	0.266	60.8
5.75	115.668	0.90132	15.927	0.299	70.3
4.60	115.687	0.90117	15.893	0.334	80.0
3.45	115.707	0.90103	15.859	0.372	89.9
2.30	115.725	0.90089	15.826	0.416	100.4
1.15	115.744	0.90075	15.793	0.470	111.8
0.09	115.760	0.90062	15.764	0.523	122.6

### 3.5.4.3 Numerical Solution

There is a wide range of numerical methods available in the literature designed for minimizing non-linear least-squares functions which are basically quadratic forms. The basic methods considered

here are the Gauss-Newton method and the Levenberg-Marquardt method. Both methods require a Jacobian to be calculated.

For the cost function in equation (3.30), the Gauss-Newton iteration is described by

$$\mathbf{x}_{i+1} = \mathbf{x}_i + (\mathbf{S}_a^{-1} + \mathbf{K}_i^T \mathbf{S}_e^{-1} \mathbf{K}_i)^{-1} (\mathbf{K}_i^T \mathbf{S}_e^{-1} [\mathbf{y} - \mathbf{F}(\mathbf{x}_i)] - \mathbf{S}_a^{-1} [\mathbf{x}_i - \mathbf{x}_a]) \quad (3.34)$$

where  $\mathbf{K}_i = \partial \mathbf{F}(\mathbf{x}_i) / \partial \mathbf{x}$  is the Jacobian. Equation (3.28) can also be written as

$$\mathbf{x}_{i+1} = \mathbf{x}_a + (\mathbf{S}_a^{-1} + \mathbf{K}_i^T \mathbf{S}_e^{-1} \mathbf{K}_i)^{-1} \mathbf{K}_i^T \mathbf{S}_e^{-1} [\mathbf{y} - \mathbf{F}(\mathbf{x}_i) - \mathbf{K}_i(\mathbf{x}_i - \mathbf{x}_a)]. \quad (3.35)$$

Note that the efficiency of the iteration is enhanced if  $\mathbf{S}_e$  is diagonal, particularly for cases where the measurement vector is large, as in the case of TES. However, the apodization of microwindows will introduce off-diagonal elements in  $\mathbf{S}_e$  and other sources such as calibration may also cause correlations in the measurement errors. The off-diagonal elements due to apodization are easily calculated and if any other correlations are stable with time, we could perform an inversion of the error correlation matrix on an infrequent basis. This stored matrix could then be scaled using the diagonal measurement errors to provide  $\mathbf{S}_e^{-1}$  for each retrieval. The retrieval sensitivity to the accuracy of the off-diagonal elements in  $\mathbf{S}_e$  needs to be studied in order to decide when off-diagonal elements can be neglected and how often the inverted correlation matrix would need to be updated to account for any time variations.

The Gauss-Newton method is satisfactory for *small residual problems* [Fletcher, 1993]. For these problems, the initial guess is in a region sufficiently close to the solution such that non-linearities in the cost function are small, as we hope to have with the initial guess refinement. If the initial guess refinement is not successful, then the Levenberg-Marquardt (LM) method will be used. This algorithm is implemented as a *trust-region* method [More', 1977]. In this method, the cost function in (3.30) is minimized subject to a constraint on the maximum step size,  $\|\mathbf{x}_{i+1} - \mathbf{x}_i\| < \delta$ . The *trust region radius*  $\delta$  defines a sphere over which the cost function is considered linear. The iteration becomes

$$\mathbf{x}_{i+1} = \mathbf{x}_i + (\gamma_i \mathbf{W}^T \mathbf{W} + \mathbf{S}_a^{-1} + \mathbf{K}_i^T \mathbf{S}_e^{-1} \mathbf{K}_i)^{-1} (\mathbf{K}_i^T \mathbf{S}_e^{-1} [\mathbf{y} - \mathbf{F}(\mathbf{x}_i)] - \mathbf{S}_a^{-1} [\mathbf{x}_i - \mathbf{x}_a]) \quad (3.36)$$

where the parameter  $\gamma_i$  is called the LM parameter and  $\mathbf{W}$  is a non-zero scaling matrix that permits the minimization over an ellipse rather than a sphere. The LM parameter is varied from step to step according to the strategy described by More':

1. Find  $\gamma_i$  such that the step size is within the trust region radius.
2. Check that  $C(\mathbf{x}_{i+1}) < C(\mathbf{x}_i)$ . If the update cost function has increased, then reduce the trust region radius and return to step 1.
3. Compare  $C(\mathbf{x}_{i+1})$  with its linear approximation,  $C_1(\mathbf{x}_{i+1})$ .
4. Increase the trust region radius if  $C(\mathbf{x}_{i+1}) \sim C_1(\mathbf{x}_{i+1})$  and decrease if  $C(\mathbf{x}_{i+1}) \gg C_1(\mathbf{x}_{i+1})$ .
5. Return to step 1 for next iteration.

#### 3.5.4.4 Convergence Criterion

The convergence criterion depends on the numerical method being used. If it is a second-order method such as Levenberg-Marquardt then once the  $\gamma$  parameter has become small, i.e., when the Levenberg-Marquardt step reduces to a Gauss-Newton step, a change  $C(\mathbf{x}_i) - C(\mathbf{x}_{i+1})$  that is

positive and much less than unity is appropriate [Press *et al.*, 1989]. When convergence appears to have taken place according to this criterion the absolute value of  $C(\mathbf{x})$  will be examined to determine whether the iteration has converged to a valid solution. This is determined using a  $\chi^2$  test:

$$\chi^2 = (\mathbf{y} - \mathbf{F}(\mathbf{x}))^T \mathbf{S}_e^{-1} (\mathbf{y} - \mathbf{F}(\mathbf{x})). \quad (3.37)$$

This test determines whether the solution agrees with the measurements to the required accuracy. We may also test whether the solution agrees with the *a priori* using

$$\chi^2 = (\mathbf{x} - \mathbf{x}_a)^T \mathbf{S}_a^{-1} (\mathbf{x} - \mathbf{x}_a) \quad (3.38)$$

but the statistics of the *a priori* are likely to be less well known than those of the measurement error, so this may tell us more about the quality of the *a priori* rather than that of the retrieval.

#### 3.5.4.5 Jacobian Update

In principle the Jacobian should be recalculated every iteration. At the time of writing it is not known how expensive that will be, although if it is carried out using an algebraic derivative built into the forward model it will not be computationally expensive.

If that is not possible, and the Jacobian must be calculated by perturbation, then it will be expensive, and a strategy for minimizing the number of evaluations will be required. The following sample strategies require testing:

- (1) Iterate to convergence. Calculate a new Jacobian at convergence.
- (2) Recalculate the Jacobian every  $n$ th iteration, for some TBD  $n$ .
- (3) Examine the change of  $C(\mathbf{x}_i)$  as a function of  $i$ . If it is not decreasing quadratically, recalculate the Jacobian.

### 3.5.5 Clear Pixel Identification (nadir)

At this time, we do not have a forward model that would allow us to retrieve cloud altitudes or their optical properties. Therefore, we must at least be able to identify the presence of clouds so that incorrect retrievals are not propagated. For TES nadir data, we should be able to reject most of the cloud filled or partially filled pixels by the cloud flags provided by Level 1B. These flags will be calculated based on radiance levels and differences using methods similar to those proposed for MODIS [Ackerman, *et al.*, 1998]. In addition, we have demonstrated using AES data that inter-pixel radiance differences provide a good indication of either partial cloud filling or large surface variations for nadir views. These types of scenes would require special processing and should be flagged as such. We plan to choose our initial Level 1B threshold levels based on studies of AES nadir data as well as nadir and limb simulations with clouds for different seasons and latitudes. For nadir scenes that are not rejected, either because of small partial cloud filling or thin cirrus, we should be able to detect clouds, or at least determine the errors associated with non-detection, by testing the sensitivity of retrieved parameters, such as the  $\text{N}_2\text{O}$  column, to different cloud optical depths, altitudes and pixel fill ratios.

Another possibility, to be considered for special processing, is to perform the retrieval in the presence of clouds using the  $\text{CO}_2$  slicing technique, in conjunction with the NWP temperature field, to determine the effective cloud amount and the cloud-top pressure. The cloud could then be included in the forward model with retrievable optical parameters. The basic  $\text{CO}_2$  slicing method is described in many papers (see the description and references in Wylie, *et al.*, 1994) and involves the assumption of a single cloud layer. The cloud-top pressure is determined using the measured



radiance and the estimated clear sky radiance for (at least 2) channels with CO<sub>2</sub> lines where the weighting functions peak at different altitudes. This type of algorithm can be tested with many existing data sets such as AES, IRIS-D, IMG and NAST-I. For TES data, in many cases, we should be able to compare the estimated cloud top pressures with CHEM OMI data products.

### **3.5.6 Clear Pixel Identification (limb)**

Clear pixel detection in the limb view is much more straightforward than in the nadir because the background is cold space rather than a warm surface. It can be accomplished simply by setting a radiance threshold in a window region such as 12  $\mu\text{m}$ . Calculations made for ISAMS [Lambert *et al.*, 1996] show limb radiance at 12  $\mu\text{m}$  in the region of 10-20 km as around 0.5 mW/m<sup>2</sup>/sr/cm<sup>-1</sup> in the absence of aerosol, compared with the Planck function at 200K of around 20 mW/m<sup>2</sup>/sr/cm<sup>-1</sup>. Mt. Pinatubo volcanic aerosol was shown to be optically thick in this region, so that we would expect cirrus cloud also to be optically thick.

A more sophisticated cloud detector would be the joint retrieval of temperature and aerosol extinction profiles using an onion peeling process. The lower limit of the limb retrieval would then be set as the lowest altitude where the aerosol extinction is less than some threshold.

### **3.5.7 Retrieval Microwindow Selection**

There are several reasons for using small regions of the spectrum (microwindows) for retrievals, including:

- Reduction in computation, because the forward model only has to generate a small interval.
- Reduction in computation due to fewer fitted parameters
- Reduction of the effect of interfering gases

The spectral size of the microwindows will range from a few wavenumbers to one hundred or more wavenumbers, depending upon the species to be retrieved. In order to achieve the maximum reduction in computing time, both the calculated and observed spectrum need to be apodized. This reduces the ringing of lines, and thus the width of the spectrum required.

Usually, different microwindows will be needed for different altitude regions, and for the nadir and limb. Generally, strong lines will be used for high altitudes, while weak lines will give more information at low altitudes.

There are at least two objective methods for microwindow selection [Rodgers 1996, von Clarmann 1999]. Candidate regions are selected for a species based on known absorption and interferences. The information content for particular points in the interval are evaluated, and selections made to maximize the information. Initial microwindows will be selected using simulated spectra, with expected instrument noise. The microwindows will be revised early in the mission based on real instrument performance.

### **3.5.8 A Priori Database Generation**

We are in the process of assembling climatologies for all of our retrieved species. The primary purpose of collecting these data is to formulate *a priori* covariance matrices,  $\mathbf{S}_a$ , appropriate for different observing conditions. However, they may also be used to generate the retrieval first guess in some cases and for simulating test data. At present we have profile information for most IR active trace gases in the stratosphere and upper troposphere from UARS and ATMOS. However,

information in the troposphere is more difficult to acquire since there are relatively few measurements available. As a starting point, we have converted temperature, water vapor and ozone profiles from the TIGR (TOVS initial guess retrieval) database [Heinemann, *et al.*, 1995] to TES Level 2 input specifications. These data are from ozone sondes and contain 40 pressure levels, from sea level to 0.05 mb. A recent analysis of ozone sonde data for seasonal, latitudinal and longitudinal dependence, with particular attention to errors and biases, has been released by J. Logan [Logan, 1998]. This compilation will form the basis for the ozone climatology that we use to generate *a priori* correlations. We plan to incorporate other EOS, IMG and ENVISAT data as they become available, especially if they are assembled into climatologies for general use.

### 3.5.9 Error Analysis

The retrieved state  $\mathbf{x}_r$  can be related to the true state  $\mathbf{x}$  by

$$\mathbf{x}_r = \mathbf{x}_a + \mathbf{A}(\mathbf{x} - \mathbf{x}_a) + \mathbf{e}_x \quad (3.39)$$

where  $\mathbf{A} = \partial \mathbf{x}_r / \partial \mathbf{x}$  is the averaging kernel, and  $\mathbf{e}_x$  is the contribution to the total error from random and systematic errors in the measurement and the forward model.

The error term  $\mathbf{e}_x$  can be described by a covariance matrix  $\mathbf{S}_e$ , which can be expressed as the sum of random and systematic components:

$$\mathbf{S}_e = \mathbf{S}_r + \mathbf{S}_s \quad (3.40)$$

The averaging kernel matrix and the error covariances may be calculated at little cost during the retrieval process. However they are of size  $n^2$ , when  $\mathbf{x}$  is of size  $n$ , and every retrieval has its own unique averaging kernel and error covariance. There may be problems of (a) storage and (b) user appreciation.

The following parameters will be computed for error characterization:

- (1) the error variance of each retrieved quantity, separated into random and systematic components.
- (2) for profile quantities, the ‘correlation distance’, or vertical range outside which the absolute value of correlation coefficient is less than some TBD quantity (nominally 0.5)
- (3) the correlation matrix for the retrieval vector
- (4) the fraction of explained variance

The averaging kernel matrix should be made available in some form, but it is TBD whether we present (1) the full matrix for every retrieval or (2) a few sample matrices

The fraction of explained variance can be described as

$$f_i = 1 - [\mathbf{K}^T \mathbf{S}_e^{-1} \mathbf{K} + \mathbf{S}_a^{-1}]^{-1}_{ii} \mathbf{S}_{a ii} \quad (3.41)$$

which has the property that  $f_i$  takes the value 1 when all of the information comes from the data and none from the *a priori* and 0 when no information comes from the data.

Finally, the user should know the range of grid levels over which the retrieval comes primarily from the data, rather than the *a priori*. This is most properly expressed in terms of the area of the averaging kernel, a vector of length  $n$ . It can be simplified to two numbers - the upper and lower levels of the range within which the *a priori* contribution is less than some given fraction.

### 3.6 FINAL FULL SPECTRUM CALCULATION

In order to search for unmodeled species in our data, we will examine the difference between the complete forward model generated from our retrieved atmospheric state and the full TES measured spectrum. The final forward model is calculated using the full state vector constructed from the microwindow retrievals. Unmodeled species will appear as deviations in the residual that are above the noise level and have characteristic spectral features that can be analyzed using techniques such as Fourier analysis, wavelet transforms or spectral matched filtering.

For land nadir views, in order to calculate a residual spectrum, we will also need to retrieve surface spectral emissivity parameters since these cannot be completely provided from the microwindow retrievals. This requires saving the transmission and downwelling radiance from the atmospheric radiative transfer calculation but the Jacobians of the atmospheric parameters would not need to be calculated or stored.

### 3.7 DATA QUALITY & RESIDUALS

Data quality will be indicated in several ways. The first level will be indicated by flags generated by various processing steps. If level 1B flags are all acceptable, the level 2 processing will start. If level 2 retrieval fails, additional flags will be used to indicate the cause (these will be recorded in the level 2 processing log).

At the end of each retrieval stage, the following flags will be generated (some may be numerical quantities):

- non-convergence
- out of expected range
- consistency between nadir and limb retrieval (if appropriate)
- average spectral residuals larger than expected
- maximum spectral residuals larger than expected

For the final complete spectrum calculation, only the latter two flags will be used.

Subsequent retrieval stages will check the relevant flags from earlier stages before proceeding, for example a failed temperature retrieval will halt processing, while failure to retrieve CO would not halt ozone retrieval.

Observation sets that complete all stages with acceptable flags will be release to the archive. The data will be accompanied by the spectral residuals, standard error, fraction of explained variance, and correlation length.

## 4.0 ALGORITHM VERIFICATION

### 4.1 END-TO-END CLOSURE EXPERIMENTS

The purpose of the end-to-end closure experiments using the TES reference and operational software is to test the robustness of TES level 2 retrieval algorithms and the operational software and to identify any problems either in the algorithm or in coding. This procedure will also be helpful for algorithm validations. A single step end-to-end simulation would be to add noise to the model radiance and then to execute a step retrieval defined in the TES retrieval strategies. A full end-to-end closure experiment would be to generate a full four-day global survey set of radiances with added noise and clouds and then to carry out the four-day retrieval processing.

Establishing a profile/parameter database which consists collections of measured atmospheric temperature and constituent profiles and surface parameter data by all means of observations, sonde, balloon, aircraft, satellite, etc. is one of the key activities for the pre-launch closure experiments. These profiles/parameters along with model simulated profiles allow us to compile the baseline initial guesses and the *a priori* (see sections 3.5.3 and 3.5.4), to simulate the observed spectral radiance, and to evaluate the retrieval results for all the possible atmospheric conditions including extreme cases. Global cloud coverage data will also be obtained so that the simulated TES global pixel measurements will be more realistic.

The end-to-end closure experiments will follow three procedures: (1) simulate the TES observations using collected measurement profiles/surface parameters/cloud coverage as the true atmospheric full state with added noise, (2) generate TES retrieval products using a defined initial guess, and (3) examine and evaluate the retrieval results and error analysis by comparing with the “smoothed true profiles” and their statistical variance. Since the level 2 software will be developed in steps from a single profile retrieval to automated four-day data retrieval, the end-to-end experiment can be performed at each step.

### 4.2 VALIDATION

Validation, in the sense used here, differs from validation of the TES measurements in that we will use pre-existing data that have already been analyzed by others. The objective is to ensure that the TES algorithm either produces identical results or there are plausible reasons why it does not. Measurement validation will employ near-concurrent and co-located measurements and is not further discussed in this document (although, of course, it is a crucial part of the overall TES experiment).

Data sources currently identified that are (or will be) appropriate for this purpose are

1) Airborne Emission Spectrometer (AES). AES operates in both a downlooking mode from a variety of aircraft and uplooking from the surface. It was specifically designed to cover the same spectral region at the same resolution as TES and is therefore a prime data source for validation exercises. Downlooking data are very similar to the TES nadir mode and uplooking data are a useful surrogate for TES limb data.

2) AERI (Atmospheric Emitted Radiation Interferometer). AERI is a well calibrated,  $1\text{ cm}^{-1}$  spectral resolution, uplooking, Michelson interferometer covering the range 550 to 1700 and 2000 to  $2500\text{ cm}^{-1}$ . Several copies of the instrument are operational – the one of primary interest for TES validation is located at the Central facility of the ARM Cloud And Radiation Test (CART) site in northern Oklahoma. The AERI-X (eXtended resolution AERI) is also located at the central

facility. It has  $0.1\text{ cm}^{-1}$  spectral resolution, but only covers  $550$  to  $1600\text{ cm}^{-1}$ . The ARM program provides good temperature and water vapor information about the atmosphere overhead. Information about ozone and other stratospheric gases, as well as aerosol optical depth, is available from solar absorption instruments at the site.

3) HIS (High resolution Interferometric Sounder). HIS is an autonomous FTS that flies on the ER2 in a variety of campaigns with the goal of temperature and water vapor sounding. Some of the more recent campaigns have been in support of tropospheric chemistry missions, where independent measurements may also be available. Although the spectral resolution is lower, the data are from an altitude that is more “space-like” than the AES data.

4) IMG (Interferometric Monitor of Greenhouse Gases). IMG, a nadir sounder developed by the Japanese, flew on the ADEOS mission (which failed in June 1997). Nevertheless, it represents the only available source of real space-based data with spectral coverage and resolution very close to that of TES. Some tests using IMG data are already ongoing and more are planned.

5) MIPAS (Michelson Interferometer for Passive Atmospheric Sounding). MIPAS will fly on the ENVISAT mission at least one year before TES. It is a limb sounder with slightly poorer spectral resolution than TES but will nevertheless be the only available source of space-based limb emission data prior to TES, so it will be a very valuable validation tool.

6) NAST-I (NPOESS Aircraft Sounder Testbed – Interferometer). NAST-I is a nadir-viewing instrument that has flown on several ER2 missions, including CAMEX-3, with correlative radiosonde measurements. It has a spectral resolution of  $0.25\text{ cm}^{-1}$  covering the spectral regime  $590$ - $2810\text{ cm}^{-1}$ . As a testbed to the NPOESS candidate instruments, it has been used to simulate “space-like” ground coverage views for the validation of key meteorological species.

## 5.0 REFERENCES

### 1.0 INTRODUCTION

*Execution Phase Project Plan for the Earth Observing System (EOS)*. GSFC 170-01-01, Rev. A, May 1995.

*Mission to Planet Earth Strategic Enterprise Plan 1996-2002*. NASA HQ MTPE, May 1996.

*Tropospheric Emission Spectrometer: Scientific Objectives & Approach, Goals & Requirements*. JPL D-11294, Rev. 5.0, May 1996.

### 2.0 BACKGROUND

Rothman, L.S., C.P. Rinsland, A. Goldman, S.T. Massie, D.P. Edwards, J.-M. Flaud, A. Perrin, C. Camy-Peyret, V. Dana, J.-Y. Mandin, J. Schroeder, A. McCann, R.R. Gamache, R.B. Wattson, K. Yoshino, K.V. Chance, K.W. Jucks, L.R. Brown, V. Nemtchinov, and P. Varanasi, The HITRAN Molecular Spectroscopic Database and HAWKS (HITRAN Atmospheric Workstation): 1996 Edition, *J. Quant. Spectrosc. Radiat. Transfer*, 60, 665-710, 1998.

TES Level 1B ATBD, JPL D-16479, October 1, 1999.

### 3.0 ALGORITHM DESCRIPTION

#### 3.1 ALGORITHM OVERVIEW

*TES Level 1B Algorithm Theoretical Basis Document*, JPL D-16479, 1999.

##### 3.2.4.1 Spectral grid for radiative transfer

Clough, S.A. and F.X. Kneizys, Convolution algorithm for the lorentz function. *Applied Optics*, 18, 2329, 1979.

##### 3.3.1.4 Atmospheric Radiance

Clough, S.A., F.X. Kneizys, E.P. Shettle, G.P. Anderson, Atmospheric radiance and transmittance, FASCOD2, in *Proceedings of the Sixth Conference on Atmospheric Radiation, Extended Abstracts (American Meteorological Society)*, Williamsburg, VA, May 13-16, pp. 141-144, 1986.

Clough, S.A., F.X. Kneizys, L.S. Rothman and W.O. Gallery, Atmospheric spectral transmittance and radiance: FASCOD1B. In *Proceedings of the SPIE* 277, 152-166, 1981.

##### 3.3.1.6 Solar Radiance

Rinsland, C.P., G.K. Yie, M.R. Gunson, R. Zander, and M.C. Abrams, Mid-infrared extinction by sulfate aerosols from the Mt. Pinatubo eruption, *J. Quant. Spectrosc. Radiat. Transfer*, 52, 241-252, 1994.

##### 3.3.1.7 Surface Contribution

Goody, R.M and Y.L. Yung, *Atmospheric Radiation, Theoretical Basis*, Second Edition, Oxford University Press, 1989.

### 3.3.2.1 Surface Radiative Properties

Smith, W. L., R. O. Knuteson, H. E. Revercomb, W. Feltz, H.B. Howell, W.P. Menzel, N. Nalli, O. Brown, J. Brown, P. Minnett, and W. McKeown, Observations of the Infrared Radiative Properties of the Ocean - Implications for the Measurement of Sea Surface Temperature via Satellite Remote Sensing, *Bull. Amer. Meteor. Soc.*, January 1996.

Masuda, K.T., Takashima and Y. Takayama: Emissivity of pure and sea waters for the model sea surface in the infrared window regions, *Remote Sens. Environ.*, 24, 313-329, 1988.

### 3.3.3 Radiative Transfer for Aerosols

Moncet, J.-L. and S.A. Clough (1997): Accelerated monochromatic radiative transfer for scattering atmospheres: Application of a new model to spectral radiance observations. *J. Geophys. Res.*, 102, 21,853-21,866.

### 3.3.4 Solar Source Function

Gunson, M.R., M.M. Abbas, M.C. Abrams, M. Allan, L.R. Brown, T.L. Brown, A.Y. Chang, A. Goldman, F.W. Irion, L.L. Lowes, E. Mahieu, G.L. Manney, H.A. Michelsen, M.J. Newchurch, C.P. Rinsland, R.J. Salawitch, G.P. Stiller, G.C. Toon, Y.L. Yung, and R. Zander, The Atmospheric Trace Molecule Spectroscopy (ATMOS) experiment: Deployment on the ATLAS Space Shuttle missions, *Geophys. Res. Lett.*, 23, 2333-2336, 1996.

Kurucz, R.L., The solar spectrum: Atlases and line identifications, in *Laboratory and Astronomical High Resolution Spectra*, 81, edited by A.J. Sauval, R. Blomme, and N. Grevesse, Astron. Soc. of the Pacific Coast, 17-31, 1995.

Kurucz, R.L., Synthetic infrared spectra, in *Infrared Solar Physics*, IAU Symp. 154, edited by D.M. Rabin and J.T. Jefferies, Kluwer Acad., Norwell, MA, 1992a.

Kurucz, R.L., Atomic and molecular data for opacity calculations, *Revista Mexicana de Astronomia y Astrofisica*, 23, 45-48, 1992b.

Kurucz, R.L., Finding the missing solar ultraviolet opacity, *Revista Mexicana de Astronomia y Astrofisica*, 23, 181-186, 1992c.

Kurucz, R.L., Remaining line opacity problems for the solar spectrum, *Revista Mexicana de Astronomia y Astrofisica*, 23, 187-194, 1992d.

Kurucz, R.L., I. Furenlid, J. Brault, and L. Testerman, *Solar Flux Atlas from 296 to 1300 nm*, 240 pp., National Solar Observatory, Sunspot, New Mexico, 1984.

### 3.3.7.1 ABSCO Table Generation

Anderson, G.P., S.A. Clough, F.X. Kneizys, J.H. Chetwynd, and E.P. Shettle, *AFGL atmospheric constituent profiles (0-120 km)*. AFGL-TR-86-0110, 1986.

National Aeronautics and Space Administration, (1976). *U.S. Standard Atmosphere Supplements*, U.S. Government Printing Office, Washington, D.C., 1976.

### 3.3.7.2 TES Line-by-Line Code

Clough, S.A. and M.J. Iacono (1995): Line-by-Line Calculations of Atmospheric Fluxes and Cooling Rates II: Application to Carbon Dioxide, Ozone, Methane, Nitrous Oxide, and the Halocarbons. *J. Geophys. Res.*, 100, 16,519-16,535.

Clough, S.A., M.J. Iacono, and J.-L. Moncet, Line-by-line calculation of atmospheric fluxes and cooling rates: Application to water vapor. *J. Geophys. Res.*, 97, 15761-15785, 1992.

Hoke, M. L., S. A. Clough, W. Lafferty, and B. Olson, Line coupling in oxygen and carbon dioxide, in *IRS '88: Current Problems in Atmospheric Radiation*, edited by J. Lenoble and J. F. Geleyn, pp. 368-370, A. Deepak Publishing, Hampton, VA, 1989.

Mlawer, E.J., S.J. Taubman, P.D. Brown, M.J. Iacono and S.A. Clough, Radiative Transfer for Inhomogeneous Atmospheres: RRTM, a Validated correlated-k model for the longwave. *J. Geophys. Res.*, 102, 16,663-16,682, 1997.

Rothman, L. S., R. R. Gamache, R. Tipping, C. P. Rinsland, M. A. H. Smith, D. C. Benner, V. Malathy Devi, J.-M. Flaud, C. Camy-Peyret, A. Goldman, S. T. Massie, L. R. Brown, and R. A. Toth, HITRAN molecular database: Edition of 1991 and 1992, *J. Quant. Spectrosc. Radiat. Transfer*, 48, 469-507, 1992.

Tobin, D. C., F. A. Best, P. D. Brown, S. A. Clough, R. G. Dedeker, R. G. Ellingson, R. K. Garcia, H. B. Howell, R. O. Knuteson, E. J. Mlawer, H. E. Revercomb, J. F. Short, P. F. W. van Delst, and V. P. Walden, Downwelling Spectral Radiance Observations at the SHEBA Ice Station: Water Vapor Continuum Measurements from 17-26 micrometer, *J. Geophys. Res.*, 1999, in press.

### 3.3.8 ABSCO Databases

National Aeronautics and Space Administration, (1976). *U.S. Standard Atmosphere Supplements*, U.S. Government Printing Office, Washington, D.C., 1976.

#### 3.3.8.1 Line Parameters

Brown, L. R., M. R. Gunson, R. A. Toth, F. W. Irion, C. P. Rinsland, and A. Goldman, The 1995 Atmospheric Trace Molecule Spectroscopy (ATMOS) Linelist. *Appl. Opt.*, 35, 2828-2848, 1996.

Rothman, L.S., C.P. Rinsland, A. Goldman, S.T. Massie, D.P. Edwards, J.-M. Flaud, A. Perrin, C. Camy-Peyret, V. Dana, J.-Y. Mandin, J. Schroeder, A. McCann, R.R. Gamache, R.B. Wattson, K. Yoshino, K.V. Chance, K.W. Jucks, L.R. Brown, V. Nemtchinov, and P. Varanasi, The HITRAN Molecular Spectroscopic Database and HAWKS (HITRAN Atmospheric Workstation): 1996 Edition, *J. Quant. Spectrosc. Radiat. Transfer*, 60, 665-710, 1998.

#### 3.3.8.2 Cross-Sections

Ballard, J., W.B. Johnston, M.R. Gunson, and P.T. Wassel, Absolute absorption coefficients of ClONO<sub>2</sub> infrared bands at stratospheric temperatures, *J. Geophys. Res.* 93, 1659-1665, 1988.

Camy-Peyret, C., J.-M. Flaud, L. Lechuga-Fossat, C. Laverdet and G. Le Bras, The Absorption of Gaseous Dinitrogen Pentoxide in the 8.1 and 5.7  $\mu\text{m}$  Spectral Regions, *Chem. Phys. Lett.* 139, 345-349, 1987.



Clerbaux, C., R. Colin, P.C. Simon and C. Granier, Infrared Cross Sections and Global Warming Potentials of 10 Alternative Hydrohalocarbons, *J. Geophys. Res.* 98, 10491-10497, 1993.

Cantrell, C.A., J.A. Davidson, A.H. McDaniel, R.E. Shetter, and J.G. Calvert, *Chem. Phys. Lett.* 148, 358-363, 1988; Erratum *Chem. Phys. Lett.* 152, 274, 1988.

Jacquinet-Husson, N., E. Ari  , J. Ballard, A. Barbe, L.R. Brown, B. Bonnet, C. Camy-Peyret, J.P. Champion, A. Ch  din, A. Chursin, C. Clerbaux, G. Duxbury, J.M. Flaud, N. Fourri  , A. Fayt, G. Graner, R. Gamache, A. Goldman, V.I. Golovko, G. Guelachvilli, J.M. Hartmann, J.C. Hillico, G. Lef  vre, O.V. Naumenko, V. Nemtchinov, D.A. Newnham, A. Nikitin, J. Orphal, A. Perrin, D.C. Reuter, L. Rosenmann, L.S. Rothman, N.A. Scott, J. Selby, L.N. Sinita, J.M. Sirota, A.M. Smith, K.M. Smith, V.I.G. Tyuterev, R.H. Tipping, S. Urban, P. Varanasi, M. Weber, The 1997 Spectroscopic GEISA Databank, *J. Quant. Spectrosc. Radiat. Transfer*, in press, 1998.

Li, Z., and P. Varanasi, Measurement of the Absorption Cross-Sections of CFC-11 at Conditions Representing Various Model Atmospheres, *J. Quant. Spectrosc. Radiat. Transfer*, 52, 137-144, 1994.

Massie, S.T., A. Goldman, D.G. Murcray and J.C. Gille, Approximate absorption cross sections of F12, F11, ClONO<sub>2</sub>, HNO<sub>3</sub>, CCl<sub>4</sub>, CF<sub>4</sub>, F21, F113, F114, and HNO<sub>3</sub>, *Appl. Opt.*, 24, 3426-3427, 1985.

Massie, S.T., A. Goldman, A.H. McDaniel, C.A. Cantrell, J.A. Davidson, R.E. Shetter, and J.G. Calvert, Temperature Dependent Infrared Cross Sections for CFC-11, CFC-12, CFC-13, CFC-14, CFC-22, CFC-113, CFC-114, and CFC-115, *NCAR Technical Note/TN-358+STR*, 1991.

Massie, S.T., and A. Goldman, Absorption Parameters of very Dense Molecular Spectra for the HITRAN Compilation, *J. Quant. Spectrosc. Radiat. Transfer*, 48, 713-719, 1992.

McDaniel, A.H., C.A. Cantrell, J.A. Davidson, R.E. Shetter, and J.G. Calvert, The Temperature Dependent, Infrared Absorption Cross-Sections for the Chlorofluorocarbons: CFC-11, CFC-12, CFC-13, CFC-14, CFC-22, CFC-113, CFC-114, and CFC-115, *J. Atmos. Chem.*, 12, 211-227, 1991.

Orlando, J.J., G.S. Tyndall, A. Huang, and J.G. Calvert, Temperature Dependence of the Infrared Absorption Cross Sections of the Carbon Tetrachloride, *Geophys. Res. Lett.*, 19, 1005-1008, 1992.

Orphal, J., M. Morillon-Chapey, and G. Guelachvili, High-Resolution Absorption Cross Sections of Chlorine Nitrate in the  $\nu_2$  Band Region Around 1292 cm<sup>-1</sup> at Stratospheric Temperatures, *J. Geophys. Res.*, 99, 14,549-14,555, 1994.

Rothman, L.S., C.P. Rinsland, A. Goldman, S.T. Massie, D.P. Edwards, J.-M. Flaud, A. Perrin, C. Camy-Peyret, V. Dana, J.-Y. Mandin, J. Schroeder, A. McCann, R.R. Gamache, R.B. Wattson, K. Yoshino, K.V. Chance, K.W. Jucks, L.R. Brown, V. Nemtchinov, and P. Varanasi, The HITRAN Molecular Spectroscopic Database and HAWKS (HITRAN Atmospheric Workstation): 1996 Edition, *J. Quant. Spectrosc. Radiat. Transfer*, 60, 665-710, 1998.

Smith, K., D. Newnham, M. Page, J. Ballard, and G. Duxbury, Infrared Band Strengths and Absorption Cross-Sections of HFC-32 Vapor, *J. Quant. Spectrosc. Radiat. Transfer*, 56, 73-82, 1996.

Smith, K., D. Newnham, M. Page, J. Ballard, and G. Duxbury, Infrared Absorption Cross-Sections and Integrated Absorption Intensities of HFC-134 and HFC-143a Vapour, *J. Quant. Spectrosc. Radiat. Transfer*, 59, 437-451, 1998.

Varanasi, P., A. Gopalan, and J.F. Brannon Jr., Infrared Absorption Coefficient Data on SF<sub>6</sub> Applicable to Atmospheric Remote Sensing, *J. Quant. Spectrosc. Radiat. Transfer*, 48, 141-145, 1992a.

Varanasi, P., Absorption Coefficients of CFC-11 and CFC-12 needed for Atmospheric Remote Sensing and Global Warming Studies, *J. Quant. Spectrosc. Radiat. Transfer*, 48, 205-219, 1992b.

Varanasi, P., Absorption Spectra of HCFC-22 around 829 cm<sup>-1</sup> at Atmospheric Conditions, *J. Quant. Spectrosc. Radiat. Transfer*, 47, 251-255, 1992c.

Varanasi, P., and V. Nemtchinov, Thermal Infrared Absorption Coefficients of CFC-12 at Atmospheric Conditions, *J. Quant. Spectrosc. Radiat. Transfer*, 51, 679-687, 1994.

Varanasi, P., Z. Li, V. Nemtchinov, and A. Cherukuri, Spectral Absorption-Coefficient Data on HCFC-22 and SF<sub>6</sub> for Remote-Sensing Applications, *J. Quant. Spectrosc. Radiat. Transfer*, 52, 323-332, 1994.

Goody, R.M and Y.L. Yung, *Atmospheric Radiation, Theoretical Basis*, Second Edition, Oxford University Press, 1989.

### 3.3.8.3 Aerosols

Massie, S. T., Indices of refraction for the HITRAN compilation, *J. Quant. Spectrosc. Radiat. Transfer*, 52, 501-513, 1994.

Rinsland, C. P., G. K. Yue, M. R. Gunson, R. Zander, and M. C. Abrams, Mid-infrared extinction by sulfate aerosols from Mt. Pinatubo eruption, *J. Quant. Spectrosc. Radiat. Transfer*, 52, 241-252, 1994.

Rothman, L.S., C.P. Rinsland, A. Goldman, S.T. Massie, D.P. Edwards, J.-M. Flaud, A. Perrin, C. Camy-Peyret, V. Dana, J.-Y. Mandin, J. Schroeder, A. McCann, R.R. Gamache, R.B. Wattson, K. Yoshino, K.V. Chance, K.W. Jucks, L.R. Brown, V. Nemtchinov, and P. Varanasi, The HITRAN Molecular Spectroscopic Database and HAWKS (HITRAN Atmospheric Workstation): 1996 Edition, *J. Quant. Spectrosc. Radiat. Transfer*, 60, 665-710, 1998.

### 3.3.8.4 Continuum

Clough, S. A., F. X. Kneizys, and R. W. Davies: Line shape and the water vapor continuum, *Atmos. Res.*, 23, 229-241, 1980.

Clough, S.A. and M.J. Iacono, Line-by-Line Calculations of Atmospheric Fluxes and Cooling Rates II: Application to Carbon Dioxide, Ozone, Methane, Nitrous Oxide, and the Halocarbons. *J. Geophys. Res.*, 100, 16,519-16,535, 1995.

Clough, S.A., The water vapor continuum and its role in remote sensing, in *Optical Remote Sensing of the Atmosphere, Vol. 2, 1995, OSA Technical Digest Series*, Optical Society of America, Washington, DC, pp. 76-81, 1995.

Clough, S.A., M.J. Iacono, J.-L. Moncet, Line-by-Line Calculation of Atmospheric Fluxes and Cooling Rates: Application to Water Vapor. *J. Geophys. Res.*, 97, 15761-15785, 1992.

Clough, S.A., F.X. Kneizys, and R. W. Davies, Line shape and the water vapor continuum. *Atmospheric Research*, 23, 229-241, 1989.

Han, Y., J.A. Shaw, J.H. Churnside, P.D. Brown and S. A. Clough, Infrared spectral Radiance measurements in the tropical Pacific atmosphere, *J. Geophys. Res.*, 102, 4,353-4,356, 1997.

Lafferty, W.J., A.M. Solodov, A. Weber, W.B. Olson and J.-M. Hartmann, Infrared collision-induced absorption by  $N_2$  near 4.3 microns for atmospheric applications: measurements and empirical modeling, *Appl. Optics*, 35, 5911-5917, (1996).

Mlawer, E.J., S.A. Clough, P.D. Brown, and D.C. Tobin, A new formulation for the water vapor continuum, *Proceedings of the 8th Atmospheric Radiation Measurement (ARM) Science Team Meeting*, Tucson, Arizona, 1999 (in press).

Thibault, F., V. Menoux, R. Le Doucen, L. Rosenman, J.-M. Hartmann, and Ch. Boulet Infrared collision-induced absorption by  $O_2$  near 6.4 microns for atmospheric applications: measurements and empirical modeling, *Appl. Optics*, 35, 5911-5917, 1996.

Tobin, D. C., F. A. Best, P. D. Brown, S. A. Clough, R. G. Dedeker, R. G. Ellingson, R. K. Garcia, H. B. Howell, R. O. Knuteson, E. J. Mlawer, H. E. Revercomb, J. F. Short, P. F. W. van Delst, and V. P. Walden, Downwelling Spectral Radiance Observations at the SHEBA Ice Station: Water Vapor Continuum Measurements from 17-26 micrometer, *J. Geophys. Res.*, 1999, in press.

Tobin, D.C., L.L. Strow, W.J. Lafferty and W.B. Olson, Experimental investigation of the self- and  $N_2$ -broadened continuum within the  $v_2$  band of water vapor, *Appl. Opt.*, 35, 4274-4734, 1996.

### 3.5 Retrieval

Fletcher, R., *Practical Methods of Optimization*, 2<sup>nd</sup> Edition, John Wiley & Sons, 1993.

Gill, P. E., W. Murray, and M. H. Wright, *Practical Optimization*, Academic Press, 1981.

Lambert, A., R.G. Grainger, J.J. Remedios, W.J. Reburn, C.D. Rodgers, F.W. Taylor, J.L. Mergenthaler, J.B. Kumer, S.T. Massie and T. Deshler, Validation of Aerosol Measurements by the Improved Stratospheric And Mesospheric Sounder, *J. Geophys. Res.*, 101, 9811-9830, 1996.

Press, W. H., B. P. Flannery, S. A. Teukolsky, and W. T. Vetterling, *Numerical Recipes*, Cambridge University Press, New York, 1989.

Twomey, S. On the numerical solution of Fredholm integral equations of the first kind by the inversion of the linear system produced by quadrature. *J. Ass. Comput. Mach.*, 10, p 97, 1963.

Wylie, D.P., W.P. Menzel, H.M. Woolf, and K.I. Strabala: Four Years of Global Cirrus Cloud Statistics Using HIRS. *J. Climate*, 7, 1972-1986, 1994.

#### **3.5.4.2.3 Strategy for Limb Pointing Retrieval**

Anderson, G.P., S.A. Clough, F.X. Kneizys, J.H. Chetwynd, and E.P. Shettle, *AFGL atmospheric constituent profiles (0-120 km)*, AFGL-TR-86-0110, 1986.

#### **3.5.4.3 Numerical Solution**

More', J. Jorge, The Levenberg-Marquardt Algorithm: Theory and Implementation, *Numerical Analysis: Proceedings, Biennial Conference*, Dundee, 1977.

Marquardt, D., An algorithm for least squares estimation of nonlinear parameters., *J. Soc. Indust. Appl. Math* 11:431-441, 1963.

#### **3.5.5 Clear Pixel Identification (nadir)**

Wylie, D.P., W.P. Menzel, H.M. Woolf, and K.I. Strabala, 1994: Four Years of Global Cirrus Cloud Statistics Using HIRS. *J. Climate*, **7**, 1972-1986.

Ackerman, S.A., K. Strabala, W.P. Menzel, R.A. Frey, C.C. Moeller and L.E. Gumley, "Discriminating clear sky from clouds with MODIS", *J. Geophys. Res.*, 103, 32141-32157, 1998.

#### **3.5.7 Retrieval Microwindow Selection**

Rodgers, C. D. Information content and optimisation of high spectral resolution measurements, SPIE, Vol 2830, *Optical Spectroscopic Techniques and Instrumentation for Atmospheric and Space Research II*, Paul B. Hays and Jinxue Wang, eds., 136-147, 1996.

von Clarmann, T and G. Echle, Selection of optimized microwindows for atmospheric spectroscopy, *Appl Opt.*, **37**, 7661-7669, 1998.

#### **3.5.8 A Priori Database Generation**

Heinemann, G., N.S. Chedin, N. Scott and C. Claud, Sensitivity studies of TOVS retrievals with 3I and ITPP retrieval algorithms. Application to the resolution of mesoscale phenomena in the Antarctic, *Meteorology and Atmospheric Physics*, v55, pp87-100, 1995.

Logan, J.A., An analysis of ozonesonde data for the troposphere: recommendations for testing 3-D models and development of a gridded climatology for tropospheric ozone, submitted to *J. Geophys. Res.*, July 1998.

Logan, J.A., An analysis of ozonesonde data for the lower stratosphere: recommendations for testing models, submitted to *J. Geophys. Res.*, July 1998.

## APPENDICES

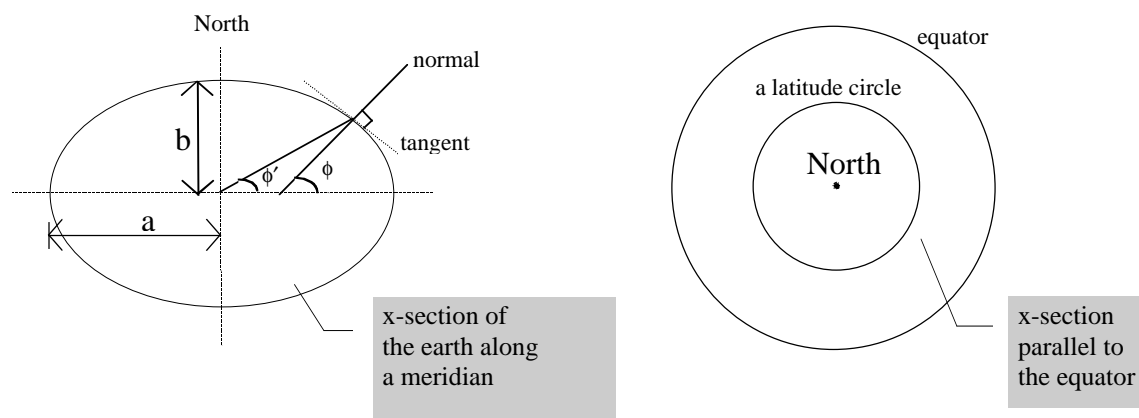
### A3.3.1: Radiative Transfer

The Radius of Curvature of the Earth's Surface for a Given TES Limb Tangent Latitude and Viewing Direction

The ray-tracing step in Level 2 process uses Snell's Law for a spherically symmetric atmosphere to determine the bending along the ray. The radius of the "sphere" is considered to be the sum of the altitude and the *radius of curvature of the Earth surface* (not the Earth-centered radius) at the given location in the given direction. This Appendix presents the equations for the radius of the Earth surface curvature at a given latitude (TES limb tangent latitude) for TES viewing direction.

A very commonly used Earth geometric model is an ellipsoidal shape as illustrated below.

**Figure A - 1: Earth Geometric Model**



Definitions of some parameters:

- $a$  — equatorial radius (the semi-major axis of the meridian ellipse).
- $b$  — polar radius (the semi-minor axis of the meridian ellipse).
- $f$  — flattening factor.
- $e$  — Earth ellipsoid eccentricity.
- $\phi$  — geodetic latitude as illustrated above.
- $\phi'$  — geocentric latitude as illustrated above.

Their relationships:

$$\tan(\phi) = \frac{\tan(\phi')}{(1 - f)^2}; \quad (\text{A1.1})$$

$$f = \frac{a-b}{a}; \text{ and} \quad (A1.2)$$

$$e = \sqrt{2f - f^2}. \quad (A1.3)$$

There are two principle curvatures on the model Earth surface at a given location, the meridian curvature (North-South curvature) and the East-West curvature. The tangents of these two curvature are perpendicular. The East-West curvature plane is defined by the tangent along a latitude circle and the local normal. The equations for the radius of these two principle curvature planes are:

Radius of curvature in the North-South plane:

$$R_{NS} = \frac{a(1 - e^2)}{(1 - e^2 \sin^2 \phi)^{3/2}}. \quad (A1.4)$$

Radius of curvature in the East-West plane:

$$R_{EW} = \frac{a}{(1 - e^2 \sin^2 \phi)^{1/2}}. \quad (A1.5)$$

TES always looks straight backward along the orbit. The orbit has 98.21° inclination angle which is the angle between the equatorial plane and the orbital plane. The parameter to define the TES viewing direction at its limb tangent point or any point along its line of sight is the azimuth angle ( $A_z$ ). The azimuth angle is the angle between the local meridian plane (the N-S plane) and the plane defined by the local normal and the tangent along the TES viewing direction. Under the spherical approximation,  $A_z$  can be calculated as

$$\sin(A_z) = \frac{\cos(\text{inclination angle})}{\cos(\text{geocentric latitude})}. \quad (A1.6)$$

The EOS Toolkit provides a program to calculate a more rigorous azimuth without the spherical approximation (PGS\_CSC\_ZenithAzimuth). The viewing vector however, in the ECR (Earth Centered Rotating) coordinate system, needs to be defined.

The radius of the curvature in azimuth  $A_z$  ( $R_C$ ) can be calculated as

Radius of curvature in azimuth  $A_z$ :

$$\frac{1}{R_C} = \frac{\cos^2(A_z)}{R_{NS}} + \frac{\sin^2(A_z)}{R_{EW}}. \quad (A1.7)$$

### A3.3.1.1: Ray Tracing and Path Integrals

For ray tracing and path integrals, we require the following elements from the retrieval vector, at a set of levels  $j=0..n$  in  $\ln(P)$ , and in the limb case when the atmosphere is not horizontally homogeneous, also at a set of locations along the line of sight:

$T_j$	level temperatures
$q_{jm}$	level mixing ratios for molecule m
$P_s$	surface pressure
$T_s$	surface temperature

and the following forward model parameters:

$z_s$	altitude of the surface relative to the geoid
$R_c$	radius of the geoid at the measurement location
$R_{cs}$	altitude of the spacecraft from the center of curvature of the geoid
$\theta_s$	angle of ray at the satellite

The level quantities in the retrieval vector are interpolated at a finer spacing to give the full grid level values  $q_k^m$  and  $T_k$ .

#### A3.3.1.1.1 Hydrostatic Equation

The total air density  $\rho_k$  is computed from the gas equation at each full grid level. This must allow for the water content of the air, but the other minor constituents may be ignored [except possibly CO<sub>2</sub>] (see Appendix 3.3.1.1.7). The hydrostatic equation may be written

$$dz = -[P/\rho(P)g(z)] d \ln(P) \quad (A2.1)$$

As the quantity  $[P/\rho(z)g(z)]$  is close to  $RT/Mg$ , from the ideal gas equation, we take it to be linear in  $\ln(P)$  over each layer. Hence the layer thickness is

$$z_k - z_{k-1} = (P_{k-1}/\rho_{k-1}g_{k-1} + P_k/\rho_k g_k)[\ln(P_{k-1}) - \ln(P_k)]/2 \quad (A2.2)$$

from the trapezoidal rule. The acceleration due to gravity is given as a function of height and latitude, and it consists of gravitational and rotational parts,

$$g(\phi, z) = g_{\text{grav}}(\phi, 0)[(R_e)/(R_e + z)]^2 - \Omega^2 N [((N+z)/R_e) \cos \phi]^2 \quad (A2.3)$$

where  $\Omega$  is the Earth's rotational angular frequency;  $N = a^2 \sqrt{(a^2 - (a^2 - b^2) \sin^2 \phi)}$ ; and  $a$  and  $b$  is the semi-major and minor axis of earth respectively. The gravitational term at the earth surface is given by [International Gravity Formula, 1980]

$$g(\phi, 0) = 978.0327(1.0 + 0.0052790414 \sin^2 \phi + 0.0000232718 \sin^4 \phi + 0.0000001262 \sin^6 \phi),$$

$$\text{and } \sigma_{\text{grat}}(\phi, \rho) = \sigma(\phi, \rho) - \sigma_{\text{rat}}(\phi, \rho). \quad (\text{A2.4})$$

Note that equation (A2.2) requires  $g_k = g(z_k)$  before  $z_k$  has been computed. The effect is small and can be accommodated by several different ways, of which the simplest might be to approximate  $g_k$  by its value at an altitude given by  $2z_{k-1} - z_{k-2}$ .

#### *A3.3.1.1.2 Ray tracing in the nadir case.*

The zenith angle of the ray at each level is given by Snell's law in spherical symmetry:

$$\sin \theta_k = [R_{cs} \sin \theta_s] / [(R_c + z_k) n_k] \quad (\text{A2.5})$$

where the refractive index  $n_k$  is given in section A3.3.1.1.8. However as  $n_k \sim 1.0002$  at the surface, it may be ignored, incurring an error of only 0.02% in  $\sin \theta_k$ , and hence a similarly small amount in path length through  $\sec \theta_k$ .

#### *A3.3.1.1.3 Path integrals in the nadir case*

We need to evaluate the number of molecules per unit area in each layer, together with appropriately weighted mean pressures and temperatures of the layer. The mass per unit area of an element  $dP$  is  $dP/g$ , so the number of molecules of molecule  $m$  is

$$dn_m = N q_m dP / g [M_d + q^w M_w] \quad (\text{A2.6})$$

where  $N$  is Avogadro's number,  $q_m$  is the volume mixing ratio of molecule  $m$ , defined as the ratio to the number of molecules of dry air,  $M_d$  and  $M_w$  are the molar masses of dry air and water, and  $q^w$  is the mixing ratio of water vapor. Hence the number of molecules of  $m$  in a layer along the line of sight is

$$u_{lm} = - \int_{l_{l-1}}^l q_m(P) f(P) dP \quad (\text{A2.7})$$

where

$$f(P) = \sec \theta N / g [M_d + q^w M_w] \quad (\text{A2.8})$$

is very nearly constant over a layer. Interpolating  $\ln(f)$  as well as  $\ln(q_m)$  linearly in  $\ln(P)$ , we obtain integrals that can be evaluated analytically. Putting

$$q_m f = q_{ml} f_{l-1} (P/P_{l-1})^{\alpha_l} \quad (\text{A2.9})$$

within the layer, where  $\alpha_l = \ln(q_{ml} f_l / q_{ml-1} f_{l-1}) / (\zeta_l - \zeta_{l-1})$ , we obtain

$$\begin{aligned} u_{lm} &= [q_{ml-1} f_{l-1} P_{l-1} - q_{ml} f_l P_l] / (1 + \alpha_l) \\ &= q_{ml-1} f_{l-1} P_{l-1} (\zeta_l - \zeta_{l-1}) E[(1 + \alpha_l)(\zeta_l - \zeta_{l-1})] \end{aligned} \quad (\text{A2.10})$$

where  $E(x) = [1 - \exp(-x)]/x$ , which will need special evaluation near  $x=0$ . The first form is simpler, but the second form is needed when  $(1 + \alpha_l) \sim 0$ . We also require the weighted mean pressure and temperature obtained from

$$u_{lm} \bar{P}_l = - \int_{l_{l-1}}^l q_m f P dP \quad (\text{A2.11})$$



$$u_{lm} \overline{T}_l = - \int_{l-1}^l q_m f T dP \quad (A.2.12)$$

in order to evaluate the optical depth

$$\tau_v = k_v(\overline{P}, \overline{T}) u \quad (A.2.13)$$

where  $k_v$  is the absorption coefficient (cross section) to be interpolated from a tabulation against pressure and temperature. We easily obtain

$$\begin{aligned} u_{lm} \overline{P}_l &= [q_{ml-1} f_{l-1} P_{l-1}^2 - q_{ml} f_l P_l^2] / (2 + \alpha_l) \\ &= q_{ml-1} f_{l-1} P_{l-1}^2 (\zeta_l - \zeta_{l-1}) E[(2 + \alpha_l)(\zeta_l - \zeta_{l-1})] \end{aligned} \quad (A.2.14)$$

The temperature integral can also be performed algebraically, but leads to slightly more complicated expressions.

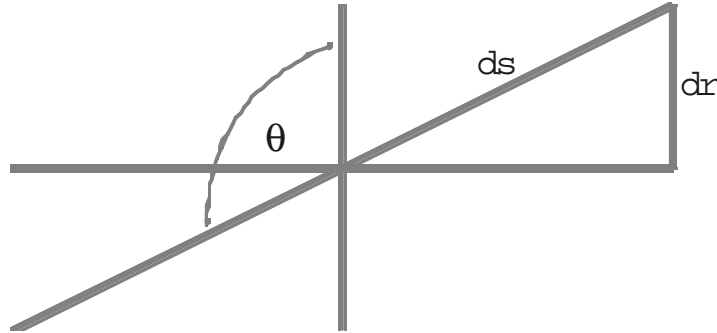
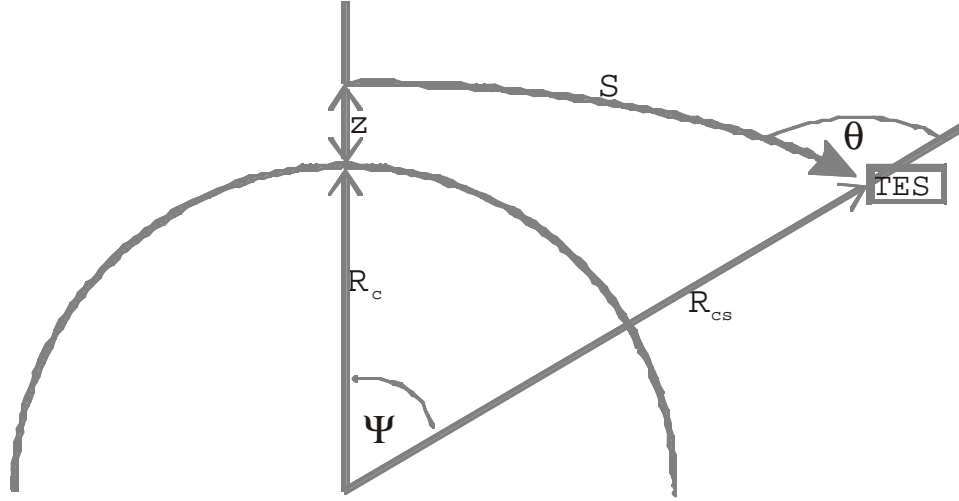
For computational efficiency we wish to avoid a two dimensional interpolation in the absorption coefficient tables. The mean pressure is therefore approximated by its value at  $\alpha_l = 0$ , and the tabulation made at the corresponding set of layer mean pressures,  $\overline{P}_l = (P_l + P_{l-1})/2$ . This approximation is in error by 1.2% in pressure at  $\alpha = < 1$  for a layer thickness of 1 UARS layer, and is quadratic in layer thickness.

#### *A3.3.1.1.4 Ray Tracing in the Limb Case*

To avoid a pressure interpolation in the absorption coefficient table in the forward model, we need to predetermine the layer mean pressures in order to tabulate at the required pressures. Therefore we ray trace forward from a set of tangent points on the full grid (with given pressures) and evaluate the forward model for these rays, rather than tracing from the satellite in a set of directions related to the detector array. The ray trace will provide an angle of incidence at the satellite, so that a quadrature over the field of view of each detector can be carried out.

The use of a pressure grid involves an extra complication, because ray tracing is essentially a geometric procedure, best carried out in height coordinates, while the state vector is defined in pressure coordinates. In the case when horizontal homogeneity is assumed, the approach is relatively straightforward, following the principles of the method used in Kneizys *et al.* (1983). The quantities required from the ray trace are the angle of the ray at the satellite, and the pressure as a function of distance along the ray, so that path integrals such as  $\int q p ds$ ,  $\int q p P ds$ , and  $\int p T ds$  can be evaluated for each layer.

Figure A - 2: Propagation of a refracted ray through the limb



First we use the hydrostatic equation to obtain the heights  $z_k$  of the pressure levels for the full grid. These will not be equally spaced in height. We then trace a ray from each  $z_k$  as tangent height to the altitude of the satellite, relative to the center of curvature of the geoid. See Figure A-2 to define the terminology. For the refracted ray in the horizontally homogeneous case, the zenith angle of the ray at any altitude can be obtained from Snell's law:

$$n(r)r \sin\theta(r) = r_m \quad (\text{A.2.15})$$

where  $r = z + R_c$  and  $r_g = n(r)r_t = R_{cs} \sin\theta_s$ , is a constant for the ray, the geometric tangent radius or the *impact parameter*. Using

$$dr = \cos\theta \, ds \quad (\text{A.2.16})$$

we obtain

$$ds = (1 - r_g^2/n^2 r^2)^{-1/2} dr \quad (\text{A.2.17})$$

which cannot easily be integrated numerically to obtain  $s(r)$  because of the singularity at the tangent point. However by changing the variable of integration from  $r$  to  $x = r \cos \theta$  we can obtain

$$ds = dx/[1 - \gamma(r) \sin^2 \theta(r)] \quad (\text{A.2.18})$$

where  $\gamma = -(r/n) \partial n / \partial r$ , a positive quantity, is an explicit function of  $r$ , as is  $\sin \theta$ . The coordinate  $x$  has the property that in the absence of refraction,  $x = s$ . To integrated over each full grid layer, we choose a set of quadrature points  $x_l$  within the layer, and use e.g. the trapezium rule:

$$\Delta s = \sum_i (x_i - x_{i-1}) (1/(1 - \gamma_i \sin^2 \theta_i) + 1/(1 - \gamma_{i-1} \sin^2 \theta_{i-1}))/2 \quad (\text{A.2.19})$$

or some higher order integration rule. Note that it is not straightforward to find the altitudes of a set of points equally spaced in  $x$  because  $x^2 = r^2 - r_g^2/n^2(r)$  cannot be explicitly inverted to give  $r(x)$ , even though  $x$  can be evaluated at any given value of  $r$ . Either  $r^2(x) = x^2 + r_g^2/n^2(r)$  must be evaluated iteratively, or points chosen in  $r^2$  to make them approximately evenly spaced in  $x$ .

The refractive index of air is given in section A3.3.1.1.8 as an experimentally fitted function of pressure, temperature and water vapor. However it is close to being of the form  $n = 1 + \alpha p(r)$ , where  $\alpha$  is a constant, so that within each narrow layer, such as the full grid layer, it may be reasonably fitted to the form

$$n = 1 + \alpha p_0 \exp(-r/H_n) \quad (\text{A.2.20})$$

so that we can write

$$\partial n / \partial r = -(n - 1)/H_n \quad (\text{A.2.21})$$

where  $H_n$  is the scale height of refractivity,  $n-1$ , within the layer.

#### A3.3.1.1.5 Path Integrals for the Limb Case

The absorber amount of molecule  $m$  in a sublayer,  $\Delta u_m = \int q_m \rho \, ds$  can be evaluated in the same way as  $\Delta s$  by integrating with respect to  $x$  using the trapezium (or other) rule:

$$\Delta u_m = \sum_i (x_i - x_{i-1}) (q_{im} \rho_i / (1 - \gamma_i \sin^2 \theta_i) + q_{m,i-1} \rho_{i-1} / (1 - \gamma_{i-1} \sin^2 \theta_{i-1}))/2 \quad (\text{A.2.22})$$

The effective pressure for a full grid layer is defined by

$$\bar{P} = \int \rho P \, ds / \int \rho \, ds \quad (\text{A.2.23})$$

where the two integrals are evaluated as sums over sublayers within the full grid layer, the elements of the sums being

$$\int \rho P \, ds = \Delta(uP) = \sum_i (x_i - x_{i-1}) (P_i \rho_i / (1 - \gamma_i \sin^2 \theta_i) + P_{i-1} \rho_{i-1} / (1 - \gamma_{i-1} \sin^2 \theta_{i-1}))/2 \quad (\text{A.2.24})$$

and

$$\int \rho \, ds = \Delta u = \sum_i (x_i - x_{i-1}) (\rho_i / (1 - \gamma_i \sin^2 \theta_i) + \rho_{i-1} / (1 - \gamma_{i-1} \sin^2 \theta_{i-1}))/2 \quad (\text{A.2.25})$$

The integral over the lowest sublayers (close to the tangent point) should be evaluated using a quadratic rule.

The effective temperature for a full grid layer is defined by

$$\bar{T} = \int \rho T \, ds / \int \rho \, ds \quad (\text{A.2.26})$$

in a similar way to the effective pressure. The elements of the sum for the numerator are

$$\Delta(uT) = \sum_i (x_i - x_{i-1}) (T_i \rho_i / (1 - \gamma_i \sin^2 \theta_i) + T_{i-1} \rho_{i-1} / (1 - \gamma_{i-1} \sin^2 \theta_{i-1})) / 2 \quad (\text{A.2.27})$$

Again, the integral over the lowest sublayers should be evaluated using a quadratic rule.

#### *A3.3.1.1.6 Ray tracing in the Inhomogeneous Limb Case.*

It is marginal whether the change in the refracted path due to horizontal inhomogeneities is significant. In the worst case, the slope of a pressure surface of 0.001, corresponding to a geostrophic wind of  $100 \, \text{m s}^{-1}$ , gives an error in tangent height at mid troposphere of order 40 m, or about 0.5% in pressure or density. Nevertheless we give the following analysis to describe a possible approach, should it be needed on further investigation.

In the general case the refraction equations do not have an explicit solution expressible as integrals, unlike the horizontally homogeneous case. A set of coupled ordinary differential equations can be derived, relating  $r(s)$ ,  $\theta(s)$  and  $\psi(s)$ :

$$d(\theta + \psi)/ds = -\sin\theta / n (\partial n / \partial r)_\psi + (\cos\theta / rn)(\partial n / \partial \psi)_r \quad (\text{A.2.28})$$

$$dr/ds = \cos\theta \quad (\text{A.2.29})$$

$$d\psi/ds = \sin\theta / r \quad (\text{A.2.30})$$

where  $\psi$  is the angle at the center of curvature relative to the instrument. The first equation states that the curvature of the ray is equal to the fractional gradient of the refractive index normal to the ray. The others are simple geometry. We can use (A.2.28) and (A.2.30) to obtain:

$$d\theta/ds = -\sin\theta [1/r + 1/n (\partial n / \partial r)_\psi] + (\cos\theta / rn)(\partial n / \partial \psi)_r \quad (\text{A.2.31})$$

Equations (A.2.29), (A.2.30) and (A.2.31) can be integrated by any standard differential equation solver such as Runge-Kutta to give  $r(s)$ ,  $\theta(s)$  and  $\psi(s)$ .

The boundary conditions cause difficulties, however. A single ray must pass through the instrument at a known location, and have a tangent point at a given pressure level:

- (i) at  $s = 0$ ,  $\psi(0) = 0$  and  $r(0) = R_{cs}$
- (ii) at  $r = r(\zeta_i)$ ,  $\cot\theta = - (1/r)(\partial r / \partial \psi)_\zeta$ , i.e the slope of pressure surface  $\zeta_i$

where  $\zeta = -\ln(P/P_0)$ . Here I have put the origins of  $\psi$  and  $s$  at the instrument for convenience. We do not know before the ray trace where  $\psi$  of the tangent point is relative to the satellite. (This does not matter in the case of the horizontally homogeneous atmosphere.) Therefore we must solve the problem iteratively by either:

- (a) finding the value of  $\psi$  at the tangent point for which the ray passes through the instrument, or
- (b) finding the scan angle  $\theta_s$  at the satellite which gives a tangent point at the right pressure level

To locate the tangent point relative to the satellite, it is most convenient to locate the origin of  $s$  at the tangent point and the origin of  $\psi$  at the instrument. The initial conditions are, at the tangent point

$$(i) \ s = 0 \quad (ii) \ r = r_t \quad (iii) \ \psi = \psi_t \quad (iv) \ \cot\theta = - (1/r)(\partial r / \partial \psi)_\zeta.$$

Integrate forward from the tangent point until the ray reaches satellite altitude  $R_{cs}$ . The ray will miss the instrument by an amount  $\psi(R_{cs})$ . This quantity is then subtracted from  $\psi_t$  for the next iteration. If there were no line of sight gradients, we would need to go no further, but one more iteration will probably be necessary for convergence.

The temperature, water and (hence) the refractive index are specified vertically on the full grid, and horizontally at some set of values of  $\psi$ . Use the hydrostatic equation to find  $r$  on this same grid. Then the table can be used to find the partial derivatives  $(\partial n / \partial r)_\psi$ ,  $(\partial n / \partial \psi)_r$  and  $(\partial r / \partial \psi)_\zeta$  where they are required.

There is the extra complication that we want to find quadrature points along the rays lying on the full grid. We are at liberty to choose the quadrature points for the integration so we will change them as we iterate so that a subset ends up lying on the pressure grid. The suggested process is as follows, for each full grid level within the range seen by the instrument:

Repeat:

- Select a set of quadrature points in  $s$ :
- First time round, use  $s = ih$ ,  $i=0,1..$  for some constant spacing  $h$ .
- Subsequent times we will have a reasonable guess at the ray path, so use the tangent point, plus points where the ray intersects the full grid (inverse interpolate in  $\zeta(s)$ ), subdividing sections so that no interval is longer than  $h$ .
- Adjust the initial condition  $\psi_t$
- Integrate forward & backward through the atmosphere to give  $r(s)$ ,  $\theta(s)$  and  $\psi(s)$ .
  - Use a straight line ray from just outside the atmosphere where  $n=1$  to the satellite altitude to calculate the angle  $\psi_s$  by which the ray misses the instrument
  - Evaluate  $\zeta(s)$  at each quadrature point (use  $r$ ,  $\psi$  to interpolate in the 2-D profile table). until converged (fixed number of times, probably 3 or 4)

Carry out the path integrals using the same quadrature points and e.g. Simpsons rule.

The fixed number of iterations is required so that we safely can do a numerical perturbation of the ray trace for the Jacobian calculation.

A reasonable initial value for  $\psi_i$  can be obtained by starting with the highest tangent point required, initialized with the geometric (unrefracted) value, and work downwards, each time using the final value for the previous level as the initial value for the current level.

We should probably check for pathological circumstances such as the ray being refracted below the tangent level, by at least checking whether  $r < r_i$ ! This applies to the homogeneous case too.

The alternative approach of finding the scan angle  $\theta_s$  at the satellite which gives a tangent point at the right pressure level turns out to be more complicated, and not worth pursuing:

#### *A3.3.1.1.7 The gas equation for air*

The gas equation for air is given by Ciddor [1996] as

$$\rho = \frac{M_{dry}}{R^*T} P \cdot \frac{\left[ 1 - X_{H_2O} \left( 1 - \frac{M_{H_2O}}{M_{dry}} \right) \right]}{Y}, \quad (A2.32)$$

where  $R^* = 8.31451 \text{ J mole}^{-1} \text{ K}^{-1}$ , the universal gas constant;

$$M_{dry} = [28.9635 + 12.011 \cdot 10^{-6} (X_{CO_2} - 400)] \cdot 10^{-3} \text{ kg/mole};$$

$$X_{CO_2} = 1.5202 \cdot q_{CO_2};$$

$$M_{H_2O} = 0.018015 \text{ kg/mole};$$

$$X_{H_2O} = 0.6223 \cdot q_{H_2O}; \text{ and}$$

the compressibility factor  $Y$  is given by

$$Y = 1 - (P/T)[a_0 + a_1 t + a_2 t^2 + (b_0 + b_1 t)X_{H_2O} + (c_0 + c_1 t)X_{H_2O}^2] + (P/T)^2(d + eX_{H_2O}^2)$$

where

$$a_0 = 1.58123e^{-6}$$

$$a_1 = 2.9331e^{-8}$$

$$a_2 = 1.1043e^{-10}$$

$$b_0 = 5.707e^{-6}$$

$$b_1 = 2.051e^{-8}$$

$$c_0 = 1.9898e^{-4}$$

$$c_1 = 2.376e^{-6}$$

$$d = 1.83e^{-11}$$

$$e = -0.765e^{-8}$$

$$\text{and } t = T - 273.15$$

#### A3.3.1.1.8 Refractive index of air

The index of refraction of air ( $n$ ) depends on frequency ( $\nu$ ), pressure ( $P$ ), temperature ( $T$ ) and water vapor amount (partial pressure  $P_{H_2O}$ ). Since the original Edlén equation was published in the early 1960's [Edlén, 1966], many revised empirical formulas have been published based on the new measurements. We use a revision of Edlén by Birch and Downs [1993 and 1994]:

$$\begin{aligned} n &= n_{tp} - f \cdot (a_9 - a_{10} \nu^2) \cdot 10^{-10}; \\ n_{tp} - 1 &= \frac{P(n_s - 1)}{a_5} \cdot \frac{[1 + 10^{-8}(a_6 - a_7 t)P]}{(1 + a_8 t)}; \text{and} \\ (n_s - 1) \cdot 10^{-8} &= a_0 + a_1 \cdot (a_2 - \nu^2)^{-1} + a_3 (a_4 - \nu^2)^{-1}; \end{aligned} \quad (A2.33)$$

where  $a_0$  to  $a_{10}$  are constants ( $a_0 = 8342.54$ ;  $a_1 = 2406147.0$ ;  $a_2 = 130.0$ ;  $a_3 = 15998.0$ ;  $a_4 = 38.9$ ;  $a_5 = 96095.43$ ;  $a_6 = 0.601$ ;  $a_7 = 0.00972$ ;  $a_8 = 0.003661$ ;  $a_9 = 3.7345$ ;  $a_{10} = 0.0401$ ; ),  $\nu$  is frequency in  $\text{mm}^{-1}$ ,  $P$  is pressure in Pa,  $t$  is temperature in  $^{\circ}\text{C}$  ( $t = T - 273.15$ ), and  $f$  is the partial pressure of water vapor.

Although the above formula was derived from measurements of visible and near infrared region, other measurements suggest that it could be extrapolated to the infrared region [Coleman *et al.*, U.S. NBS, "Table of Wavenumbers", 1960]. Note that frequency ( $\nu$ ) only has a secondary effect on  $n$ , so that the ray-trace step simply uses the averaged frequency for the forward model spectrum range in the calculation.

### A3.3.1.5: Non-LTE

The single-line volumetric absorption  $\kappa_v$  and local thermal radiance  $R_v$  is given by

$$\kappa_v = \frac{h\nu}{4} \bar{B} (g_u n_l - g_l n_u) \phi_v \quad (\text{A3.1})$$

and

$$R_v = \frac{h^2 \nu^4}{2\pi c^2} g_l n_u \chi_v, \quad (\text{A3.2})$$

where

$$\chi_v = \phi_v e^{-h(\nu - \nu_o)/kT}, \quad (\text{A3.3})$$

where  $n_l$  and  $n_u$  are the number density populations of the lower and upper V-R states and the constant integers  $g_l$  and  $g_u$ , are the respective single state degeneracy factors.

This result is a general one for a two-level system. The lineshapes,  $\chi_v$  and  $\phi_v$ , are functions of the bulk thermodynamic quantities such as pressure, temperature, plus individual gas densities which can separately influence the far wing lineshapes. The populations are given by the Boltzman distribution only under conditions of local thermodynamic equilibrium. In the presence of a strong radiation field, or under conditions for which the relaxation rates are slow with respect to physical processes influencing the state populations, the upper and lower state populations are not simply related through Boltzmann factors associated with a characteristic temperature for the system and the source function for the radiance is no longer given by the Planck function.

In the present case for TES observations, several assumptions can be made which significantly simplify the Non-LTE problem: (1) the relevant transitions occur at low pressure so that the Doppler shape is dominant with the line shape for emission and absorption being the same; (2) the system is in translational equilibrium with a characteristic kinetic temperature (affects only the Doppler width); and (3) the system is in rotational equilibrium with a characteristic rotational temperature. In the present formulation, the Non-LTE radiative transfer is developed as an extension of the LTE radiative transfer minimizing complexity and computational cost. The Non-LTE vibrational state population variables can be used to relate the Non-LTE single-line absorption and radiance to the same quantities calculated for an atmosphere in equilibrium at the characteristic temperature  $\bar{T}$ . The relationship between non-equilibrium and equilibrium radiative properties for a single line can be summarized by

$$\kappa_v = \left[ \frac{g_u n_l - g_l n_u}{g_u n_l^e - g_l n_u^e} \right] \kappa_v^e \quad (\text{A3.3})$$

and

$$R_v = \frac{n_u}{n_u^e} R_v^e, \quad (\text{A3.4})$$

which can also be written in terms of the Planck function as



$$R_v = \frac{n_u}{n_u^e} B_v(\bar{T}) K_v^e. \quad (\text{A3.5})$$

The superscript  $e$  denotes the equilibrium values of the respective quantities.

The ratios of non-LTE vibrational populations to their equilibrium values are given as enhancement (or depletion) ratios,

$$r_l = \frac{n_l}{n_l^e} \quad \text{and} \quad r_u = \frac{n_u}{n_u^e}. \quad (\text{A3.6})$$

The single-line contributions to  $K_v$  and  $C_v$  due to a transition with wavenumber value  $\nu_o$  can be expressed simply in terms of these ratios according to

$$K_v = \left[ \frac{r_l - r_u \Delta}{1 - \Delta} \right] K_v^e \quad (\text{A3.7})$$

and

$$C_v = \left[ \frac{r_l - r_u}{1 - \Delta} \right] K_v^e \quad (\text{A3.8})$$

where  $\Delta$  is the Boltzman factor,

$$\Delta = \frac{g_l n_u^e}{g_u n_l^e} = e^{-h\nu_o/k\bar{T}}. \quad (\text{A3.9})$$

The factors in brackets can be viewed as Non-LTE line strength correction factors. The functions,  $K_v$  and  $C_v$ , are obtained from the equilibrium values of the spectral absorption coefficients tabulated for individual vibrational states of a given molecular species. The quantities required for the calculation are  $r_l$ ,  $r_u$  and  $\nu_o$  for each Non-LTE vibrational state.

The complete solution of the radiative transfer equation for a homogeneous path is given by

$$L_v = L_v^o e^{-K_v u} + B_v(\bar{T}) \left[ 1 - \frac{C_v}{K_v} \right] [1 - e^{-K_v u}] \quad (\text{A3.10})$$

where  $L_v^o$  is the radiation at the path boundary. The effect of solving the non-equilibrium problem for a homogeneous layer is effectively to modify the line strengths (equilibrium absorption coefficients) contributing to the local absorption coefficient  $K_v$ , and to replace the Planck function  $B_v$  by the high resolution function  $B_v(\bar{T}) [1 - C_v / K_v]$ .

### A3.3.2.2: Map of Earth Surface Composition

#### Global Land Cover Characteristics Data Base

This appendix describes an existing source of global land cover maps with 1 km resolution and a choice of land classification schemes. This database was generated by the U.S. Geological Survey (USGS) Earth Resources Observation System (EROS) Data Center, the University of Nebraska-Lincoln (UNL) and the Joint Research Centre of the European Commission and is described in more detail at: <http://edcwww.cr.usgs.gov/landdaac/glcc/glcc.html>. Their maps are derived primarily from 1 km resolution composites of normalized difference vegetation index (NDVI) data from the Advanced Very High Resolution Radiometer (AVHRR) for the 12 month period of April 1992-March 1993. (NDVI values are the difference divided by the sum of the near infrared (channel 2) and visible (channel 1) reflectance values, after calibration and atmospheric corrections). The strategy for global land cover characterization is given in Loveland *et al* [1991, 1995] and Brown *et al* [1993] and an AVHRR data quality evaluation is described in Zhu and Yang [1996]. The global land cover maps are available in 6 different classification schemes with a range of 10 to 94 land cover types. These schemes are optimized to provide relevant information for research in areas such as atmospheric general circulation models and land use studies. Three of these classification schemes include urban/built-up areas as a land cover type, a useful distinction for our purposes. These are the Global Ecosystems classification (94 classes), Olson [1994 a&b]; the USGS Land Use/Land Cover System (24 classes), Anderson *et al* [1976]; and the International Geosphere Biosphere Programme (IGBP) Land Cover Classification (17 classes), Belward [1996]. Although we should not preclude the use of the more detailed Global Ecosystems classification, the USGS Land Use/Land Cover system (listed below) has been chosen for the initial algorithm development. The IGBP scheme, although simpler, was not chosen because there were no classes to distinguish moist vs. dry vegetation, an important distinction because of significant spectral IR reflectance differences. None of the land cover classifications in this database distinguished ice from snow, and an additional database may be needed for these areas.

**Table A - 1: USGS Land Use/Land Cover System Legend (Modified Level 2)**

<b>Value</b>	<b>Code</b>	<b>Description</b>
1	100	Urban and Built-Up Land
2	211	Dryland Cropland and Pasture
3	212	Irrigated Cropland and Pasture
4	213	Mixed Dryland/Irrigated Cropland and Pasture
5	280	Cropland/Grassland Mosaic
6	290	Cropland/Woodland Mosaic
7	311	Grassland
8	321	Shrubland
9	330	Mixed Shrubland/Grassland
10	332	Savanna
11	411	Deciduous Broadleaf Forest
12	412	Deciduous Needleleaf Forest
13	421	Evergreen Broadleaf Forest
14	422	Evergreen Needleleaf Forest
15	430	Mixed Forest
16	500	Water Bodies
17	620	Herbaceous Wetland
18	610	Wooded Wetland
19	770	Barren or Sparsely Vegetated
20	820	Herbaceous Tundra
21	810	Wooded Tundra
22	850	Mixed Tundra
23	830	Bare Ground Tundra
24	900	Snow or Ice

### A3.4: Jacobians

The radiance at the satellite in terms of component contributions from the atmosphere and the surface, but neglecting the solar contribution, may be written as,

$$L_{sat} = L_L^\uparrow + \left[ \varepsilon B(T_{sfc}) + \alpha L_0^\downarrow \right] T_{0,L} \quad (A4.1)$$

in which  $L_L^\uparrow$  is the upwelling radiance contribution of the atmosphere from the surface to the level at the top of the atmosphere (TOA),  $T_{0,L}$  is the transmittance of the atmosphere and  $L_0^\downarrow$  is the downwelling radiance at the surface. For a specularly reflecting surface,  $L_0^\downarrow$  is calculated for the same zenith angle as  $L_L^\uparrow$  and  $\alpha$  is the appropriate bidirectional reflectance. For a Lambertian surface,  $L_0^\downarrow$  is calculated at the diffusivity angle, the downwelling radiation scattered by the surface is taken to be isotropic and  $\alpha$  is the albedo.

Due to the form of the radiative transfer equation, the analytic derivative of the radiance at the satellite with respect to a change in parameter  $x_l$  at level  $l$ , is most expeditiously obtained in terms of associated layer quantities, so that we have

$$\frac{\partial L_{sat}}{\partial x_l} = \sum_j \frac{\partial L_{sat}}{\partial \bar{x}_j} \frac{\partial \bar{x}_j}{\partial x_l} \quad (A4.2)$$

in which  $x_l$  is an element of the retrieval vector associated with level  $l$  and  $\bar{x}_j$  is the associated layer quantity for layer  $j$ . Note that in general,  $x$  may be mixing ratio (log mixing ratio) or temperature in this context.

In this section we focus on the computation of  $\frac{\partial L_{sat}}{\partial \bar{x}_j}$ , noting that  $\frac{\partial \bar{x}_j}{\partial x_l}$  is independent of wavenumber. Differentiating Eq. A4.1 with respect to  $\bar{x}_j$  we obtain

$$\frac{\partial L_{sat}}{\partial \bar{x}_j} = \frac{\partial L_L^\uparrow}{\partial \bar{x}_j} + \varepsilon B(T_{sfc}) \frac{\partial T_{0,L}}{\partial \bar{x}_j} + \alpha \frac{\partial L_0^\downarrow}{\partial \bar{x}_j} T_{0,L} + \alpha L_0^\downarrow \frac{\partial T_{0,L}}{\partial \bar{x}_j} \quad (A4.3)$$

$$= \frac{\partial L_L^\uparrow}{\partial \bar{x}_j} + \alpha T_{0,L} \frac{\partial L_0^\downarrow}{\partial \bar{x}_j} + \left[ \varepsilon B(T_{sfc}) + \alpha L_0^\downarrow \right] \frac{\partial T_{0,L}}{\partial \bar{x}_j} \quad (A4.4)$$

It will prove useful to consider the partial derivative of the total transmittance with respect to the layer optical depth,  $\frac{\partial T_{0,L}}{\partial \tau_j}$ , which can be written as

$$\frac{\partial T_{0,L}}{\partial \tau_j} = \frac{\partial \{T_{1,L} T_{j,L} T_L\}}{\partial T_j} \quad (\text{A4.5})$$

$$= \frac{\partial \{\exp(-\tau_1)_L \exp(-\tau_j)_L \exp(-\tau_L)\}}{\partial T_j} \quad (\text{A4.6})$$

$$= \{\exp(-\tau_1)_L [-\exp(-\tau_j)]_L \exp(-\tau_L)\} \quad (\text{A4.7})$$

$$= -T_{0,L} \quad (\text{A4.8})$$

Thus we have the simple result that the partial derivative of the total transmittance with respect to the optical depth in any layer is the negative of the total transmittance.

We proceed next to consider the partial derivative of the total transmittance with respect to layer mixing ratios,

$$\frac{\partial T_{0,L}}{\partial \bar{q}_{l,m}} = \frac{\partial T_{0,L}}{\partial \tau_l} \frac{\partial \tau_l}{\partial \bar{q}_{l,m}} \quad (\text{A4.9})$$

where  $\bar{q}_l$  is the layer mean mixing ratio for molecule  $m$  in layer  $l$ . The optical depth can be written as follows

$$\tau_l(\bar{T}_l) = \sum_m u_{l,m} \kappa_{l,m}(\bar{T}_l) + u_{l,1} \left\{ C_f(\bar{T}_l) \left( \frac{\bar{\rho}_{l,dry}}{\rho_0} \right) + C_s(\bar{T}_l) \left( \frac{\bar{\rho}_{l,1}}{\rho_0} \right) \right\} \quad (\text{A4.10})$$

where  $\bar{T}_l$  is the layer mean temperature,  $\kappa_{l,m}$  is the absorption coefficient for molecule  $m$  and  $u_m$  is the integrated path amount for molecule  $m$ . For the purposes of this derivation, the air broadened continua contributions are considered as included in  $\kappa_{l,m}$ . The self broadened water vapor continuum contribution is given explicitly in terms of the continuum coefficient  $C_s(\bar{T}_l)$  with  $\bar{\rho}_{l,1}$  the number density of water vapor in layer  $l$  and  $\rho_0$  the reference number density with  $P_0 = 1$  atm and  $T_0 = 296$  K. Eq. A4.10 may be written in terms of layer mixing ratio as

$$\tau_l(T_l) = u_l \left\{ \sum_m \bar{q}_{l,m} \kappa_{l,m}(\bar{T}_l) + C_f(\bar{T}_l) (1 - \bar{q}_{l,1}) \left( \frac{\bar{\rho}_l}{\rho_0} \right) + C_s(\bar{T}_l) \bar{q}_{l,1} \left( \frac{\bar{\rho}_l}{\rho_0} \right) \right\} \quad (\text{A4.11.1})$$

$$= u_l \left\{ \sum_m \bar{q}_{l,m} \kappa_{l,m}(\bar{T}_l) + \bar{q}_{l,1} \left( \frac{\bar{\rho}_l}{\rho_0} \right) \left[ C_f(\bar{T}_l) + \bar{q}_{l,1} [C_s(\bar{T}_l) - C_f(\bar{T}_l)] \right] \right\} \quad (\text{A4.11.2})$$

$$= u_l \bar{K}_l \quad (\text{A4.12})$$

where  $\bar{\rho}_l$  is now the mean number density for the layer and  $u_l$  is the integrated path amount for dry air in the layer. The effective absorption coefficient,  $\bar{\kappa}_l$ , will be prove useful in the subsequent development. From Eq. A4.9, the partial derivative of the total transmittance with respect to layer mixing ratio in layer  $l$  can now be obtained as

$$\left. \frac{\partial T_{0,L}}{\partial \bar{q}_{l,m}} \right|_{m \neq 1} = -T_{0,L} \{u_l \kappa_{l,m}(\bar{T}_l)\} \quad (\text{A4.13.1})$$

and

$$\frac{\partial T_{0,L}}{\partial \bar{q}_{l,1}} = -T_{0,L} \left\{ u_l \left[ \kappa_{l,1}(\bar{T}_l) + 2\bar{q}_{l,1} C_s(\bar{T}_l) \left( \frac{\bar{\rho}_l}{\rho_0} \right) \right] + \frac{\partial u_l}{\partial \bar{q}_{l,1}} \bar{\kappa}_l \right\} \quad (\text{A4.13.2})$$

In this derivation the explicit dependence of the self-continuum due to water vapor has been included because of its large contribution to the radiance in the boundary layer and lower troposphere. The layer pressure boundaries are assumed constant for these derivatives with the implicit constraint that the mass in the layer be constant and thus the column of dry air must increase as the mixing ratio of water vapor in the layer is increased, the second term in Eq. A4.13.2. The change in the dry air column due to changes in mixing ratios of the other species being retrieved is negligible. The magnitude of this term should be assessed to establish whether implementation is necessary in the computation of the derivatives. The dependence of the optical depth on the self broadened line width of water vapor has not been included in the calculation of the derivative since its contribution to the radiance, though non-negligible, is small enough to neglect for present purposes. Eq. A4.13 thus provides the result for the last term in Eq. A4.4. Note that this expression is simple and contains terms that have been obtained in the course of the radiance calculation.

We now consider this same term for the case in which the elements of the retrieval vector are temperature,  $\frac{\partial T_{0,L}}{\partial \bar{T}_l}$ . We have from Eq. A4.9,

$$\frac{\partial T_{0,L}}{\partial \bar{T}_l} = \sum_{l'} \frac{\partial T_{0,L}}{\partial \tau_{l'}} \frac{\partial \tau_{l'}}{\partial \bar{T}_l} \quad (\text{A4.14})$$

$$= -T_{0,L} \left\{ \left. \frac{\partial \tau_l}{\partial \bar{T}_l} \right|_{u_l} + \sum_{l'} \bar{\kappa}_{l'} \frac{\partial u_{l'}}{\partial \bar{T}_l} \right\} \quad (\text{A4.15})$$

The first term in Eq. A4.15 is straightforward to implement for the case in which the absorption coefficients are tabulated as a function of temperature and is very efficient. In the current version of TWPR, three point Lagrange interpolation is used to obtain the optical depths at the specified layer temperature. The analytic derivative for this term is readily obtained from the interpolation expression. This result is one of the principal reasons for utilizing absorption

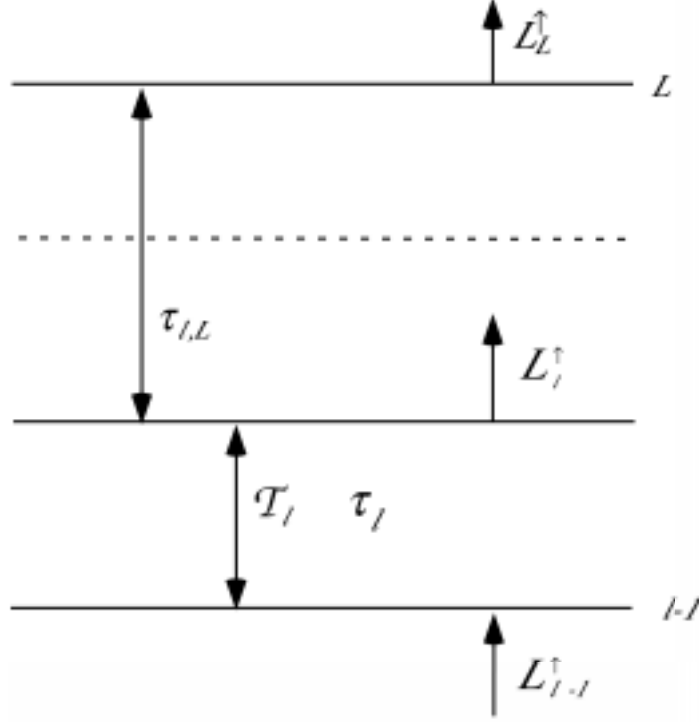
coefficient tables. The second term in Eq. A4.15 arises in the calculation of the integrated path amounts along the refracted path for the limb case. The layer mixing ratios are assumed to be constant for present purposes, a premise that needs to be confirmed. With some added complication, the effect of the variation of the column amounts with temperature can be included in the calculation of the optical depth at the three temperatures, facilitating the implementation of this contribution to the temperature derivative.

It should be noted that there are implications in this approach for the algorithms employed. For this case, it is desirable in calculating the radiative transfer, to obtain the spectral optical depths at the three appropriate temperatures and then to perform the interpolation to the layer temperature rather than interpolating the absorption coefficients to the layer temperature. For the partials with respect to mixing ratio, however, the absorption coefficients of the relevant species at the layer temperature are required (Eq. A4.13). Considerable acceleration can be achieved in this regard if derivatives with respect to temperature and mixing ratio are not required simultaneously. In general, this is not always possible nor necessarily desirable, but it does lead to computational saving. In addition, the algorithm should be developed to avoid computation of derivative components when they are small: when  $T_{0,L}$  is small or for water vapor in certain spectral regions above a given altitude.

We now consider the other terms in Eq. A4.4. In considering the partial derivatives of the up and downwelling atmospheric radiance with respect to layer quantities, we adopt an algorithmic perspective to simplify the development and facilitate implementation. We utilize a simplified form of the radiative transfer equation ignoring the ‘linear in  $\tau$ ’ dependence on the Planck function. The contribution from this term is not large and may readily be included at a subsequent stage in the implementation.

The first step is to start at the TOA and calculate the optical depths ( $\tau_l$ ), layer transmittances ( $T_l$ ) and total transmittance to each atmospheric level ( $T_{l,L}$ ) in accordance with the following figure (Figure A-3) where and  $T_{l-1,L}$  is obtained from  $T_{l,L} \times T_l$  with  $T_{L-1,L} \equiv 1$ .

Figure A - 3: First Step in Jacobians



If at some level  $L_{\min}$ ,  $T_{L_{\min},L}$  is below a preset threshold, then  $L_{\min}$  becomes the lowest level that must be treated in the entire problem and the Eq. (A4.1) becomes

$$L_{sat} = L_L^{\uparrow} \quad (\text{A4.16})$$

so that the surface and the downwelling contributions may be ignored. If  $T_{l,L}$  does not go below the threshold, then  $L_{\min} = 0$  and all terms of Eq. A4.1 must be considered.

The second step in obtaining  $L_{sat}^{\uparrow}$  and the relevant derivatives is to consider the radiative transfer algorithm initialized at  $L_{\min}$  and proceeding to level  $L$ . The radiance at level  $l$  is given by

$$L_l^{\uparrow} = T_l L_{l-1}^{\uparrow} + B(\bar{T}_l)(1 - T_l) \quad (\text{A4.17})$$

with  $L_{L_{\min}}^{\uparrow} = 0$ .

At a given stage in the calculation we can write  $L_L^{\uparrow}$  as the sum of the two terms,

$$L_L^{\uparrow} = L_l^{\uparrow} T_{l,L} + L_{l,L}^{\uparrow} \quad (\text{A4.18})$$



in which  $L_{L,l}^\uparrow$  is the contribution to the radiance from layers above layer  $l$  (level  $l$ ). Substituting Eq. A4.17 into Eq. A4.18, we obtain

$$L_L^\uparrow = \left\{ T_l c + B(\bar{T}_l)(1 - T_l) \right\} T_{l,L} + L_{l,L}^\uparrow \quad (\text{A4.19})$$

It is important to note that  $L_{l-1}^\uparrow$  and  $L_{l,L}^\uparrow$  do not contain any dependence with respect to layer quantities associated with layer  $l$ . Thus, this form is particularly useful for the evaluation of the derivative with respect to the general layer quantity  $\bar{x}_l$ ,

$$\frac{\partial L_L^\uparrow}{\partial \bar{x}_l} = \left\{ \frac{\partial T_l}{\partial \bar{x}_l} L_{l-1}^\uparrow + \frac{\partial B(\bar{T}_l)}{\partial \bar{x}_l} (1 - T_l) - B(\bar{T}_l) \frac{\partial T_l}{\partial \bar{x}_l} \right\} T_{l,L} \quad (\text{A4.20})$$

This expression includes the effect of  $\bar{x}_l$  on attenuating the incoming radiation to the layer as well as on the radiance originating in the layer.

We next consider the case in which  $\bar{x}_l$  is the mixing ratio associated with molecule  $m$ . Taking advantage of the expressions previously derived we obtain

$$\frac{\partial L_L^\uparrow}{\partial \bar{x}_{l,m}} = \left\{ \frac{\partial T_l}{\partial \tau_l} \frac{\partial \tau_l}{\partial \bar{x}_{l,m}} \left[ L_{l-1}^\uparrow - B(\bar{T}_l) \right] \right\} T_{l,L} \quad (\text{A4.21})$$

$$= \left\{ \left[ B(\bar{T}_l) - L_{l-1}^\uparrow \right] T_l \frac{\partial \tau_l}{\partial \bar{x}_{l,m}} \right\} T_{l,L} \quad (\text{A4.22})$$

Note that all quantities required here have previously been calculated so that this contribution to the partial derivatives may be evaluated at each step in the algorithm. The partial derivative of optical depth with respect to mixing ratio may be obtained from the bracketed terms in Eqs. A4.13.1 and A4.13.2.

Next consider the derivative of  $L_L^\uparrow$  with respect to layer temperature,

$$\frac{\partial L_L^\uparrow}{\partial \bar{T}_l} = \left\{ \frac{\partial T_l}{\partial \bar{T}_l} L_{l-1}^\uparrow + \frac{\partial B(\bar{T}_l)}{\partial \bar{T}_l} (1 - T_l) - B(\bar{T}_l) \frac{\partial T_l}{\partial \bar{T}_l} \right\} T_{l,L} \quad (\text{A4.23})$$

$$= \left\{ \frac{\partial T}{\partial \tau_l} \frac{\partial \tau_l}{\partial \bar{T}_l} \left[ L_{l-1}^\uparrow - B(\bar{T}_l) \right] + \frac{\partial B(\bar{T}_l)}{\partial \bar{T}_l} (1 - T_l) \right\} T_{l,L} \quad (\text{A4.24})$$

$$= \left\{ \left[ B(\bar{T}_l) - L_{l-1}^\uparrow \right] T_l \frac{\partial \tau_l}{\partial \bar{T}_l} + \frac{\partial B(\bar{T}_l)}{\partial \bar{T}_l} (1 - T_l) \right\} T_{l,L} \quad (\text{A4.25})$$

Again, all terms are available, with the previous discussion of  $\frac{\partial \tau_l}{\partial \bar{T}_l}$  applicable in this case as well.

The derivative of the Planck function with respect to layer temperature is calculated and stored using a piecewise linear update as is used for the Planck function. Also note that many of the terms are just those required for the radiative transfer calculation itself, Eq. A4.3.17.

Finally consider the second term in Eq. A4.4 in which  $\frac{\partial L_0^\downarrow}{\partial \bar{x}_j}$  is required. Recall this term is only

necessary if  $L_{\min}=0$ . This case is essentially identical to that required for  $\frac{\partial L_L^\uparrow}{\partial \bar{x}_j}$  except that the direction is reversed. The transmittance from the surface to each successive level is required,  $T_{0,l}$ , readily obtained since the  $T_l$  have been saved. The radiance calculation is initiated at level  $L$  (TOA) and proceeds to level 0 (sfc). Note that the integrated path amounts and the layer transmittances may be different from those used for  $L_L^\uparrow$  depending on whether the surface is Lambertian or specular.

The extension of the present approach to the limb viewing case is straightforward. The emissivity,  $\epsilon$ , in the present formulation is set to zero and the albedo,  $\alpha$ , is set to unity. This approach enables the treatment of atmospheres that are asymmetric about the line of sight tangent point with minimal additional effort. A critical remaining task is the development of the partial derivatives of the layer quantities with respect to level quantities. This can be achieved by developing the necessary analytic derivatives where feasible. For variables for which this is difficult, the finite difference approach may be utilized. In the course of implementing the coding for the analytic derivatives, validation using the currently implemented finite difference method will be essential. In this development for the analytic derivatives, the solar contribution has been neglected for simplicity of exposition. Inclusion of this contribution is straightforward in the context of the present formulation. It should be emphasized that the derivation is most directly obtained for the variable associated with species profile taken as volume mixing ratio,  $\bar{q}_m$ . If another variable is preferred, e.g.,  $\log \bar{q}_m$ , this variable change can be made as part of the transformation from layer to level quantities. A final point with respect to the transformation from level quantities to layer quantities, is the fact that the transformation is not dependent on frequency. Consequently, this transformation may be performed after the spectral convolution is performed, providing a potential saving of time and providing an opportunity for increased flexibility in the retrieval vector definitions without significantly impacting computational cost.

### A3.3.8.1: Line Parameters: ABSCO Databases

#### H<sub>2</sub>O (molecule 1)

There are numerous, significant deficiencies in the currently available water vapor parameters in the thermal IR spectral region covered by TES. A major update to the positions, intensities, air-broadening coefficients, self-broadening coefficients, and pressure-induced shifts is in preparation (R. A. Toth, Jet Propulsion Laboratory, private communication, 1998).

As was done for the ATMOS compilation [Brown *et al.*, 1995], we plan to treat HDO and a separate molecular species because of the large fractionation effects of HDO with respect to H<sub>2</sub>O. The current database does not include the updated positions and intensities of the HD<sup>16</sup>O  $\nu_2$  band derived by Flaud *et al.* [1986] and the more recent  $\nu_2$  HD<sup>16</sup>O, HD<sup>17</sup>O, and HD<sup>18</sup>O position and intensity analysis results of Toth [1993]. The parameters of Flaud *et al.* [1986] have been regenerated (J.-M. Flaud, private communication) and are now available to the TES project with approximate air-broadened widths (C. P. Rinsland, private communication, 1998). Air-broadened pressure shifts are set to zero.

#### CO<sub>2</sub> (molecule 2)

A new global least-squares fit of the energy levels of carbon dioxide is performed for each edition of HITRAN to improve the accuracy [Rothman *et al.*, 1998]. In addition, absolute intensities are computed from an updated set for each edition. Recent studies not yet incorporated in the HITRAN global fit include the analysis of 1500 lines in 36 vibration-rotation bands of <sup>12</sup>C<sup>16</sup>O<sub>2</sub> between 3090 and 3850 cm<sup>-1</sup> [Malathy Devi *et al.*, 1998a]. The results were derived from room temperature 0.01- cm<sup>-1</sup> resolution laboratory spectra recorded at Kitt Peak. Although this spectral region will not be measured by TES, the line positions will improve the <sup>12</sup>CO<sub>2</sub> energy levels for future HITRAN updates. Recent developments in the infrared spectroscopy of CO<sub>2</sub> have been reviewed by Malathy Devi *et al.* [1996].

#### O<sub>3</sub> (molecule 3)

Updates for O<sub>3</sub> on the 1996 HITRAN compilation and updates not incorporated in the current edition of HITRAN have been summarized by Rinsland *et al.* [1998a]. There are several results of importance for TES studies.

Spectra of <sup>17</sup>O-enriched ozone samples have been recorded at 0.005-cm<sup>-1</sup> resolution and analyzed to derive the line positions and intensities for the  $\nu_1$  and  $\nu_3$  bands of <sup>16</sup>O<sup>17</sup>O<sup>16</sup>O [Heyart *et al.*, 1992] and <sup>16</sup>O<sup>16</sup>O<sup>17</sup>O [Heyart *et al.*, 1993]. As described by Rinsland *et al.* [1998a], these parameters, which are not included on HITRAN 1996 [Rothman *et al.*, 1998] have been used to identify isolated lines of the  $\nu_3$  bands of <sup>16</sup>O<sup>17</sup>O<sup>16</sup>O and <sup>16</sup>O<sup>16</sup>O<sup>17</sup>O in both high resolution ground-based and balloon-borne stratospheric solar absorption spectra. Hence, they may be detectable in TES spectra and will need to be included for accurate retrievals.

The first high-resolution analysis of the  $\nu_1 + \nu_3$  bands of <sup>16</sup>O<sup>16</sup>O<sup>18</sup>O and <sup>16</sup>O<sup>18</sup>O<sup>16</sup>O at 4.8  $\mu$ m was performed by Flaud *et al.* [1994]. On the basis of that work, isolated lines of both heavy isotopic

species have been identified in high resolution ground-based solar absorption spectra by Arlander *et al.* [1994] and Goldman *et al.* [1998] and in high resolution stratospheric solar occultation spectra by Goldman *et al.*<sup>41</sup> At the present time, the potential use of these lines for quantitative atmospheric studies has not been fully realized. The levels of the (101) vibrational upper state are perturbed by interactions with the nearby, unobserved rotational levels of the (002) and (200) states.<sup>39</sup> Positions and relative intensities computed for unperturbed lines have been used to identify suitable intervals for future quantitative <sup>18</sup>O-isotopic ozone atmospheric studies.<sup>41</sup>

Absolute intensities of 376 <sup>16</sup>O<sub>3</sub> lines in the 9-11  $\mu\text{m}$  region have been measured from room temperature spectra recorded at 0.0027-cm<sup>-1</sup> with the National Solar Observatory facility on Kitt Peak [Smith *et al.*, 1998]. The ozone samples were contained in a glass cell having crossed IR-transmitting and UV-transmitting paths approximately 10 cm in each direction. The ozone partial pressures were determined in the cell were determined from measurements of the 254-nm UV absorption using the absorption cross sections of Mauersberger *et al.* [1987] as the reference standard. A multispectrum nonlinear least-squares fitting technique was used to determine the intensities of 366 lines in the P, Q, and R branches of the  $\nu_3$  fundamental and 10 lines in the R branch of the  $\nu_1$  band. The absolute accuracies of the lines ranged from 2% for the strongest, most well-determined lines to 4 to 5% for the weakest lines measured. On average, the measured intensities are 1% larger than the values on the 1996 HITRAN list [Rothman *et al.*, 1998]. This result indicates that the intensity scale assumed for HITRAN O<sub>3</sub> at 10  $\mu\text{m}$  is sufficiently accurate for retrievals of O<sub>3</sub> from the TES observations.

### CO (molecule 5)

Self-broadening and self-shift coefficients have been measured recently in the fundamental band of <sup>12</sup>C<sup>16</sup>O [Malathy Devi *et al.*, 1998b]. The results were obtained by analyzing five 0.0027-cm<sup>-1</sup> resolution room temperature laboratory spectra simultaneously using a multispectrum nonlinear least-squares fitting technique. The self-broadening coefficients are lower than on HITRAN 1996 [Rothman *et al.*, 1998] whereas the self-shifts are different in the P and R branches at the same  $\text{cm}^{-1}\text{atm}^{-1}$  with values that range from +0.0005(1) to -0.0042(3) cm<sup>-1</sup>atm<sup>-1</sup> at 296 K. A laboratory study to measure the broadening and the shifts of CO in air at room and low temperatures is planned for the new future (M. A. H. Smith, private communication, 1998).

### CH<sub>4</sub> (molecule 6)

The ongoing work summarized in the CH<sub>4</sub> section of the HITRAN 1996 main paper (Rothman *et al.*, 1998) is essential for a number of TES objectives.

### NO<sub>2</sub> (molecule 10)

Perrin *et al.* [1998] have reviewed the status of NO<sub>2</sub> line parameters. Below is a summary of the important problems that are likely to affect TES retrievals based on that review and other recent studies.

The 3.4  $\mu\text{m}$  region corresponds to the  $\nu_1 + \nu_3$  band and the associated first hot band  $\nu_1 + \nu_2 + \nu_3 - \nu_2$ . Although 20 times weaker than the absorption in the 6.2  $\mu\text{m}$  region, the 3.4  $\mu\text{m}$  bands occur in a window region that can be measured in nadir spectra. Recently, a new analysis for positions and intensities has been performed from Fourier transform spectra [Mandin *et al.*, 1997]. The analysis took into account both the Coriolis interaction between the spin-rotation levels of the (101) vibrational state and those of (120) and the spin-rotation resonances within (101) and (120). Although the experimental intensities of the  $\nu_1 + \nu_3$  band lines are in good agreement with earlier work, the hot band lines are about 1.48 times lower than determined previously [Perrin *et al.*, 1982].

In HITRAN 1996 [Rothman *et al.*, 1998], the air-broadening coefficients are set to  $0.067 \text{ cm}^{-1} \text{ atm}^{-1}$  at 296 K for all lines, except for the 3.4  $\mu\text{m}$  region, where the air-broadening coefficients for all lines are set to  $0.063 \text{ cm}^{-1} \text{ atm}^{-1}$  at 296 K. However, as described below there is evidence for a need to update the HITRAN air-broadening values.

Dana *et al.* [1997] have reported self-,  $\text{N}_2$ -, and  $\text{O}_2$ -broadening coefficients of  $\text{NO}_2$  lines in the  $\nu_1 + \nu_3$  band at 3.4  $\mu\text{m}$ . The study found a slight rotational dependence of the broadening coefficients versus  $N''$ , whereas no significant dependence was observed versus  $K_a''$ . An empirical relation was derived to compute air-broadening coefficients at 296 K with an uncertainty of about "10% for values of  $N''$  and  $K_a''$  less than 40 and 10, respectively. The authors note that for typical lines used for atmospheric applications, the single value reported in the HITRAN database for all lines of all bands of  $\text{NO}_2$  can differ by more than 20% from the measured values [Dana *et al.*, 1997]. A preliminary analysis of unpublished spectra of the  $1600 \text{ cm}^{-1}$   $\text{NO}_2$  band indicates that the widths of these lines are also too small in the HITRAN linelists with tests indicating that the changes produce a 10% increase in the retrieved mixing ratio of  $\text{NO}_2$  at 25 km and little effect above 30 km [Sen *et al.*, 1998].

#### $\text{HNO}_3$ (molecule 12)

Recently, Perrin *et al.* [1998] have reanalyzed the  $\nu_8 + \nu_9$  band at  $1205 \text{ cm}^{-1}$  based on a  $0.003\text{-cm}^{-1}$  resolution laboratory spectrum recorded at the University of Denver. As in a recent analysis [Wang *et al.*, 1997], the Hamiltonian for fitting the line positions takes into account the  $\tilde{A}K''^2$  anharmonic resonance linking the rotational levels of the  $\nu_8=1, \nu_9=1$  "bright" vibrational state with those of the  $\nu_7=1, \nu_8=1$  "dark" vibrational state. However, in contrast to previous work,  $\nu_8 + \nu_9$  is noted to be a hybrid-type band with clearly identified B-type transitions among those of the strong A-type lines. The A- and B-type components of the transition moment operator of the  $\nu_8 + \nu_9$  band were determined through a least-squares fit of experimental line intensities measured from the spectrum. The new analysis extends the assignments for the  $\nu_8 + \nu_9$  band to maximum rotational quantum numbers of  $J=74$  and  $K_a=49$  as compared to a maximum  $J$  value of 57 [Wang *et al.*, 1997].

### C<sub>2</sub>H<sub>6</sub> (molecule 27)

Recently, assignments, improved positions, intensities, and air-broadening coefficients and their temperature dependence have been derived for the strong and sharp <sup>P</sup>Q<sub>3</sub> subbranch of the  $\nu_7$  band at 2976.8 cm<sup>-1</sup> [Pine and Stone; 1996; Rinsland *et al.*, 1998; Pine and Rinsland, 1998]. This strong and sharp feature is prominent in ground-based solar spectra [Rinsland *et al.*, 1987; Rinsland *et al.*, 1998] and nearly free of atmospheric interferences. The new results were obtained from analysis of Doppler-limited and sub-Doppler molecular beam laboratory spectra. It may be possible to measure this C<sub>2</sub>H<sub>6</sub> feature in the TES nadir view spectra.

### COF<sub>2</sub> (molecule 29)

Although located almost entirely in the stratosphere, COF<sub>2</sub> produces IR absorption features in the limb spectra with absorptions located primarily in the regions of the  $\nu_1$  (1944 cm<sup>-1</sup>),  $\nu_4$  (1243 cm<sup>-1</sup>), and  $\nu_6$  (774 cm<sup>-1</sup>) bands. Recently, D'Cunha *et al.* [1997] have reported an analysis of the  $\nu_1$  band region. The new analysis included the Fermi resonance with the  $2\nu_2$  state and Coriolis interaction with the  $2\nu_3 + \nu_6$  dark state. According to D'Cunha *et al.* [1997], the results are in very good agreement with the values in HITRAN [Rothman *et al.*, 1998], as described by Rinsland *et al.* [1992]. Hence, we do not anticipate the need for a further update to the COF<sub>2</sub> parameters at this time.

### Partition Functions

It is important to note that the partition functions supplied by HITRAN have several significant deficiencies as discussed by Goldman *et al.* [1998].

### A3.3.8.2: Cross-Section P-T Interpolation Program XSFINT

#### 1. P-T Point outside table of temperature-pressure values

In this case the "distance" away from every point in the table is calculated and compared to find the closest point. The distance calculation is based on linear distance formulas where the pressure is divided by 10 to give similar units in temperature and pressure.

#### 2. P-T Point inside table of temperature-pressure values

This program picks points based on temperature lines where all temperatures within 2 degrees are considered to be on the same temperature line. A temperature line could look like

Temperature	Pressure
216	50.6
214.1	70.8
215.8	100.0

A table of pressures on temperature lines is constructed from which to pick points. There are four basic cases in the interpolate point outside table of temperature values; four points around target; three points around target; two points around target. The new cross-section records interpolated from the above cases are all written to a new cross-section file. The user can also select the points and interpolation method by hand rather than letting the program select the points and interpolation method.

#### Four points around target

In this case 2 points on the temperature line before and after the target temperature are found where the points surround the target pressure.

216.6,70.5	217.1,90.2 (temp line after)
210.0,80.0 (target point)	
200.1,69.9	201.0,89.9 (temp line before)

The corner pressures must be within 10% of each other (216.6,70.5 with 200.1,69.9 & 217.1,90.2 with 201.0,89.9) or the tightest diagonal line is picked and the 2 point temperature interpolate is activated, otherwise the 4 point interpolate is activated.

#### Three points around target

In this case either the temperature line above or below the target contains only one point.

216.6,70.5	217.1,90.2 (temp line after)
210.0,80.0 (target point)	
200.1,69.9	(temp line before)

or

216.6,70.5    217.1,90.2 (temp line after)  
210.0,80.0 (target point)  
201.0,89.9    (temp line before)

If the target temperature is within 5 degrees of the temperature line with 2 points, then a 2 point pressure interpolate is activated between those two points. If the target temperature is not close enough to the temperature line with two points, then two points are chosen that create a diagonal (200.1,69.9 with 217.1,90.2 or 216.6,70.5 with 201.0,89.9) then the two point temperature interpolate is activated.

### **Two points around target**

In this case one point on the temperature line before and after the target are used. If both points are either greater or smaller in pressure that the target, then the closest in pressure is used as the new point. If one of the two points are within 4% in temperature and 15% in pressure of the target, then that point is used as new point. If both points are within the 4% and 15% then the closest in temperature is used. If none of the above special cases occur then the 2 point temperature interpolate is activated.

### **Two point Temperature Interpolate**

Two point temperature interpolate does a linear interpolate in temperature between the two pressure/temperature cross-section points for each point in the cross-sections.

### **Two point Pressure Interpolate**

Two point pressure interpolate does a log interpolate in pressure between the two pressure/temperature cross-section points for each point in the cross-sections. (Note In the code the two point pressure interpolate is noted as a 3 point interpolate since two point temperature interpolate is noted as a 2 point interpolate)

### **Four point Interpolate**

Four point interpolate does a linear interpolate in temperature between the side pressure/temperature cross-section points, then a log interpolate in pressure between the two new temperature points resulting from the linear temperature interpolate.

### **XSFINT Source Code**

Xsfint has been compiled and tested on roma in /home/goldman/xsctions/interp. The source code for xsfint is all in one FORTRAN90 file called xsfint.F90. It contains two modules and one main code. The main code is at the end of the file, and must be there for it to use the two modules. The program has code to create plots using NCAR GKS graphics. The graphics code is currently disabled using conditional compilation with #define, #ifdef, #endif. All sections of graphics code are bracketed in #ifdef NCARGKSOUTPUT, #endif NCARGKSOUTPUT. The first line in the source code has a comment line

```
!#define NCARGKSOUTPUT
```

Uncommenting this line, (removing the "!"), activates the graphics code. The source file is named with .F90 instead of .f90 to activate the pre-processor that processes the NCARGKSOUTPUT lines. To compile xsfint, activate f90 as follows

```
f90 -o xsfint xsfint.F90
```



### **XSFINT Input**

The input file format is as follows

line1 -input cross-section filename

line 2 -output cross-section filename

line 3 -target temperature target pressure interpolate select  
interpolate select

0 = Automatic pick of points to interpolate and interpolate method

1 = Use the temperature, pressure shown on line 4 to select a record from the cross-section file as the new point. (manual pick nearest point)

2 = Use the temperature, pressure shown on line 4 and 5 to select 2 records from the cross-section file to do a two point temperature interpolate on.

3 = Use the temperature, pressure shown on line 4 and 5 to select 2 records from the cross-section file to do a two point pressure interpolate on.

4 = Use the temperature, pressure shown on line 4, 5, 6 and 7 to select 4 records from the cross-section file to do a four point interpolate on.

Lines to specify manual selections contain  
temperature pressure

There can be multiple target points selected in a run, each possibly with different interpolation selectors.

There is an example case on roma in /home/goldman/xsections/interp and is named cfc22.test.input. It contains

```
../cfc22.xsect (cross-section file to read)
cfc22.test.output (cross-section file to create)
220.0 50.0 3 (target 220.0,50.0 manual select points)
216.0 176.8 (point 1 for 2 point pressure interp)
216.0 40.9 (point 2 for 2 point pressure interp)
240.0 300.0 0 (target 240.,300. auto select points & interp)
226.0 223.0 2 (target 226.0, 223.0 manual select points)
237.0 270.4 (point 1 for 2 point temperature interp)
216.0 176.8 (point 2 for 2 point temperature interp)
```

### **Running XSFINT**

To run xsfint on the test case on roma type

```
xsfint <cfc22.test.input >& cfc22.test.output
```

This reads cfc22.test.input and creates cfc22.new.xsect and cfc22.test.output.

### **List of files**

All files are on ms are in /GOLDMAN/VARANAS/XSEC.JUNE.97 except where noted otherwise.

CCL4

Xsection file - ccl4.tar  
Resolution - 0.03 cm<sup>-1</sup>  
Fixed 0.0025 cm<sup>-1</sup> Spc file -ccl4.xsect.25  
Avg Spc file - ccl4.xsect.avgspc  
Table - table.ME0216 in goldman output subdirectory  
Number of Files 32  
Wavenumber range 750.0100-811.9900 cm<sup>-1</sup>

#### CFC11

Xsection file - cfc11.tar  
Resolution - 0.01, 0.03 cm<sup>-1</sup>  
Fixed 0.0025 cm<sup>-1</sup> Spc file -cfc11.xsect.A.25  
cfc11.xsect.B.25  
Avg Spc file - cfc11.xsect.avgspc.A  
cfc11.xsect.avgspc.B  
Table - table.ME0131 (part a) in goldman output subdirectory  
table.ME7904 (part b) in goldman output subdirectory  
Number of Files 55  
Wavenumber range 810.0060-879.9930 cm<sup>-1</sup>  
1050.0000-1119.9930 cm<sup>-1</sup>

#### CFC12

Xsection file - cfc12.tar  
Resolution - 0.01, 0.02, 0.03 cm<sup>-1</sup>  
Fixed 0.0025 cm<sup>-1</sup> Spc file -cfc12.xsect.A.25  
cfc12.xsect.B.25  
Avg Spc file - cfc12.xsect.avgspc.A  
cfc12.xsect.avgspc.B  
Table - table.ME8745 (part a) in goldman output subdirectory  
table.ME6165 (part b) in goldman output subdirectory  
Number of Files 51  
Wavenumber range 850.0050-949.9950 cm<sup>-1</sup>  
1050.0060-1199.9850 cm<sup>-1</sup>

#### CFC22

Xsection file - cfc22.tar  
Resolution - 0.03 cm<sup>-1</sup>  
Fixed 0.0025 cm<sup>-1</sup> Spc file -cfc22.xsect.25  
Avg Spc file - cfc22.xsect.avgspc  
Table - table.ME0088 in goldman output subdirectory  
Number of Files 7  
Wavenumber range 760.0300-860.000 cm<sup>-1</sup>

### SF6

Xsection file - sf6.tar

Resolution -  $0.03 \text{ cm}^{-1}$

Fixed  $0.0025 \text{ cm}^{-1}$  Spc file -sf6.xsect.25

Avg Spc file - sf6.xsect.avgspc

Table - table.ME0112 in goldman output subdirectory

Number of Files 7

Wavenumber range  $925.0100\text{-}955.000 \text{ cm}^{-1}$

### CF4

Xsection file - cfc14.tar

Resolution -  $0.01, 0.03 \text{ cm}^{-1}$

Fixed  $0.0025 \text{ cm}^{-1}$  Spc file -cfc14.xsect

Avg Spc file - cfc14.xsect.avgspc

Table - table.ME0132 in goldman output subdirectory

Number of Files 54

Wavenumber range  $1250.0050\text{-}1289.9975 \text{ cm}^{-1}$

## REFERENCES

### A3.3.1.1: Ray Tracing

Allen, C.W., *Astrophysical Quantities*. Athlone Press, 1976.

Ciddor, P.E. Refractive index of air: new equations for the visible and near infrared. *Applied Optics*, 35, 1566-1573, 1996.

Edlén, B., The Refractive Index of Air, *Metrologia*, 2, 71-80, 1966.

Birch, K. P., and M. J. Downs, An Updated Edlén Equation for the Refractive Index of Air, *Metrologia*, 30, 155-162, 1993.

Birch, K. P., and M. J. Downs, Correction to the Updated Edlén Equation for the Refractive Index of Air, *Metrologia*, 31, 315-316, 1994.

Coleman, C. D., W. R. Bozman, and W. F. Meggers, *Table of Wavenumbers*, US Department of Commerce, NBS Monograph 3, May, 1960.

### A3.3.2.3: Global Land Cover Characteristics Data Base

Anderson, J.R., E.E. Hardy, J.T. Roach and R.E. Witmer, A land use and land cover classification system for use with remote sensor data, *U.S. Geological Survey Professional Paper* 964, 28, 1976.

Belward, A.S., ed., The IGBP-DIS global 1 km land cover data set (DISCover)-proposal and implementation plans, *IGBP-DIS Working Paper No. 13*, Toulouse, France, 1996.

Brown, J.F., T.R. Loveland, J.W. Merchant, B.C. Reed, and D.O. Ohlen, Using multisource data in global land cover characterization: concepts, requirements and methods, *Photogrammetric Engineering and Remote Sensing*, 59, 977-987, 1993.

Brown, J.F., B.C Reed, and L. Huewe, Advanced strategy for multi-source analysis and visualization in land cover characterization, *Proceedings, Pecora 13, Human Interactions with the Environment: Perspectives From Space*, in press.

Loveland, T.R., J.W. Merchant, J.F. Brown, D.O., Ohlen, B.C. Reed, P. Olson, and J., Hutchinson, Seasonal land-cover regions of the United States, *Annals of the Association of American Geographers*, 85, 2, 339-355, 1995.

Loveland, T.R., J.W. Merchant, D.O. Ohlen, and J.F. Brown, Development of a land-cover characteristics database for the conterminous U.S., *Photogrammetric Engineering and Remote Sensing*, 57, 11, 1453-1463, 1991.

Loveland, T.R., D.O. Ohlen, J.F. Brown, B.C. Reed, Z. Zhu, J.W. Merchant, and L. Yang, Western hemisphere land cover-progress toward a global land cover characteristics database, *Proceedings, Pecora 13, Human Interventions with the Environment: Perspectives From Space*, in press.

Olson, J.S., 1994a, *Global ecosystem framework-definitions*, USGS EROS Data Center Internal Report, Sioux Falls, SD, 1994.

Olson, J.S., 1994b, *Global ecosystem framework-translation strategy*, USGS EROS Data Center Internal Report, Sioux Falls, SD, 1994.

Zhu, Z., and L. Yang, Characteristics of the 1-km AVHRR data set for North America, *International Journal of Remote Sensing*, 17, 1915-1924, 1996.

#### A3.3.8.1: ABSCO DATABASES: Line Parameters

Arlander, D. W., A. Barbe, M.T. Bourgeois, A. Hamdouni, J.-M. Flaud, C. Camy-Peyret, and Ph. Demoulin, The identification of  $^{16}\text{O}^{18}\text{O}^{16}\text{O}$  and  $^{16}\text{O}^{16}\text{O}^{18}\text{O}$  ozone isotopes in high resolution ground-based FTIR spectra, *J. Quant. Spectrosc. & Radiat. Transfer*, 52, 267-271, 1994.

Brown, L. R., M.R. Gunson, R.A. Toth, F.W. Irion, C.P. Rinsland and A. Goldman, The 1995 Atmospheric Trace Molecule Spectroscopy (ATMOS) Linelist. *Appl. Opt.*, 35, 2828-2848, 1996.

Dana, V., J.-Y. Mandin, M.Y. Allout, A. Perrin, L. Régalia, A. Barbe, J.-J. Plateaux and X. Thomas, Broadening parameters of  $\text{NO}_2$  Lines in the 3.4  $\mu\text{m}$  Spectral Region, *J. Quant. Spectrosc. Radiat. Transfer*, 57, 445-457, 1997.

D'Cunha, R., V.A. Job, G. Rahappan, V. Malathy Devi, W.J. Lafferty, and A. Weber, The High-Resolution Infrared Spectrum of the  $\nu_1/2\nu_2$  Fermi Dyad Bands of  $\text{COF}_2$ , *J. Molec. Spectrosc.*, 186, 363-373, 1997.

Flaud, J.-M., C. Camy-Peyret, A. Mahmoudi, and G. Guelachvili, The  $\nu_2$  band of  $\text{HD}^{16}\text{O}$ , *Internat. J. Infrared and Millimeter Waves*, 7, 1063-1090, 1986.

Flaud, J.-M., M.T. Bougeois, A. Barbe, J.J. Plateaux, and C. Camy-Peyret, The  $\nu_1 + \nu_3$  bands of  $^{16}\text{O}^{18}\text{O}^{16}\text{O}$  and  $^{16}\text{O}^{16}\text{O}^{18}\text{O}$ , *J. Molec. Spectrosc.*, 165, 464-469, 1994.

Goldman, A., W.G.Schoenfeld, T.M. Stephen, F.J. Murcray, C.P. Rinsland, A. Barbe, A. Hamdouni, J.-M. Flaud, and C. Camy-Peyret, Isotopic ozone in the 5 $\mu$  region from high resolution balloon-borne and ground-based FTIR solar spectra, *J. Quant. Spectrosc. & Radiat. Transfer*, 59, 231-244, 1998.

Goldman, A., R.R. Gamache, A. Perrin, J.-M. Flaud, C.P. Rinsland, and L.S. Rothman, HITRAN Partition Functions and Weighted Transition Probabilities, *J. Quant. Spectrosc. & Radiat. Transfer*, to be submitted.

- Heyart, M. A. Perrin, J.-M. Flaud, C. Camy-Peyret, C. P. Rinsland, M. A. H. Smith, and V., Malathy Devi, The  $\nu_1$  and  $\nu_3$  bands of  $^{16}\text{O}^{17}\text{O}^{16}\text{O}$  line positions and intensities, *J. Molec. Spectrosc.*, **156**, 210-216, 1992.
- Heyart, M., A. Perrin, J.-M. Flaud, C. Camy-Peyret, C.P. Rinsland, M.A.H. Smith, and V. Malathy Devi, The hybrid-type bands  $\nu_1$  and  $\nu_3$  of  $^{16}\text{O}^{16}\text{O}^{17}\text{O}$  line positions and intensities, *J. Molec. Spectrosc.*, **157**, 524-531, 1993.
- Malathy Devi, V. D. C. Benner, C.P. Rinsland, M.A.H. Smith, and D.S.Parmar, Infrared Spectroscopy of the  $\text{CO}_2$  Molecule, Recent Res. Devel. in *Geophys Res.*, **1**, 119-148, 1996.
- Malathy Devi, V., D. C. Benner, C.P. Rinsland, and M.A.H. Smith, Absolute Rovibrational Intensities of  $^{12}\text{C}^{16}\text{O}_2$  Absorption Bands in the 3090 to 3800- $\text{cm}^{-1}$  Spectral Region. *J. Quant. Spectrosc. Radiat. Transfer*, **60**, 741-770 1998a.
- Malathy Devi, V., D. C. Benner, C.P. Rinsland, M.A.H. Smith, and D.S.Parmar, Infrared Spectroscopy of the  $\text{CO}_2$  Molecule: *Research Signpost: Recent Research Developments in Geophysical Research*, Vol. 1, pp. 119-148, S. G. Pandalai, editor, 1997.
- Malathy Devi, V., D. C. Benner, M.A.H. Smith, and C.P. Rinsland, Air and  $\text{N}_2$  Broadening Coefficients and Pressure Shift Coefficients in the  $^{12}\text{C}^{16}\text{O}_2$  Laser Bands, 52nd Ohio State University International Symposium on Molecular Spectroscopy, paper RF14, June 16-20, 1997.
- Malathy Devi, V., D. C. Benner, M.A.H. Smith, and C.P. Rinsland, Self-Broadening and Self-Shift Coefficients in the Fundamental Band of CO. *J. Quant. Spectrosc. Radiat. Transfer*, **60**, 815-824, 1998b.
- Malathy Devi, V., D. C. Benner, M.A.H. Smith, and C.P. Rinsland, Pressure-Broadening and Shift Coefficients in the  $2\nu_2^0$  and  $\nu_1$  Bands of  $^{16}\text{O}^{13}\text{C}^{18}\text{O}$ . 52nd Ohio State University International Symposium on Molecular Spectroscopy, paper RF13, June 16-20, 1997.
- Malathy Devi, V., D. C. Benner, M.A.H. Smith, and C.P. Rinsland, Pressure-Broadening and Pressure Shift Coefficients in the  $2\nu_2^0$  and  $\nu_1$  Bands of  $^{16}\text{O}^{13}\text{C}^{18}\text{O}$ . *J. Quant. Spectrosc. Radiat. Transfer*, **60**, 771-783, 1998.
- Malathy Devi, V., D. C. Benner, M.A.H. Smith, and C.P. Rinsland, Air- and  $\text{N}_2$  Broadening Coefficients and Pressure-shift Coefficients in the  $^{12}\text{C}^{16}\text{O}_2$  Laser Bands. *J. Quant. Spectrosc. Radiat. Transfer*, **59**, 137-150, 1998.
- Mandin, J.-Y., V. Dana, A. Perrin, J.-M. Flaud, C. Camy-Peyret, L. Régalia, and A. Barbe, The  $\{\nu_1 + 2\nu_2, \nu_1 + \nu_3\}$  bands of  $\text{NO}_2$ : Line positions and intensities; Line intensities in the  $\nu_1 + \nu_2 + \nu_3 - \nu_2$  hot band, *J. Mol. Spectrosc.*, **181**, 379-388, 1997.
- Perrin, A., J.-M. Flaud, and C. Camy-Peyret, Calculated line positions and intensities for the  $\nu_1 + \nu_3$  and  $\nu_1 + \nu_2 + \nu_3 - \nu_2$  band of  $\text{NO}_2$ , *Infrared Phys.*, **22**, 343-348, 1982.

Perrin, A., J.-M. Flaud, F. Keller, A. Goldman, R.D. Blatherwick, F.J. Murcray, and C.P. Rinsland, New analysis of the  $\nu_8 + \nu_9$  band of  $\text{HNO}_3$ : Line positions and intensities, *J. Molec. Spectrosc.*, submitted, 1998.

Pine, A. S., and C. P. Rinsland, The role of torsional hot bands in modeling atmospheric ethane, *53rd International Molecular Spectroscopy Symposium*, Columbus, OH, paper TF17, 1998.

Rinsland, C. P.; J.-M. Flaud, A. Goldman, A. Perrin, C. Camy-Peyret, M.A.H Smith, V. Malathy Devi, D.C. Benner, A. Barbe, T.M. Stephen, and F.J. Murcray, Spectroscopic Parameters for Ozone and Its Isotopes: Current Status, Prospects for Improvement, and the Identification of  $^{16}\text{O}^{16}\text{O}^{17}\text{O}$  and  $^{16}\text{O}^{17}\text{O}^{16}\text{O}$  Lines in Infrared Ground-Based and Stratospheric Solar Absorption Spectra. *J. Quant. Spectrosc. Radiat. Transfer*, 60, 803-814, 1998.

Rinsland, C. P.; M.R. Gunson, P. Wang, R.F. Arduini, B.A. Baum, P. Minnis, A. Goldman, M.C. Abrams, R. Zander, E. Mahieu, R.J. Salawitch, H.A. Michelsen, F.W. Irion, and M.J. Newchurch, ATMOS/ATLAS 3 Infrared Profile Measurements of Clouds in the Tropical and Subtropical Upper Troposphere. *J. Quant. Spectrosc. Radiat. Transfer*, 60, 903-919, 1998.

Rinsland, C. P., N.B. Jones, B. Connor, J.A. Logan, N.S. Pougatchev, A. Goldman, F.J. Murcray, T.M. Stephen, A.S. Pine, R. Zander, E. Mahieu, and E. Demoulin, Northern and Southern Hemisphere Ground-Based Infrared Spectroscopic Measurements of Tropospheric Carbon Monoxide and Ethane, *J. Geophys. Res.*, 60, 665-710, 1998.

Rinsland, C. P.; A. Goldman, and J.-M. Flaud, Infrared Spectroscopic Parameters of  $\text{COF}_2$ ,  $\text{SF}_6$ ,  $\text{ClO}$ ,  $\text{N}_2$ , and  $\text{O}_2$ , *J. Quant. Spectrosc. Radiat. Transfer*, 48, 693-699, 1992.

Rothman, L.S., C.P. Rinsland, A. Goldman, S.T. Massie, D.P. Edwards, J.-M. Flaud, A. Perrin, C. Camy-Peyret, V. Dana, J.-Y. Mandin, J. Schroeder, A. McCann, R.R. Gamache, R.B. Wattson, K. Yoshino, K.V. Chance, K.W. Jucks, L.R. Brown, V. Nemtchinov, and P. Varanasi, The HITRAN Molecular Spectroscopic Database and HAWKS (HITRAN Atmospheric Workstation): 1996 Edition, *J. Quant. Spectrosc. Radiat. Transfer*, 60, 665-710, 1998.

Sen, B.; G.C. Toon, G.B. Osterman, J.-F. Blavier, J.J. Margitan, R.J. Salawitch, and G.K. Yue, Measurements of reactive nitrogen in the stratosphere, *J. Geophys. Res.*, 103, 3571-3585, 1998.

Smith, M. A. H., C. P. Rinsland, V. Malathy Devi, and D. C. Benner, Absolute intensities of  $\text{O}_3$  lines in the 9-11  $\mu\text{m}$  region, *53rd Ohio State University International Symposium on Molecular Spectroscopy*, paper WF04, Columbus, OH, 1998.

Toth, R. A.,  $\text{HD}^{16}\text{O}$ ,  $\text{HD}^{18}\text{O}$ , and  $\text{HD}^{17}\text{O}$  Transition Frequency and Strengths in the  $\nu_2$  Bands, *J. Mol. Spectrosc.*, 162, 20-40, 1993.

Wang, W. F., P.P. Ong, T.L. Tan, E.C. Looi, and H.H. Teo, Infrared analysis of the anharmonic resonance between  $\nu_8 + \nu_9$  and the dark state  $\nu_6 + \nu_7$ , *J. Mol. Spectrosc.*, 183, 407-412, 1997.

LAST PAGE